ABSTRACT

Aerodynamic and Aeroacoustic Design of Small Unmanned Aircraft System Propellers at Low Reynolds Numbers

Ricardo D. Sanchez, M.S.M.E.

Mentor: Kenneth W. Van Treuren, D.Phil.

The Small Unmanned Aircraft System (sUAS) has become an overwhelmingly important asset for military intelligence, surveillance, and reconnaissance in addition to a multitude of needs in the commercial industry. More research should investigate sUAS propulsion systems and specifically the propellers, largely responsible for noise generation and inefficiencies in power consumption at low Reynolds numbers. Experimental noise data compared stock, modified, and five bladed propellers reducing tip vortex strength and noise generation. Results showed measurable far field sound decay and five bladed noise reductions of 5 dBA. Three motors compared propeller power consumption and resulted in increased electrical efficiencies of 14.5% and 31.3%. An airfoil study showed the GOE358 as the most aerodynamically efficient airfoil tested. A Prandtl bell-shaped lift distribution, minimum induced loss design, was applied to a propeller resulting in decreased power consumption and improved electrical efficiency by 18.51% with a SPL reduction of 11.15 dBA compared against the Baseline propeller. The Baseline propeller used an industry standard minimum loss propeller design.

Aerodynamic and Aeroacoustic Design of Small Unmanned Aircraft System Propellers at Low Reynolds Numbers

by

Ricardo D. Sanchez, B.S.M.E.

A Thesis

Approved by the Department of Mechanical Engineering

_____

Paul Ro, Ph.D., Chairperson

Submitted to the Graduate Faculty of
Baylor University in Partial Fulfillment of the
Requirements for the Degree
of

Master of Science in Mechanical Engineering

Approved by the Thesis Committee

_____

Kenneth W. Van Treuren, D.Phil., Chairperson

_____

Anne M. Spence, Ph.D.

_____

Scott Koziol, Ph.D.

Accepted by the Graduate School

December 2020

_____

J. Larry Lyon, Ph.D., Dean

Page bearing signatures is kept on file in the Graduate School.

TABLE OF CONTENTS

LIST OF FIGURES

LIST OF TABLES

NOMENCLATURE

A	=	Total Lift parallel force
a	=	Axial Induction Factor
a_0	=	Lift Curve Slope
a’	=	Tangential Induction Factor
AOA	=	Angle of Attack
B	=	Number of Blades
b	=	Airfoil Width/Span
B&K	=	Brüel & Kjaer
BET	=	Blade Element Theory
BEMT	=	Blade Element Momentum Theory
c	=	Chord Length
C_d	=	Coefficient of Drag
C_l	=	Coefficient of Lift
C_M	=	Coefficient of Moment
C_P	=	Coefficient of Power
C_T	=	Coefficient of Thrust
CFD	=	Computational Fluid Dynamics
D	=	Drag Force
DAQ	=	Data Acquisition
dB	=	Decibel

dBA	=	A-Weighted Decibel
dD	=	Element Drag Force
dL	=	Element Lift Force
dQ	=	Element Torque Force
dT	=	Element Torque Force
DW	=	Dimensional Downwash
ELD	=	Engineering Design Laboratory Inc.
eVTOL	=	Electric Vertical Takeoff and Landing
F	=	Force
FFT	=	Fast Fourier Transform
GUI	=	Guided User Interface
I	=	Current
L	=	Lift Force
L/D	=	Lift to Drag Ratio
L/D_{Max}	=	Maximum Lift to Drag Ratio
M	=	Bending Moment
N	=	Normal Force
NACA	=	National Advisory Committee for Aeronautics
NAFNoise	=	NREL AirFoil Noise
NI	=	National Instruments
NREL	=	National Renewable Energy Laboratory
Δp	=	Pressure Increase Due to Energy
p’	=	Pressure In Front of Disk (Momentum)

p	=	Pressure
P	=	Power
QMIL	=	Propeller Design Code
QPROP	=	Propeller Analysis Code
R	=	Total Radius of Blade Element
r	=	Local Radius at Blade Element
Re	=	Reynolds Number
RPM	=	Rotations per Minute
sUAS	=	Small Unmanned Aircraft System
S	=	Airfoil Planform Area
SPL	=	Sound Pressure Level
T	=	Thrust Force
TBL	=	Turbulent Boundary Layer
TSR	=	Tip Speed Ratio
UAM	=	Urban Air Mobility
UAS	=	Unmanned Aircraft System
UASs	=	Unmanned Aircraft Systems
U_∞	=	Freestream Wind Speed
UIUC	=	University of Illinois Urbana-Champaign
USAFA	=	United States Air Force Academy
V	=	Velocity
V_i	=	Induced Velocity in Thrust Direction
V_{R0}	=	Resultant Velocity

V_t	=	Propeller Tip speed
V_∞	=	Freestream Velocity
v	=	Induced Velocity
VI	=	Virtual Instrument
W_i	=	Downward Speed at the Wing given Circulation
w	=	Downwash

GREEK NOMENCLATURE

α	=	Angle of Attack
α_0	=	Lift Curve Slope of Airfoil
β	=	Pitch Angle of the Blade
θ	=	Induced Flow Angle
μ	=	Viscosity
ρ	=	Air Density
η	=	Propeller Efficiency
σ	=	Solidity Ratio
ϕ	=	Helix Angle
ϕ_0	=	Resultant Flow Angle
ω	=	Angular Wake Velocity
ξ	=	Elliptic Distribution
Ω	=	Rotational Velocity
Ωr	=	Speed from Rotation

ACKNOWLEDGMENTS

First and foremost, I must always thank God for all that I have been blessed with and for the opportunity to attend Baylor University for the past six years.

Dr. Kenneth Van Treuren has had a major impact on my academic career as well in being a professional mentor. His support and guidance throughout the past years has been important for my success and it's something that I will always be grateful for.

I'd like to also highlight other faculty members that have been key to my success are Dr. Anne Spence who has been a great influence in the classroom and within the Baylor Community, thank you for serving on my thesis committee. Dr. Lesley Wright for her mentorship in my undergraduate career, introducing me to research, and for inspiring me to pursue a graduate degree. Mr. Ashley Orr for his machine assistance in propeller design and fabrication help for these past couple of years. Mrs. Jodi Branch who has assisted with the streamlining the administration work necessary to see this thesis through completion.

The previous work done by Trae Liller and Andrew Hays has had large influences on the direction of this work. They set the stage to get this study off the ground and this work would not be possible without their dedication and hard work.

Most of all, I'd also like to thank my family and friends supporting me throughout my Baylor academic career. Were it not for the support and sacrifice of my parents, I would not be in the position that I am today.

To my family Marcia, Pete, Jordin, and Maya Sanchez thank you for the never-ending love and support.

CHAPTER ONE

Introduction

The increased interest in Unmanned Aircraft Systems (UASs) is the result of a wide variety of needs in both military and commercial applications. Today there are numerous innovative UAS designs geared toward the operating environment and mission. Most of the newer designs feature improved range, endurance, and payload capacity. Improving the UAS propulsion system is a key technology to enhanced performance. This chapter will introduce the UAS, its applications, and detail the objectives of this study. Figure 1.1 illustrates the futuristic UAS concept and a current commercial UAS.

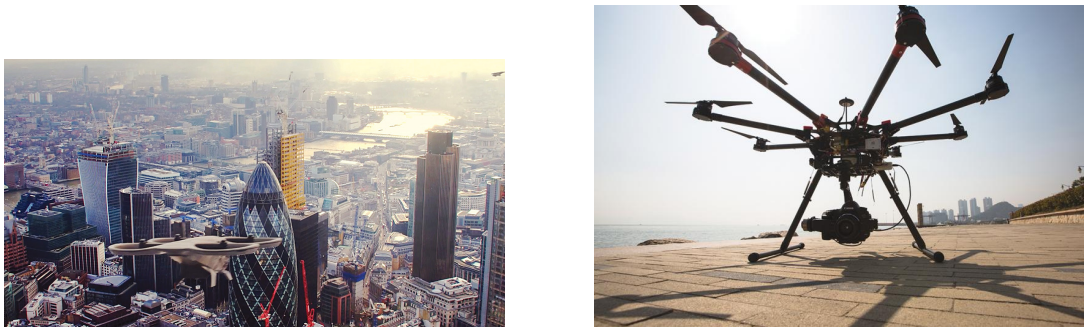

Figure 1.1 Future and Current UAS [1,2]

Future of eVTOL Demands

There has been a substantial increase in electric vertical takeoff and landing (eVTOL) aviation systems as solutions to a multitude of consumer applications. Commercially, some of these uses are logistic package deliveries, recreational photography, agricultural monitoring, and ultimately urban air mobility systems [1]. Technology conglomerate Uber

made a substantial investment expanding their company to meet the demand of urban aviation transportation [3]. Uber desires urban air ridesharing transportation systems that are entirely electric to reduce potential fueling logistics issues and provide more infrastructure consideration as parking depots are needed for the aircraft [3]. Uber's vision is to be known for mass transportation available to a vast number of consumers. This demand will drive the eVTOL market in the future. Figure 1.2 shows a futuristic eVTOL Volocopter aircraft.

Figure 1.2 Futuristic Volocopter Urban Air Mobility [2]

Among the urban air mobility (UAM) industry, eVTOL aircraft is considered as one of the best technologies for the future of urban transportation because they can takeoff vertically, consume less air space, and move people effectively [1-3]. For eVTOL aircraft to operate in urban environments, these vehicles must reduce their noise footprint in the local community. They must use efficient and quiet propellers. The concepts of efficient lift production as well as reduced noise are important when optimizing eVTOL aircraft. In the case of small Unmanned Aircraft Systems (sUASs) in the urban environment, such as quadcopters, these features will be paramount for future use and interaction with the public. Additionally, quadcopters will be increasingly used for more tasks that interact closely with

people [1,2]; therefore, noise reduction and operating lift efficiency must be a significant priority to produce the best vehicle for to co-exist with the public while optimizing its performance.

The United States Air Force (USAF) has also added itself in the eVTOL competition with its support of Agility Prime, a program dedicated to partnering with aerospace stakeholders to advance eVTOL technology [4-5]. The Agility Prime program has become a tool to rapidly develop vehicles for the emerging commercial air mobility market [4-5]. Of these companies, LIFT demonstrated its flight abilities with their proposed Hexa eVTOL vehicle, shown in Fig. 1.3.

Figure 1.4 illustrates the Joby Aviation eVTOL aircraft [5]. The prototypes involved in Agility Prime will be evaluated for airworthiness certifications instead of research and development funding as most of the companies are already privately funded [4-5]. The USAF has also stated their interest in eVTOL as they see its value in quick mobility for security forces on bases, logistics, and involvement to help search-and-rescue missions [5].

Figure 1.3 LIFT Hexa eVTOL Aircraft in Flight [4]

Figure 1.4 Joby Aviation eVTOL Aircraft [5]

UAS Classification

The UAS definition can be very broad as technology emerges across many industries with a wide range of applications. There are multiple categories that classify and separate UAS vehicles [6]. In their simplest form, UASs are robots capable of flight. Under the broad term of drone, there are UASs capable of extremely high-altitude flight and operation in small confined spaces such as buildings. Table 1.1 displays a proposed drone classification based on the weight of the vehicle [7].

Table 1.1 UAS classification based on weight [7]

Classification Category	Weight (lbs)
Micro	W <2
Mini	2 < W < 30
Tactical	30 < W < 1000
Medium and High Altitude	1000 < W < 30,000
Heavy	W > 30,000

The DARPA Black Widow is a micro UAS, Fig 1.5, that only weighs 50 grams [8]. This vehicle was designed to have a micro camera and electric propulsion system. This

UAS was also designed to operate in urban and mountainous terrain with a range of approximately 20km.

Figure 1.5 Micro UAS: DARPA Black Widow [8]

The mini UAS is pictured in Figs. 1.6 and 1.7. Figure 1.6 shows the DJI Phantom 2 Quadcopter. The Quadcopter mini UAS is perhaps the most common among sUAS applications. It is widely used in the commercial market in digital media and recreation. The DJI Phantom 2 Quadcopter has a maximum takeoff weight of 2.8 lbs [9]. This aircraft would be an example of an urban UAS as it was designed and built to support a Gimbal mounted imaging system. Fig. 1.7 shows the U.S. Army RQ-11B Raven Small Unmanned Aircraft System (sUAS).

Figure 1.6 Mini UAS: DJI Phantom 2 Quadcopter [9]

Figure 1.7 Mini UAS: U.S. Army RQ-11B Raven (sUAS) [10]

The RQ-11B Raven sUAS was a low altitude intelligence, surveillance, and reconnaissance (ISR) vehicle [10]. This vehicle weighs 4.2 lbs and could operate for 90 minutes of flight at 300 feet or higher above ground level (AGL). Figure 1.8 illustrates the tactical UAS classification with the Textron Shadow V2 Block III TUAS. This aircraft has a max weight of 467 lbs and was designed to operate in tactical environments [11]. Moreover, the Shadow V2 was designed for payloads up to 95 lbs.

Figure 1.8 Tactical UAS: Textron Shadow V2 Block III TUAS [11]

Figure 1.9 displays an example of a medium and high altitude UAS with the Northrup Grumman RQ-4 Global Hawk. The Global Hawk was designed to be a long endurance ISR aircraft [12]. Figure 1.10 shows another example of a medium and high altitude UAS

Classification with the General Atomics Predator C Avenger. The Predator C Avenger is capable of a maximum gross takeoff weight of approximately 18,000 lbs with missile payloads [13]. This UAS was designed to be a capable of delivering heavily armed payloads as air support in military combat environments.

Figure 1.9 Medium and High Altitude UAS Northrup Grumman RQ-4 Global Hawk [12]

Figure 1.10 Medium and High Altitude UAS General Atomics Predator C Avenger [13]

One of the few examples of a heavy UAS would be the optionally manned version of the F-4 Phantom, the QF-4 [14]. Figure 1.11 shows the heavy UAS that served as a target in simulation air-to-air combat. This aircraft could be shot down as it was unmanned.

Figure 1.11 QF-4 Heavy UAS [14]

Objectives and Scope of Current Study

The scope of the current study was limited to the micro UAS classification. This study was further limited to only analyzing the propulsion system of the UAS with the main emphasis being propeller aerodynamic and aeroacoustic performance. As such, the micro UAS chosen for comparison were the DJI Phantom 2 Quadcopter propeller(s) and motor(s) as well as the U.S. Army RQ-11 Raven propeller. In their respective experiments, the propeller size was limited to a diameter of 9.4 inches for the DJI Phantom 2 comparisons while 8-inch propellers were compared for the RQ-11 Raven. These propellers were designed with the overall objective to reduce the acoustic signature and power consumption. Lastly, the most significant objective was to test the effects of implementing a bell-shaped lift distribution on the propeller instead of the traditional elliptical lift distribution. This means designing propellers for minimum induced drag rather than the

traditional minimum induced loss design. This design also reduced the induced drag by unloading the tip of the propeller which was expected to reduce sound pressure level (SPL) and power consumption.

Presentation Outline

This thesis will be organized into six chapters. Chapter Two will be a literature survey of aeroacoustics, propeller testing, and the Prandtl bell shaped distribution. Chapter Three will provide the propeller theoretical background as it relates to Blade Element Momentum Theory (BEMT), propeller aerodynamics, the Prandtl Bell shaped distribution, and noise. The experimental method and setup of the tests in this study will be presented in Chapter Four. Chapter Five will show the results of the study. The conclusions of this thesis and recommendations for further investigations will be discussed in Chapter Six.

CHAPTER TWO

Literature Survey

Noise from Airfoils

Noise is one of the most obvious concerns that comes as a result of the fluid interaction with airfoils. From Brooks, Pope, and Marcolini it has been determined that airfoil noise can be attributed to a variety of factors that occur as the airfoil interacts with turbulent flow and flow that causes vortex shedding in the wake regions [15]. The sources of noise arise form turbulence at the boundary layer trailing edge, laminar boundary layer vortex shedding, separation stall, trailing edge bluntness vortex shedding, and tip vortex formation occurring at the tip of the object. The National Renewable Energy Laboratory (NREL) has produced their semi-empirical engineering model for aeroacoustic noise (NAFNoise); this model makes predictions for the aeroacoustic noise based on the airfoil [15]. Being able to predict noise based on airfoil selection enhances the decision-making process in propeller design. Additionally, Van Treuren and Hays experienced success utilizing the NAFNoise prediction method for wind turbine airfoils to analyze power production and noise [16].

In the case of sUAS propellers, a large part of the noise contribution comes from the vortex generated at the tip of the propeller which is also directly proportional to the propeller RPM. Fig. 2.1 illustrates the tip vortex formation and how noise propagates to the observer. Studies have shown that modifications to reduce the tip vortex have also reduced the motor RPM and near field noise [15].

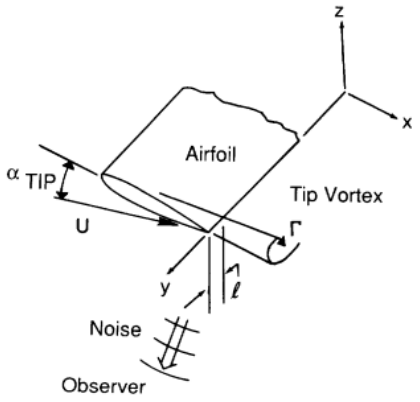

Figure 2.1: Tip Vortex Noise Formation [15]

To achieve steady flight conditions, the aircraft will increase its RPM until it gains the necessary thrust for steady flight. In the case of the quadcopter UAS, this would be the hover condition. For a fixed wing UAS, this would be where steady, level, and unaccelerated flight (SLUF) can be achieved. Inefficient ways of meeting required thrust for the UAS would result in higher operational RPMs which will therefore contribute to increased noise [17]. In the case of a UAS, this is important because of its anticipated community interaction. With the expected increase in UAS applications, the noise emissions must be low enough for the UAS to operate in the urban environment. Empirical tests validated that thrust and power are directly related to the diameter and pitch of a quadcopter propeller [18]. In the case of quadcopter propeller design, a design point of more thrust will be presumed to require more power and, thus, results in increased noise.

Wing and Wing Tip Modifications

A significant amount of costs, upwards of $400 million dollars in some cases, are incurred from the induced drag at the tip of a wing [19]. Several studies have shown that wing tip vortices have led to the implementation of the typical winglets that appear on most

modern commercial and military aircraft [19-21]. This dependent relationship of noise and thrust phenomena occurring at the tip of a wing also carries over to propellers [17]. Propellers can be thought of as rotating wings. Vortices that occur at the edge of a wing cause a rollup-up behavior in a wake formation aft of the propeller or wing. These vortices result in drag due to lift, otherwise known as induced drag [19]. The induced drag, therefore, will effectively continue proportionally to lift; applied to an airplane wing, this helps to explain why wing-tip vortices grow with an increase in lift. Research has shown that there are a series of modifications that wingtips may undergo to decrease induced drag ultimately creating a more efficient lift distribution [19-21].

Winglet modifications have shown a 4-5% fuel reduction for the Boeing 737-NG model shown with Fig. 2.2 [19]. Figure 2.3 illustrates the net-savings estimates for the winglet modification of the KC-10 [19]. Ultimately, these modifications have been successful by reducing induced drag over long duration flights and short takeoff demands as they are seen on nearly every commercial airliner today. As it applies to propellers, reducing the tip vortices would also assist in efficiency for generating lift. This would reduce the overall drag due to lift. A propeller designed to operate with minimum induced drag would become more efficient at generating lift and reducing power consumption.

Figure 2.2 Boeing 7373-NG and Winglet Design [19]

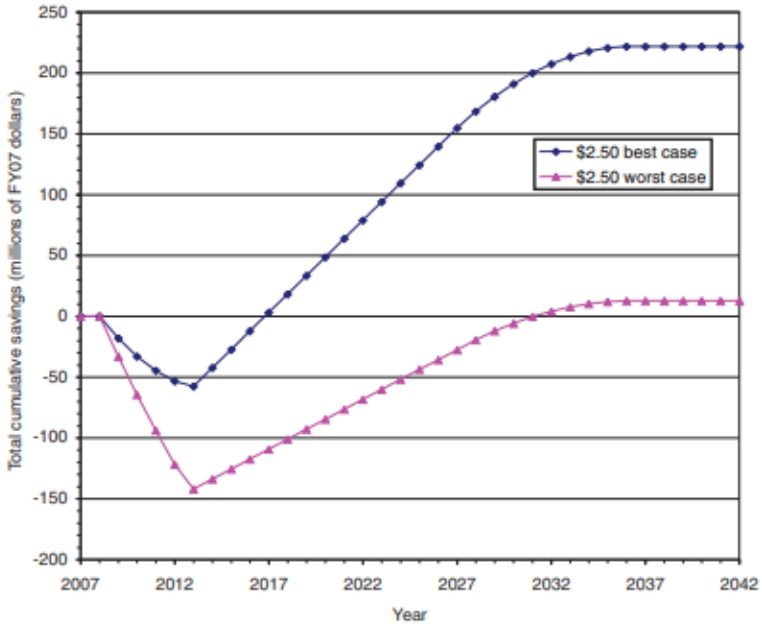

Figure 2.3 KC-10 Estimated Inventory Net-Savings Over Time [19]

Lift Distributions: Prandtl Elliptical Distribution and Lifting-Line Theory

In the realm of aircraft performance, the elliptical lift distribution has been the standard optimum lift distribution for spanwise loading on a wing planform. The elliptical lift distribution has an Oswald Efficiency Factor of 1 which has yielded the best lift distribution over the wingspan, reducing wing tip vortices and lowering induced drag. The Supermarine Spitfire of World War II is a great example of this lift distribution. The lift distribution is highest inboard of the wing and gradually decreases as the wingspan increases. Figure 2.4 illustrates the elliptical lift distribution. Therefore, the best way to optimize this distribution is to make the wingspan as large as possible and decrease the weight of the aircraft; this is not possible without constraints on the wing bending moment [23-25]. Thus, the wingspan must be limited to obtain a feasible wing design. In addition, the elliptical lift distribution will always incur some induced drag at the wing tip as a cost for lift. Therefore, one of the major constraints of the elliptical lift distribution is that there is no feasible design point

that will produce an absolute minimum for induced drag [22]. Ultimately this led Prandtl to produce the Prandtl bell-shaped or 'non-elliptical' lift distribution. In addition, wing-tip modifications have shown that it is possible to address the problem of induced drag and wingspan constraints. The same concept could be applied to propellers, as shown in Fig. 2.5 [17].

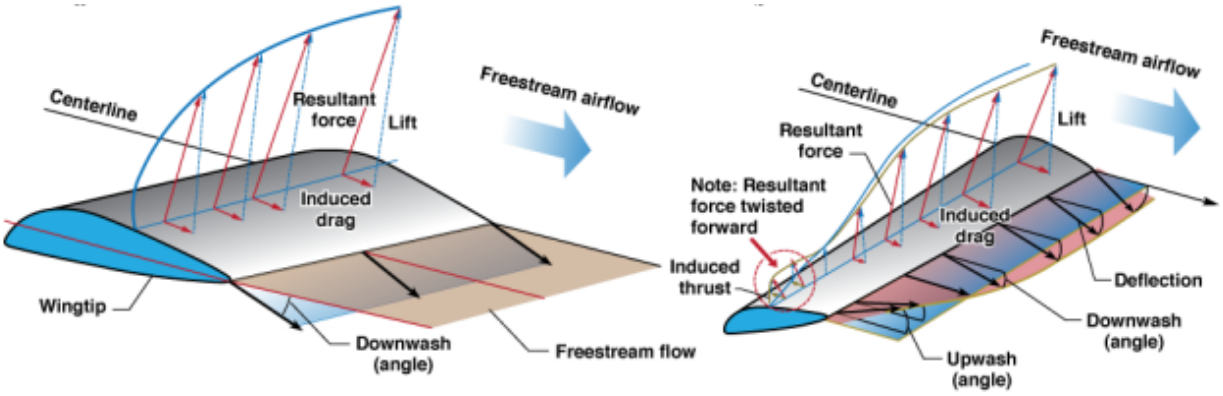

Figure 2.4: Elliptic vs. Prandtl Bell-Shaped Lift Distributions [22]

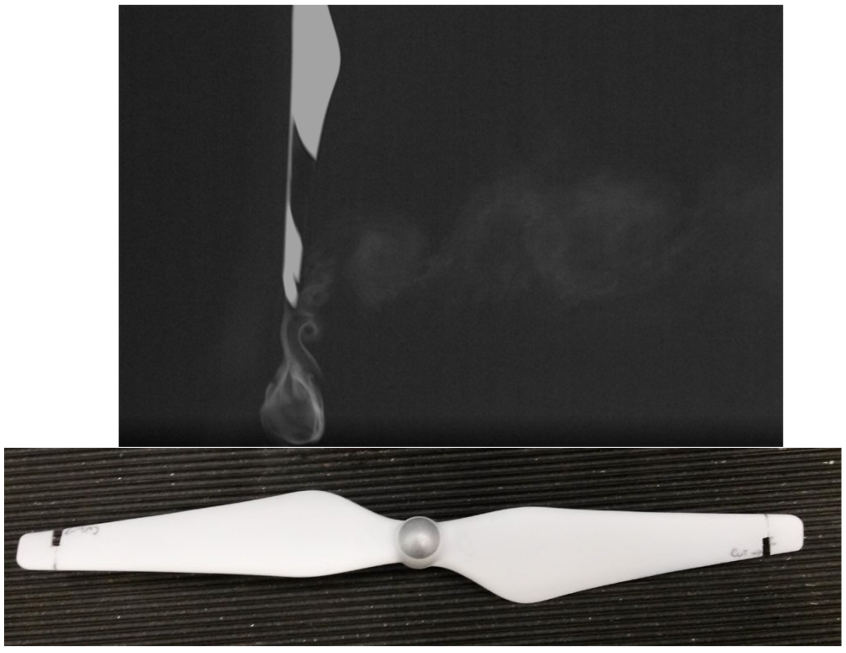

Figure 2.5 Propeller Modification Disrupting the Tip Vortex Strength [17]

In Fig. 2.5 Van Treuren et al. have shown that, like winglets, propeller modifications can also be made to reduce the strength of the tip vortex [17]. Being able to unload the tip of the propeller by its lift distribution could be another way to reduce the tip vortex and induced drag effects for propellers.

Prandtl Bell-Shaped Lift Distribution

The Prandtl bell-shaped or 'non-elliptical' lift distribution was produced by Ludwig Prandtl in 1933 [22-26]. The Prandtl bell-shaped lift distribution was developed in an attempt to improve the standard elliptical lift distribution he developed in 1922 with a minimum induced drag design, similar to birds. Prandtl determined that there must be a constraint on the span of the distribution, and that there was a solution that produced minimum induced drag like the lift distribution on a bird's wing [22]. The bell-shaped distribution has an 11% increase in efficiency, but it requires a 22% increase in its span compared to the elliptical lift distribution [22-26]. Bowers et al. used birds as an example to question the elliptical lift distribution. Birds do not have vertical tails and their wings are often tapered to a sharp point where the outer feathers experience minimal loading - a stark contrast to the elliptical lift distribution. What differentiates the elliptical and bell-shaped lift distributions is the ability for the non-elliptic lift distribution to unload the tip. This results in an absolute minimum induced drag of zero at the wingtip which is illustrated in Fig. 2.3 [22]. Furthermore, the wing vortices of the non-elliptic lift distribution produce vortices more inboard to the wing as opposed to outboard of the wing and at the wing tips [22,26]. Figure 2.6 illustrates the vortex rollup applied to the flying wing model tested by Bowers et al.

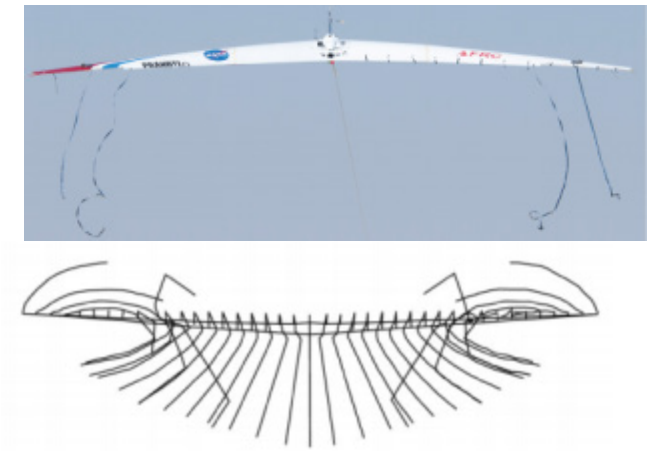

Figure 2.6 Flying Wing Model and Vortex rollup [22]

Current studies have investigated the application of the Prandtl bell-shaped lift distribution for flying wing models that resulted in an explanation for producing proverse yaw without or with a minimized vertical stabilizer [22, 24]. Bowers et al. provided biomimicry analysis of birds as a means to explain how they can maneuver without a vertical construct of some sort to produce proverse yaw. He said that the superior lift distribution answers this phenomenon by using induced thrust to produce yaw with a control surface [22]. Figure 2.6 illustrates the aircraft he used to demonstrate the concept and the vortex rollup of this flying wing design. Another current study by Carrizalez et al. have provided analytical solutions detailing a 14% improvement in the lift to drag ratio with a 44.34% reduction in the vertical tail size which would provide a 17% improvement in aircraft range [26]. This study suggests a decrease in vertical tail plane size is due to the non-elliptic lift distributions' ability to produce proverse yaw while enhancing its ability to create lift [26]. The vertical tail is a control surface on aircraft that stabilize its lateral direction in flight, but it also creates a moment about its axis that helps the vehicle create proverse yaw. If the bell-shaped lift distribution produces proverse yaw, the vertical tail

plane size would be decreased meaning that the aircraft could create the yawing moment with less influence from the vertical tail control surface. Further computational studies conducted at the University of Illinois at Urbana Champaign (UIUC) have shown how the Jones and Prandtl wing designs experience very minimal tip vortices in comparison to the standard elliptic lift distribution [23]. The Jones distribution constrains the lift and root bending moment, and the Prandtl bell-shaped distribution constrains the lift and integrated bending moment [24]. The Jones wing design is also for minimum induced drag where the lift and bending moment about the wing remain fixed while the span varied [27]. The Jones study resulted in a 15% reduction in the induced drag with a 15% increase in the span when compared to the elliptic lift distribution [27]. Another study by researchers at the U.S. Air Force Research Laboratory at Wright-Patterson Air Force Base have shown analytic solutions comparing minimum induced drag reductions using the Prandtl bell-shaped lift distributions to the elliptic lift distributions in three separate cases constraining weight, stress and deflection, chord length, and wing loading [28]. They applied analytic solutions to determine an optimum lift distribution compared to the elliptic lift distribution for the given constraints in the first case constraining 1) weight, maximum stress, and chord length; 2) weight, maximum stress, and fixed wing loading; 3) weight, maximum deflection, and fixed wing loading [28]. In each case of the study the optimized lift distribution results had reductions in induced drag that were better than the elliptic lift distribution, under the same constraints for each case. Ultimately, these studies have all agreed that the non-elliptic or Prandtl bell-shaped lift distribution can provide up to 11% drag reduction for a 22% increase in the span [22-26]. Thus, this lift distribution should

be applied to propellers in order to minimize induced drag and reduce the overall noise production by also eliminating tip vortices.

Despite the fact that the Prandtl bell-shaped theory was developed almost a century ago, limited literature is available on its application. Therefore, it was recommended that experimental studies be completed to compliment the few computational studies that have been done. Experimentally investigating the minimum induced drag distribution applied to a wing body or propeller's lift distribution should verify that unloading the tip is beneficial as previous studies have shown: reducing the loading at the outboard edge of the distribution, unloading the tip, and reducing induced drag would provide greater lift efficiency. There have been no studies in literature indicating that the Prandtl bell-shaped distribution has been applied to propeller design for experimental evaluation. Thus, the Prandtl bell-shaped lift distribution should be investigated for decreasing noise and reducing power required at low Reynolds numbers.

Applying the minimum induced drag lift distribution to sUAS propellers should lower the lift coefficient near the tip. Lowering the lift coefficient would lower the torque which would then also reduce the power consumption. Reducing power consumption would enhance the electrical efficiency of the propeller and thereby conserve power for the sUAS. The noise should also experience reductions due to the vortices occurring more inboard of the blade instead of at the tip. The RPM would also experience changes with a minimum induced drag lift distribution. Zolbayar has conducted a study on low-tip-speed propellers relating noise to large scaled aircraft; showing that noise reduction occurs at lower speeds [29]. His objective was to lower the relative rotational speed of the blade by reducing the RPM to also reduce the noise. This investigation should complement Zolbayar's study as

it relates to the changing the lift distributions to see if the new design method changes RPM and noise generation. Further studies could investigate optimization of propeller RPMs. In conclusion, the Prandtl bell-shaped lift distribution should result in a reduction in power and aeroacoustic noise, key for commercial and military use.

CHAPTER THREE

Theoretical Background

Chapter Three will discuss the airfoil and propeller theory used in this study. The topics discussed will be one-dimensional momentum propeller theory, airfoil theory, blade-element theory (BET), blade element momentum theory (BEMT), and finally noise as it relates to airfoils.

Propeller Theory

One-Dimensional Momentum Propeller Theory

One-dimensional momentum theory is perhaps the simplest theoretical background for propeller analysis [30]. The propeller is described as an actuator disk representing an infinite number of blades. This concept is based on the momentum theory as applied to the actuator. The working fluid, air, is assumed to be incompressible, inviscid, steady, and operating along a streamline. Since the propeller is considered an actuator disk, rotational effects are neglected and not applied to the streamtube. Figure 3.1 depicts one-dimensional momentum theory applied to an actuator disc which is between stations 1 and 2 in the figure. Applying the Bernoulli equation to the first stage of flow (0-1) yields

$$p + \frac{\rho V^2}{2} = p' + \frac{\rho(V+v)^2}{2} \tag{3.1}$$

As air from station 0 moves to station 1, the velocity is equivalent to the freestream velocity V and gradually accelerates with the induced velocity v as it approaches stations 1 and 2. Evaluating the flow aft of the actuator disk (2-3) yields

$$p' + \Delta p + \frac{\rho(V+v)^2}{2} = p + \frac{\rho(V+v_1)^2}{2} \tag{3.2}$$

where Δp is the pressure increase due to added energy in the flow and p' is the pressure right in front of the disk. Solving for the pressure difference Δp reduces the Bernoulli equations to:

$$\Delta p = p + \frac{\rho(V+v_1)^2}{2} - \left(p + \frac{\rho V^2}{2}\right) = \rho\left(V + \frac{v_1}{2}\right)v_1 \tag{3.3}$$

Since thrust is the change in momentum, the thrust produced across the disk area, A, is

$$T = A\Delta p \tag{3.4}$$

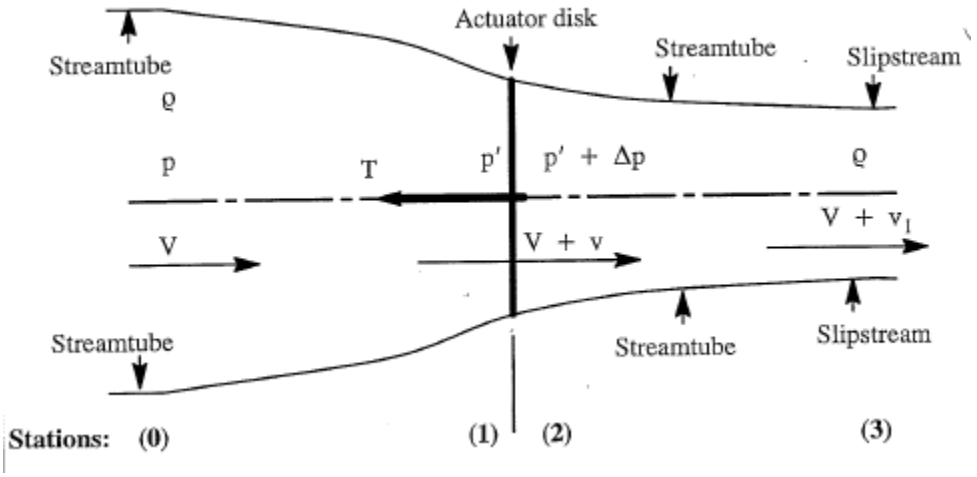

Figure 3.1 One-Dimensional Propeller Theory [30]

With Eq. 3.4 and using Bernoulli's principle, the conservation of linear momentum must be applied to solve for the induced velocity, v_1, that is sufficiently far downstream. The sum of forces acting on the control volume between stations 0 and 3 is represented in Eq. 3.5

$$\sum \vec{F} = \int_S \rho \vec{V}\,(\vec{V} \cdot d\vec{A}) \tag{3.5}$$

Since thrust, T, acts in the opposite direction of the sum of forces on the control volume

$$T = \rho A(V + v)v_1 \tag{3.6}$$

With this knowledge and definitions of thrust from Eq. 3.4 and 3.6, the induced velocity far downstream can be solved resulting in

$$v_1 = 2v \tag{3.7}$$

This shows that the induced velocities that occur far downstream of the disk are twice that of the induced velocities that occur at the disk. Now, the induced velocity at the disk, v, can be solved by rearranging Eq. 3.6 to be

$$T = 2\rho A(V + v)v \tag{3.8}$$

Therefore, the induced velocity becomes

$$v = -\frac{V}{2} + \sqrt{\left(\frac{V}{2}\right)^2 + \frac{T}{2A\rho}} \tag{3.9}$$

Lastly, the ideal propeller efficiency can be solved. This would be an ideal efficiency due to the inability to account for extra losses and drag assumed negligible. The efficiency is a ratio of the power output gained as a result of thrust and velocity, to the power input that is required to overcome momentum. This can now be written as

$$\eta = \frac{TV}{T(V+v)} = \frac{V}{V+v} \tag{3.10}$$

Airfoil Theory

It is important to see the use of the airfoil in propeller design. The airfoil is largely responsible for the aerodynamic performance, and by default, the aeroacoustics of aircraft wings and propellers. This section will be limited to the airfoil aerodynamics only. Figure 3.2 below shows the basic nomenclature associated with airfoils. To begin, this figure illustrates a cambered airfoil. The camber and thickness of the airfoil provide the physical shape, otherwise the airfoil would be symmetrical. The mean camber line can be defined

as a line equal in distance between the top and bottom of the airfoil, depicted by the dotted line in Fig. 3.2. The camber is defined as the distance between the chord line and the mean camber line. The chord line is the straight line from the leading edge to the trailing edge of the airfoil. The magnitude of the chord line would also equal this distance. The maximum thickness would then be the maximum distance between the top and bottom surfaces, typically represented as a percentage in relation to the chord.

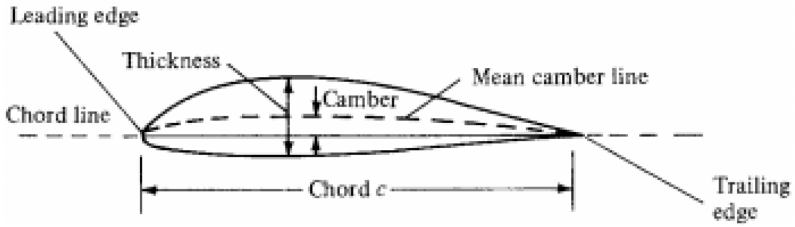

Figure 3.2 Airfoil Nomenclature [31]

Perhaps the most important parameters in airfoil theory would be the concepts of lift, drag, and angle of attack. The lift and drag can be characterized as forces generated by the flow over the airfoil. The lift force acts perpendicular to the freestream velocity, V_∞, while the drag acts parallel to the same vector, illustrated in Fig. 3.3.

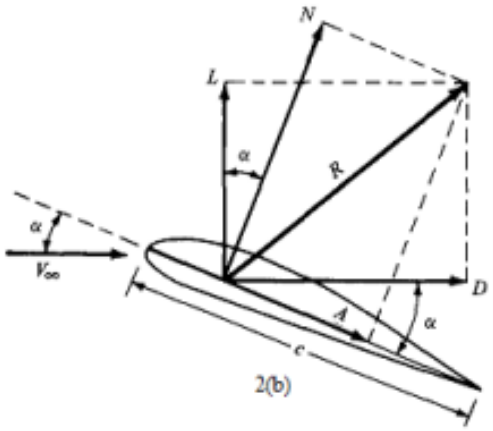

Figure 3.3: Lift and Drag on an Airfoil [32]

For low Reynolds numbers, the lifting force is mainly generated by the net pressure difference between the bottom and top of the airfoil, with low pressure on the upper surface and higher pressure on the lower surface. The non-dimensional force coefficients for a two-dimensional airfoil can be described as

$$C_l = \frac{L}{\frac{1}{2}\rho V^2 S} \tag{3.12}$$

$$C_d = \frac{D}{\frac{1}{2}\rho V^2 S} \tag{3.13}$$

$$S = b \cdot c \tag{3.14}$$

$$\frac{L}{D} = \frac{C_l}{C_d} \tag{3.15}$$

where C_l would be the coefficient of lift, C_d is the coefficient of drag, S is the planform area of the airfoil, b is the span of the airfoil, c is the chord of the airfoil, L is the lifting force, D is the drag force and V is the freestream velocity. Furthermore, it must be noted that for the airfoil applications, it is assumed that the aircraft is operating under steady, level, unaccelerated flight conditions.

Figure 3.4 illustrates the typical behavior of an airfoil's coefficient of lift as a function of the angle of attack. It is observed that for increasing angle of attack α, the coefficient of lift increases until it reaches the $C_{l,max}$ at which the airfoil reaches the stall point. The angle of attack (AOA), α, is the angle between the chord line and the incoming velocity. When stall occurs, it is due to flow separation from the upper surface of the airfoil. Typical airfoil behavior has an approximately linear slope from the point at which the angle of attack produces zero lift, $a_{L=0}$, to just before the maximum coefficient of lift region. This is depicted as the lift curve slope, a_0, of the airfoil. With these known variables, the airfoil coefficient of lift can be calculated as follows

$$c_l = a_0\alpha + c_{l,0} \tag{3.16}$$

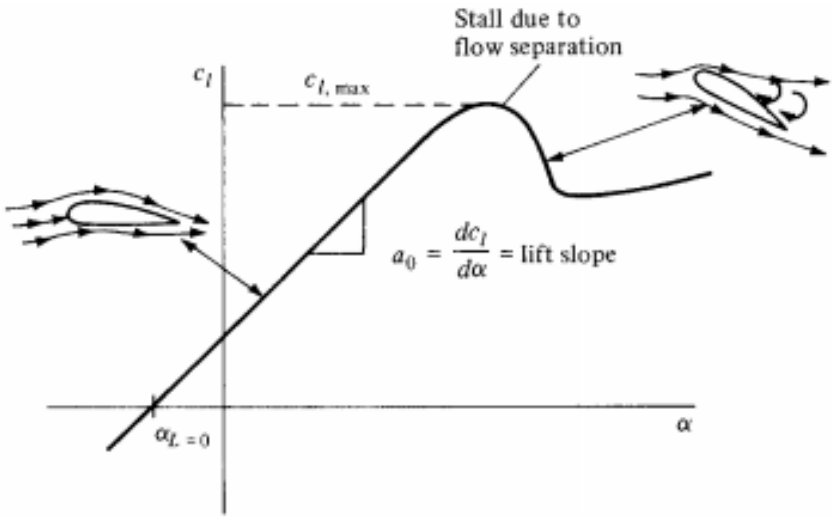

Figure 3.4 Typical Airfoil Plot for Coefficient of Lift vs. Angle of Attack [31]

For propeller design, it is important to know the ratio of the coefficient of lift to the coefficient of drag, the Reynolds number (Re) operating range, and the coefficient of lift as a function of AOA. The Reynolds number is defined as the non-dimensional ratio of inertial forces to viscous forces as shown with Eq. 3.17 where μ is the kinematic viscosity, c is the chord length, V_∞ is the freestream velocity, and ρ is the density of the fluid.

$$Re = \frac{\rho V_\infty c}{\mu} \tag{3.17}$$

As seen in Fig. 3.4, the optimal region for a design (high c_l) would be the AOA at the highest portion of the linear curve just before the max coefficient of lift so that the airfoil does not stall. Figure 3.5 illustrates a typical plot of coefficient of lift to drag ratio vs. AOA as a function of the Reynolds number [34]. A high value for L/D would mean that the airfoil is producing a large amount of lift for a small amount of drag. This is important because an L/D_{Max} occurs at the peak of the L/D curve. A broad top of the L/D curve would

represent a wide range of angles of attack at which the airfoil can maximize its performance for on-design operating conditions. Conversely, a sharp peak in the L/D curve would provide only one optimum angle of attack. Other angles would be off-design which could lead to stall effects and poor performance. These plots show that the L/D curve is directly related to the Reynolds number. The L/D values increase in magnitude with an increase in Reynolds number.

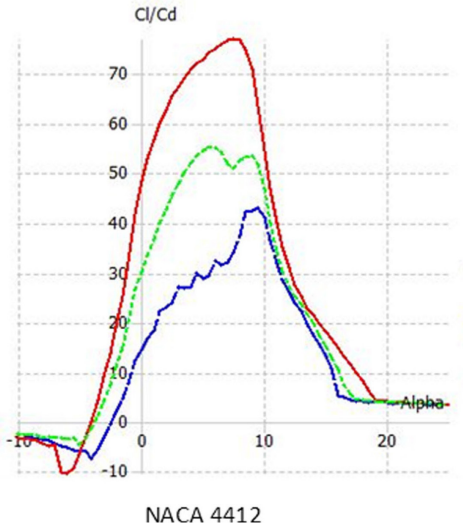

Figure 3.5 Typical Airfoil Characteristics for Coefficient of Lift and Drag Ratios vs. AOA for Reynolds Numbers of 75,000 (blue), 100,000 (green), and 200,000 (red) [33]

Blade Element Theory

Blade Element Theory (BET) is based on dividing the propeller blade into separate airfoil cross-section elements. Unlike the one-dimensional momentum propeller theory which uses an actuator disk, BET uses a finite number of blades for the propeller. Figure 3.6 illustrates the propeller blade BET geometry. Moreover, this theory analyzes local velocity components to determine the lift (dL) and drag (dD) coefficients for each blade section at a distance 'r' from the hub. The other parameters in Figure 3.6 are as follows:

- V is the forward velocity of the system
- β is the geometric pitch angle of the blade
- ρ is the fluid density
- Φ is the helix angle
- Ωr is the speed from rotation
- dT is the thrust of the blade
- dQ is the torque of the blade
- dD is the drag forces of the blade
- dL is the lift force of the blade

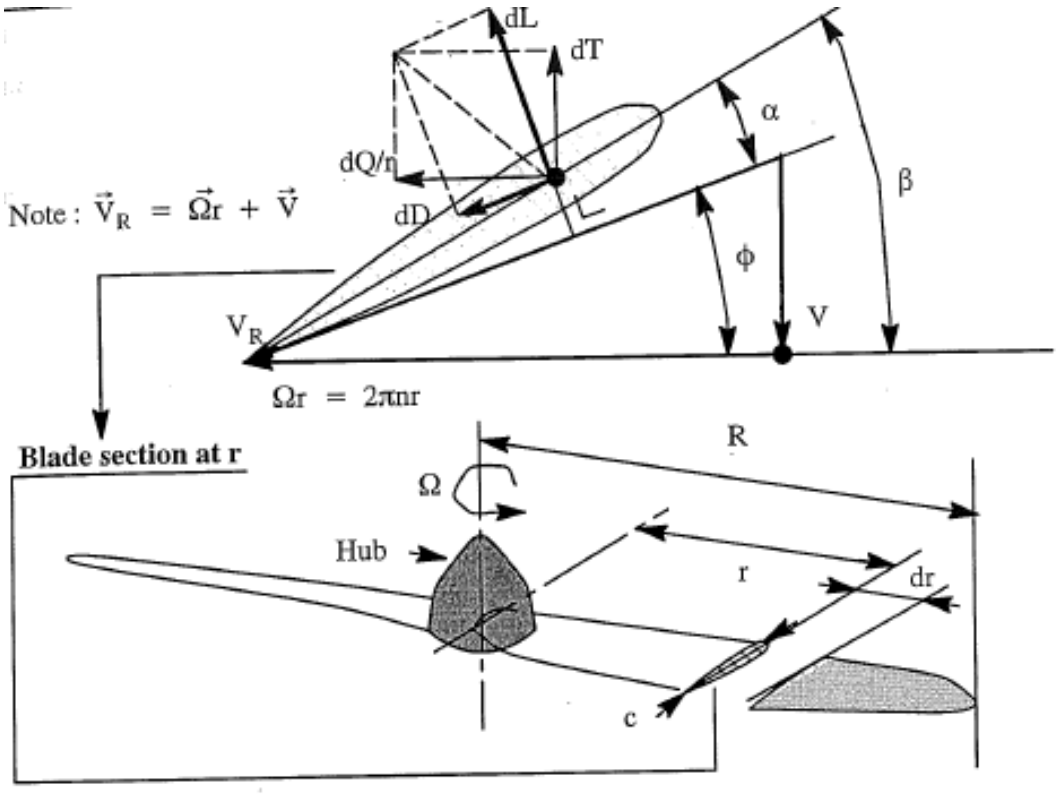

Figure 3.6 Propeller BET Geometry [30]

The aircraft speed, V, is assumed to be constant along the blade. The resultant velocity seen by the blade is a combination of the angular velocity, Ωr, and the aircraft velocity V. A geometric twist of β is required near the hub to adjust for the AOA to prevent stall. With these parameters known, the blade element thrust, torque, and efficiency can be calculated as follows where dr is the cross-section width for the element.

$$dT = dLcos\Phi - dDsin\Phi = \frac{1}{2}\,\rho V_R^2\; c\; dr\; (c_l cos\Phi - c_d sin\Phi) \tag{3.18}$$

$$dQ = (dLsin\Phi + dDcos\Phi)r = \frac{1}{2}\,\rho V_R^2 c\; r\; dr\; (c_l sin\Phi + c_d cos\Phi) \tag{3.19}$$

$$\eta = \frac{VdT}{\Omega dQ} = \frac{V(c_l cos\Phi - c_d sin\Phi)}{\Omega r(c_l sin\Phi + c_d cos\Phi)} = tan\Phi\,\frac{(c_l cos\Phi - c_d sin\Phi)}{(c_l sin\Phi + c_d cos\Phi)} \tag{3.20}$$

The final process would involve integrating Eqs. 3.18 -3.20 over the blade radius, R, and over the total number of blades on the propeller. The results yield the total force generation of thrust, torque, and efficiency. While this may be a practical method it does not account for velocities due to propeller rotation.

Blade Element Momentum Theory

Blade element momentum theory (BEMT) is a result of combining the BET and momentum theory. BEMT uses induced flow parameters that are a result of the lift produced from the propeller blade. The total elemental thrust determined by the BET provided

$$BdT = BdL\cos\varphi_0 = Bc_l 0.5\rho V_{R0}^2\, cdr\cos\varphi_0 \tag{3.21}$$

$$BdT = \rho(2\pi dr)(V + V_i\cos\varphi_0)(2V_i\cos\varphi_0) \tag{3.22}$$

By equating 3.21 and 3.22, Eq. 3.23 is as follows

$$V_i = \frac{Bc_l c V_{R0}^2}{8\pi r(V + V_i\cos\Phi_o)} \tag{3.23}$$

where B is the number of blades, c_l is the lift coefficient, r is the radius, c is the chord, V_i is the axial induced velocity, Φ_o is the resultant flow angle before accounting for induced velocity, and resultant velocity V_{R0}. Figure 3.7 shows the propeller BEMT angles. These angles ultimately determine the thrust and torque from the elemental equations for a propeller of B number of blades.

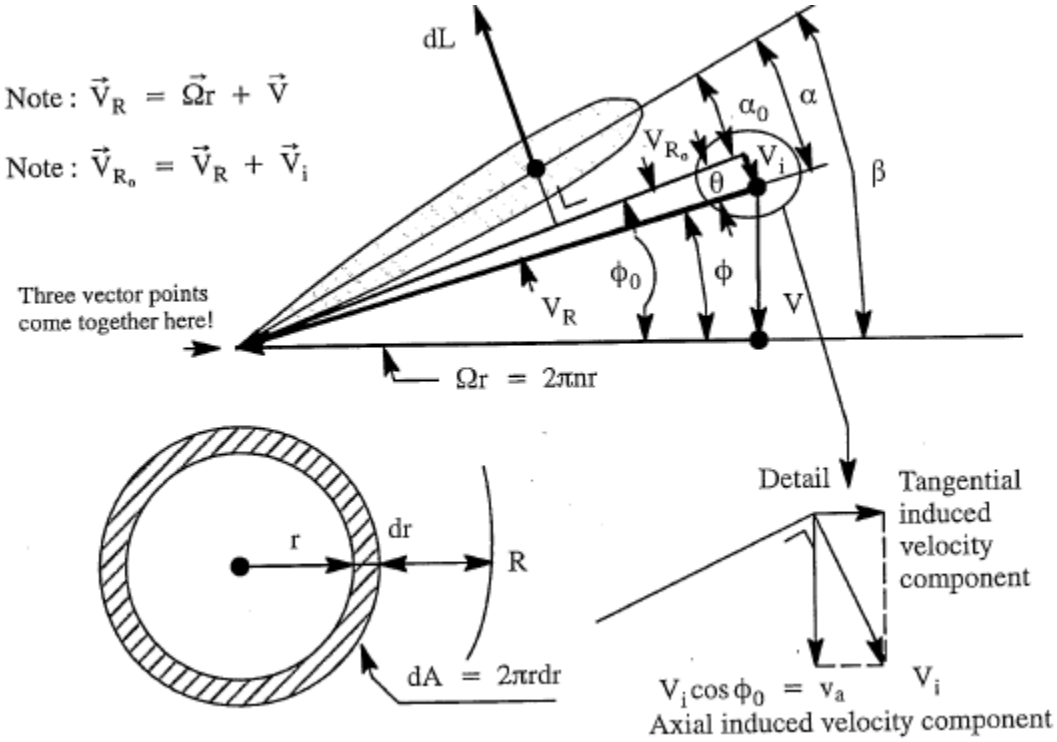

Figure 3.7 Propeller BEMT Angles [30]

If the induced flow angle θ is assumed to be small, then Eq. 3.23 can then be simplified to

$$\sin(\Phi) = \sin(\Phi_o + \theta) \approx sin\Phi_o + \theta\, cos\Phi_o \tag{3.24}$$

$$tan\theta = V_i/V_{R0} \approx \theta \tag{3.25}$$

$$c_l = a_0\alpha_o = a_0(\beta - \Phi_o - \theta) \tag{3.26}$$

Re-arranging Eq. 3.24 – 3.26 and combining Eq. 3.23 yields Eq. 3.27 where a_0 corresponds to the element section lift curve slope of the blade airfoil. The induced angle then follows

$$\theta \approx B\left(\frac{c}{8\pi r}\right)\frac{a_0(\beta-\Phi_o-\theta)}{sin\Phi_o+\theta cos\Phi_o} \tag{3.27}$$

The induced angle still remains unknown. The solidity ratio σ and non-dimensionalized blade station x must be introduced to re-arrange Eq. 3.27. The solidity ratio relates the total blade area to the disk. Assuming a constant chord yields the following

$$\sigma = \frac{BcR}{\pi R^2} = \frac{Bc}{\pi R} \tag{3.28}$$

$$x = \frac{r}{R} \tag{3.29}$$

$$\theta^2 cos\Phi_o + \theta\left(sin\Phi_o + \frac{\sigma a_0}{8x}\right) - \frac{\sigma a_0}{8x}(\beta - \Phi_o) = 0 \tag{3.30}$$

Solving Eq. 3.30 for the induced flow angle provides Eq. 3.31

$$\theta = \frac{1}{2\,cos\Phi_o}\left\{-\left(sin\Phi_o + \frac{a_0\sigma}{8x}\right) + \sqrt{\left(sin\Phi_o + \frac{a_0\sigma}{8x}\right)^2 + 4\,cos\Phi_o\frac{a_0\sigma}{8x}(\beta - \Phi_o)}\right\} \tag{3.31}$$

Knowing the induced flow angle, Eq. 3.32 – 3.34 are assumed and Eq. 3.35 – 3.36 are observed from Figure 3.6. The induced velocity is found using Eq. 3.37 where V_t corresponds to the propeller tip speed.

$$cos\Phi_o \approx 1 \tag{3.32}$$

$$sin\Phi_o \approx \frac{V}{V_R} \approx \frac{V}{xV_t} \tag{3.33}$$

$$V_R = xV_t \tag{3.34}$$

$$\frac{V_i}{V_R} = tan\theta \tag{3.35}$$

$$V_i \approx \theta V_R \approx xV_t\theta \tag{3.36}$$

$$V_i = V_t\left\{-\left(\frac{V}{2V_t} + \frac{a_0\sigma}{16}\right) + \sqrt{\left(\frac{V}{2V_t} + \frac{a_0\sigma}{16}\right)^2 + \frac{a_0\sigma\beta x}{8} - \frac{a_0\sigma V}{8V_t}}\right\} \tag{3.37}$$

However, Eq. 3.37 is better suited for high thrust applications while Eq. 3.30 is best suited for propellers when the θ^2 is neglected. In doing so, Eq. 3.30 reduces to

$$\theta = \frac{\beta - \Phi_o}{1 + \frac{8x sin\Phi_o}{\sigma a_0}} \tag{3.38}$$

From Fig. 3.7, the relation for Eq. 3.39 could be found. Lastly, Eq. 3.40 yields the elemental thrust for a propeller of B blades while the elemental torque can be found with Eq. 3.41. Most propeller design programs use BEMT and although this is a robust theory, it is limited to two dimensions for an airfoil cross-section.

$$V_{R0} = V_R cos\theta = \left(\frac{2\pi nr}{cos\Phi}\right) cos\theta \tag{3.39}$$

$$dT = B(dLcos\Phi_0 - dDsin\Phi_0) = \frac{1}{2} B\rho {V_{R0}}^2 cdr(c_l cos\Phi_0 - c_d sin\Phi_0) =$$

$$B\rho \left(\frac{2\pi^2 n^2 r^2}{cos^2\Phi} cos^2\theta\right) cdr(c_l cos\Phi_0 - c_d sin\Phi_0) \tag{3.40}$$

$$dQ = B(dLsin\Phi_0 + dDcos\Phi_0\Phi) = \frac{1}{2} B\rho W^2 crdr(c_l sin\Phi_0 + c_d cos\Phi_0) =$$

$$B\rho \left(\frac{2\pi^2 n^2 r^3}{cos^2\Phi} cos^2\theta\right) crdr(c_l sin\Phi_0 + c_d cos\Phi_0) \tag{3.41}$$

Airfoil Noise

With the sUAS operating in either urban or military environments, the reducing noise generation must be a priority. There are typically six forms of generated airfoil noise that have been addressed through the works of Brooks et al. [15]. Brooks et al. discussed the importance of distinguishing, within the overall broadband noise, the different ways the airfoil generates noise. The first classification of airfoil self-noise would be the turbulent boundary layer-trailing edge noise. This type of noise typically occurs at high Reynolds

numbers. The turbulent boundary layer begins to develop, as seen in Fig. 3.8, and the interaction of turbulence over the trailing edge produces high-frequency noise. The second source of airfoil noise would be the laminar-boundary-layer vortex shedding noise. At low Reynolds numbers, laminar boundary layers develop. The laminar boundary layers provide instability in the flow which produces vortex shedding in the airfoil wake. This vortex shedding interaction with the trailing edge produces noise. The third source of airfoil noise would be the boundary layer separation. Boundary layer separation occurring near the trailing edge results from flow separation on the upper surface of the airfoil. The combination of boundary layer separation and trailing edge turbulence produces the noise for this case.

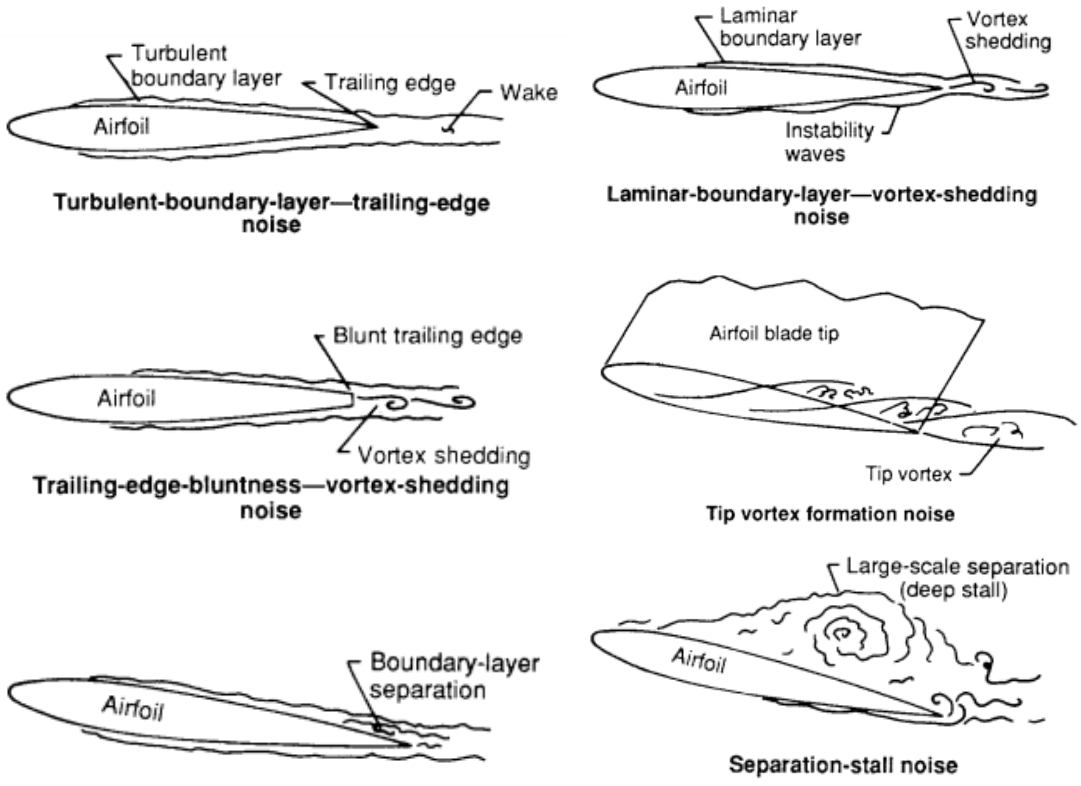

Figure 3.8 Airfoil Noise Classifications [15]

The fourth source of possible airfoil noise would be the separation-stall noise which results from deep stall and at a very high AOA. The separation-stall noise primarily causes low frequency noise. The fifth source of airfoil noise would be due to the trailing-edge-bluntness-vortex shedding noise, as a blunt trailing edge does not have a streamline profile. This is also characterized as having low frequency noise. The last source of noise considered is produced by the tip vortex formation at the edge of the airfoil which would also occur at the tip of a propeller blade. This noise source produces highly turbulent flow from the vortex eddy perturbations.

Defining Near and Far Field Noise Measurements

When measuring noise, it is important to know that noise behavior changes with distance which produces different sound fields. Sound pressure level (SPL) is an acoustic definition denoting the effective pressure of a sound to a reference value that is measured in decibels (dB) [34]. As distance increases, sound pressure decreases by a factor of 6 dB as the distance doubles which corresponds to a 50% SPL decrease. Equation 3.42 displays the SPL definition where p is the pressure level and p_0 is the reference pressure. Equation 3.43 calculates the difference in pressure levels to compare actual and predicted data of sound pressure decay rates, representing the "distance law" as it pertains to the standard decay rate.

$$SPL = 20\log_{10}\left(\frac{p}{p_0}\right) \tag{3.42}$$

$$SPL_2 = SPL_1 - \left|20\log_{10}\left(\frac{r}{r_1}\right)\right| \tag{3.43}$$

Figure 3.9 shows the distinctions of sound fields with increasing distance. More importantly, it illustrates the near and far field expected sound level trends. The near field exhibits higher sound levels and the far field appears approach background noise levels. In the literature, definitions of the near and far field are not clear. It is commonly agreed that the far field begins when doubling the distance produces an SPL reduction of 6 dB [35-37]. This transition to the far field does not have a clear distinction and will be investigated further in Chapter Five.

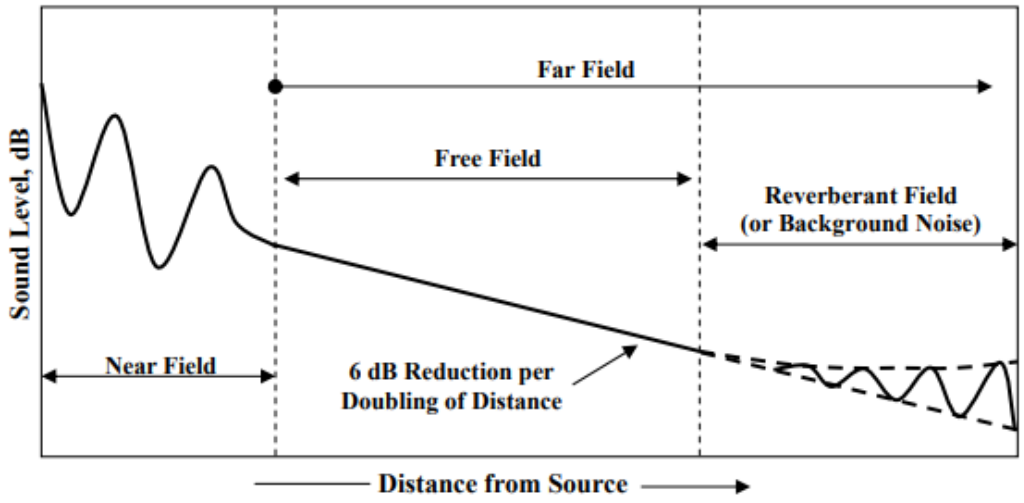

Figure 3.9 Distinctions of Sound Fields with Increasing Distance [35]

Sound can be described in terms of different weighting indexes [38]. A-weighted noise measurements (dBA) are the most common because they simulate what would be heard from a human ear [39]. A-weighted noise SPL is regarded as being a good representation to quantify environmental noise annoyance due to its low frequency [38]. The low frequency noise is the dominant noise that the human ear receives. Therefore, this study measures with dBA SPL measurements for sUAS propellers. This would best simulate sUAS noise in urban and military environments.

Bell-Shaped Lift Coefficient Distribution

This section will present a discussion of the theoretical background behind the Prandtl bell-shaped lift distribution as described by Bowers et al. [22,40].

Biomimicry and Proverse Yaw

Ludwig Prandtl's lifting line theory, as discussed earlier, has been the basis for how lift distributions have been applied throughout the history of flight. In Bowers et al.'s work, Prandtl's bell-shaped lift distribution came as a result of following biomimicry. A bird's method of flying and generating lift is different than what is found on an airplane wing. Furthermore, Bowers et al. used proverse yaw to prove the concept of the bell-shaped lift distribution. Figure 3.10 illustrates the yaw moments and the axis orientation for a typical aircraft.

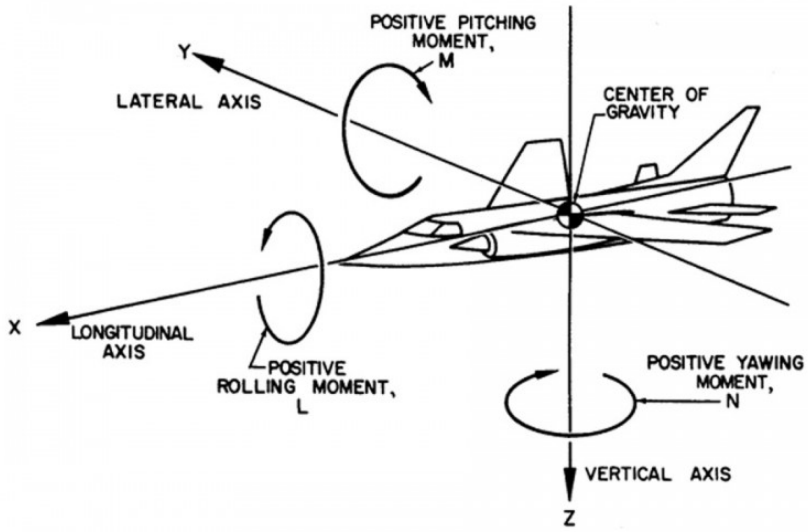

Figure 3.10 Axis Orientation Displaying Yaw Moment [41]

Yaw occurs on an aircraft when the vertical tail deflection of flow creates a yawing moment about the vertical axis. In Fig. 3.10, the yawing moment occurs about the vertical

z-axis. By manipulating thrust and drag at the wing tips Bowers et al. was able to control the yawing moment without the need of a vertical tail.

Bell-Shaped Lift Distribution

Bowers used the circulation theory of lift to develop his lift distribution Eqs. 3.62-3.66. In Bowers' terms, the bell-shaped lift distribution solution is where L is the nondimensional load (circulation distribution) and x is the span location from 0 to 1. Equation 3.63 is the non-dimensional downwash angle of the flow. The downwash, DW, represents the downward deflection of flow behind the wing which is a way to describe tip vortex behavior as well.

$$\mathrm{L} = (1 - x^2)^{3/2} \tag{3.62}$$

$$\mathrm{DW} = \frac{3}{2}(x^2 - \frac{1}{2}) \tag{3.63}$$

Limits applied to the distribution make the lift approach zero at the wingtip. The slope of the lift curve (function of span) approaches zero at the wingtip. Lastly, Eq. 3.66 displays the slope of the upwash curve (function of span) at the wingtip is equal on both sides of the wingtip.

$$\lim_{x:0\to b/2} L(x) = 0 \tag{3.64}$$

$$\lim_{x:0\to b/2} \frac{dL(x)}{dx} = 0 \tag{3.65}$$

$$\lim_{x:0\to b/2} \frac{dDW(x)}{dx} = \lim_{x:\infty\to b/2} \frac{dDW(x)}{dx} \tag{3.66}$$

CHAPTER FOUR

Experimental Method and Setup

This chapter details the experimental method and setup used within this study. The first part of this chapter will contain the propeller design procedure. The following sections will discuss the experimental measurement procedures in addition to the USAFA and Baylor testing facilities, respectively. Lastly, a description of the uncertainty analysis of the measurements in the experiments will be addressed.

Propeller Design

The propeller design process in this study began with establishing the design point parameters that would best fit the desired operating conditions of the UAS. Factors of weight and airfoil thickness became important design factors. It should be noted that the USAFA and Baylor experiments had different design points for their propeller design and testing objectives. As such, their respective propeller design parameters will be discussed separately. However, the USAFA and Baylor experiments both began with utilizing the Baylor Bearcontrol guided user interface (GUI) designed by Trae Liller [42] to design propellers.

The Bearcontrol MATLAB code was used mainly to produce a physically modeled propeller that would be 3D printed. Propellers, printed on the Objet 30 in the Baylor Machine Shop, were printed out of acrylonitrile butadiene styrene (ABS). This program is a comprehensive propeller design program that allows the user to specify design conditions for a specific airfoil. It would then use the QMIL and QPROP performance analysis tools,

developed by Drela, to iterate the aerodynamic characteristics of the airfoil to match the propeller design requirements [43-46]. The QMIL and QPROP programs utilize the BEMT propeller theory discussed in Chapter Three. Upon execution of QMIL the output file was then used as the input file for the QPROP program. When these programs were completed, Bearcontrol would then generate a series of SolidWorks macros that would construct the planes and airfoil cross sections for the propeller blade. A propeller hub or dovetail was then added to the propeller blade. The Bearcontrol program designed propellers to operate with minimum induced loss and not minimum induced drag. As discussed in Chapter Three, the minimum induced drag concept applied to propellers would allow the design to unload the tip. Since Bearcontrol was incapable of accommodating the new design considerations, a Microsoft Excel spreadsheet was used to design propellers with minimum induced drag. The Excel spreadsheet was essential for designing propellers with specified lift distribution changes to improve the propeller aerodynamic and aeroacoustic performance.

USAFA Experimental Setup: North Low-Speed Wind Tunnel

The experiments carried out at the USAFA Department of Aeronautics labs were performed to define the near and far field of the test propellers. This testing consisted of acoustic measurements in an open loop wind tunnel and an anechoic chamber. The wind tunnel experiments were conducted in the USAFA North Low-Speed Wind Tunnel. This wind tunnel was an Engineering Design Laboratory, Inc. tunnel with a test section 36” x 36” x 40” (91.44 cm x 91.4 cm x 101.60 cm) that has a top speed of approximately 108 ft/sec (32.92 m/s). All propeller tests conducted in the wind tunnel were at static conditions to simulate the hover of a quadcopter. The propellers used in this experiment were a

diameter of 9.4 inches. Therefore, wind tunnel corrections were not necessary for experiment data analysis as the propeller diameter blockage area was small compared to the tunnel cross section area. Figure 4.1 shows the test stand used to conduct the USAFA wind tunnel experiments.

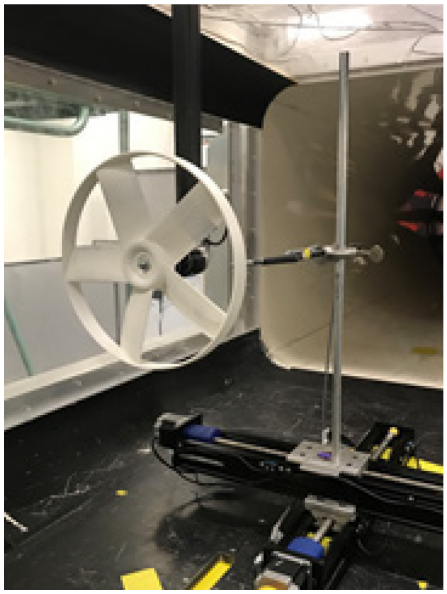

Figure 4.1 USAFA Wind Tunnel Test Stand

The USAFA wind tunnel test stand was comprised of a cantilevered system that extended down from the top of the wind tunnel. This test stand was comprised of the motor, propeller, the MRTP-0.2Nm torque cell, the thrust load cell model MBI-5 (5 lb_f), and the Monarch Instrument ACT-3X-1-1-1-0-0-0 optical sensor. The power inputs were provided by an Agilent E633A power supply, capable of 20 VDC and 10 A, used to power the single motor. A HP 6274B DC Power Supply, capable of 40 VDC and 10 A, was used for specific cases where higher power demands were needed. The transducers were powered by An Agilent E3631 capable of 0-6V and 5A. The current was measured by the PowerTEK Current Meter, capable of 20A and 24VDC. Atmospheric conditions for pressure and

temperature were measured with a HEISE Model PM. The ACT-3X-1-1-1-0-0-0 tachometer optical sensor and RPM digital display measurements were verified with a Digital Strobescope ESL-20. For the microphone placement control, a two-axis Velmex Traverse was used to move the microphone in the radial and axial directions downstream of the propeller plane of rotation. Data acquisition measurements were recorded from a VXI Agilent E14121B Mainframe version E1413C that was capable of 64 channel scanning analog to digital conversion. This system was used to record and store measurements of thrust, torque, noise, current, and RPM.

Wind Tunnel Testing Procedure – Radial Microphone Traverse

The USAFA wind tunnel experiments investigated propeller acoustic performance and electrical efficiency of three motors. The propeller comparison testing examined the aero-acoustic effects by accomplishing RPM sweeps. The RPM sweep was completed in increments of 300 RPM from a range of 2000-6900 RPM. This RPM range allowed the propeller to achieve thrust values above and below 0.7 lb_f, which was the design point thrust for one propeller in static hover. This process determined the RPM for 0.7 lb_f and this RPM was then used for the microphone traverse measurements. For the microphone traverse measurements, the microphone was pointed into the flow at a location of an r/R of 0.8 and 1 inch directly behind the propeller at the height of the hub. The microphone was traversed radially outwards from the hub to past the tip of the propeller in 0.1-inch increments from a range of 0.3-1.3 r/R. The objective of the microphone traverse was to locate the peak SPL radial location for each propeller design and blade configuration. This would provide information about the streamtube and tip vortex interaction of the propeller and how its aeroacoustic effects change because of aerodynamic design considerations. At

the completion of the microphone traverse, the peak SPL radial location would be determined from the SPL data. All testing used the Bruel and Kjaer (B&K) handheld 2270 analyzer along with Type 2670 ¼" microphone. The microphone was then moved to the peak SPL radial location, the RPM was held constant at 0.7 lb_f of thrust and a frequency spectrum was measured for 10 seconds with the B&K handheld spectrum analyzer. This procedure would be repeated for downstream distances of 1, 3, 6, 9, and 12 inches behind the propeller. Additionally, this procedure would be repeated for other propellers and blade configurations to characterize the near-field acoustic behavior.

Wind Tunnel Testing Procedure – Motor Efficiency

The experiments conducted in the USAFA North Low-Speed Wind Tunnel investigated the motor efficiency. The motor efficiency experiments used three motors: the stock DJI Phantom 2 960 Kv, Gartt 580 Kv, and Gartt 370 Kv. Additionally, the tests were conducted under static conditions using the same instrumentation and data acquisition as previously mentioned for the microphone traverse procedure. For most of the motor efficiency testing, a DJI Phantom 2 stock propeller was used. The motor efficiency compared in these experiments was defined as the ratio of the mechanical power measured to the electrical power used at the specified thrust, this will be discussed further in Chapter Five. The mechanical power is a function of the torque required to spin the propeller at the desired thrust and RPM. The electrical power is a function of the voltage and current, delivered to supply the power needed to achieve a desired thrust and RPM. The procedure began with integrating the test motor into the test stand, the stock propeller, and then an RPM sweep. The emphasis was on the thrust in relation to the mechanical and electrical power. Several RPM sweeps were made at different input voltages within the limits of the

motor's operating range. The Gartt 370 Kv had a voltage range of 18 VDC to 22.2 VDC. The Gartt 580 Kv had a voltage range of 11.8 VDC to 14.8 VDC. The stock DJI Phantom 2 motor had a voltage range of 8.32 VDC to 17.5 VDC.

USAFA Experimental Setup: Anechoic Chamber

The anechoic chamber tests in this study were conducted at the USAFA anechoic chamber. The USAFA anechoic chamber is an L-shaped design with the longest dimensioned side measuring 30'x14'x14' and the shortest side measuring 20'x14'x14'. The chamber is comprised of acoustic foam capable of absorbing 2GHz and higher radio frequencies. The test stand was placed on a tripod to stabilize the thrusting forces of the single propeller and hexacopter configuration. This can be seen in Fig. 4.2.

Both test stands were oriented with the plane of the propeller rotation to be perpendicular with the ground on a turntable with 360-degree rotation capabilities. Additionally, the center of both test stands was placed 5 feet above the surface at the center of rotation.

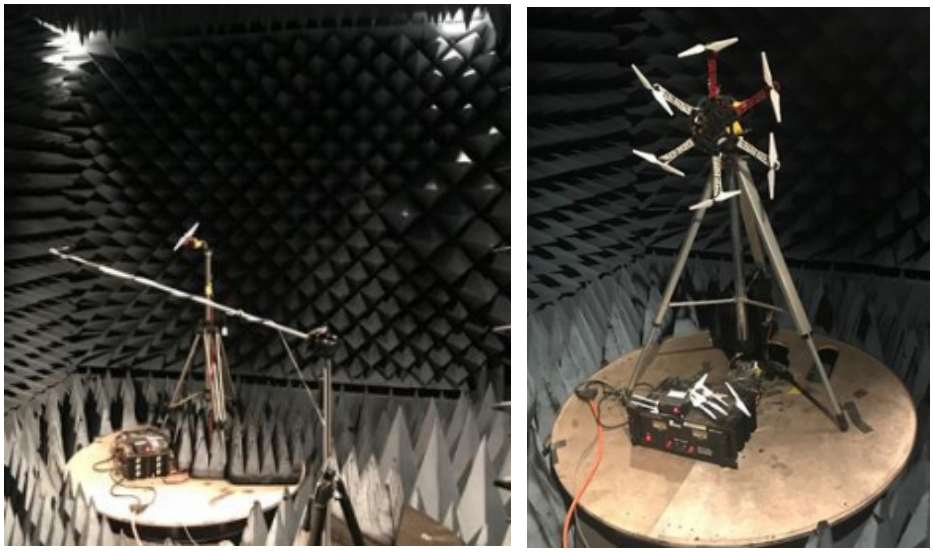

Figure 4.2 USAFA Anechoic Chamber Single and Hexacopter Test Stands

The single propeller test stand was comprised of the experimental or stock propeller, the stock DJI Phantom 2 2312 960Kv motor and a custom aluminum adapter mount. The test stand also had a Castle Creations Phoenix Edge Lite 130 25V 130-amp Brushless ESC with a 5-Amp BEC, ACT-3X-1-1-1-0-0-0 tachometer optical sensor, and a Spektrum DX5e 2.4 GHz DSM2 remote paired with an AR6100 Microlite Park flyer receiver. A PS-86KX Pyramid Regulated Power Supply was used to provide the appropriate electrical power to the motor. This power supply was capable of 13.8 VDC and 80 amps; for all experiments in the USAFA anechoic chamber the voltage was held to 11.4 VDC.

The hexacopter test stand was comprised of the DJI Flame Wheel F-550 frame that had six DJI 2312E 960Kv motors with six E series 420 Lite Electronic Speed Controllers. The same optical sensor and power supply from the single propeller test stand were also used on the hexacopter stand. The hexacopter experiments used the E-Flite EFLR310013 receiver to control the propellers.

For the near and far field measurement, the microphone was moved to distances from 1-24 feet. The microphones were placed pointing to the centerline of rotation. The data acquisition system used for recording the anechoic chamber measurements was a National Instruments USB X Series 6351. A LabVIEW virtual instrument (VI) was created to convert the analog signal to a digital signal. Figure 4.3 shows the VI front panel that controlled the data acquisition for the anechoic chamber testing.

This VI was designed to acquire 5,000 samples for a sampling rate of 1,000 samples per second for a total time of 5 seconds. Additionally, these samples were averaged while additional data was taken for the sample statistical data. This VI was able to acquire the

data for the SPL and RPM measurements. The programming details can be seen in Appendix C.

Figure 4.3 USAFA Anechoic Chamber LabVIEW VI

Anechoic Chamber Procedure

The procedure used for the anechoic chamber testing was the same for both the single propeller and hexacopter experiments. The objective of the anechoic chamber was to achieve a steady state RPM and acoustic measurement for an RPM sweep. The RPM sweeps for the anechoic chamber followed the same procedure used for the USAFA Wind Tunnel RPM sweeps. To begin, the DJI Phantom 2 stock propeller(s) and tripod were placed on the turntable. For every test, the SPL measurements began with a baseline

background noise measurement in which all systems were disabled to establish the baseline conditions. The background noise measurement would then be subtracted from the measured value with the propeller activated as mentioned in Chapter Two. All testing would be completed under static conditions to best simulate static hover conditions of a quadcopter UAS.

The microphone was placed at the testing distance specified and the orientation of the propeller plane was rotated with the turntable to the specified orientation from 0 to 180 degrees. A tape measure and laser range finder were used to verify the location of the microphone distance. The propeller azimuth orientation would be verified using the turntable controller software in the anechoic chamber control room. Then the power supply, test stand electronic speed controller, and the receiver were activated in that order. The RPM and noise measurements would be measured with an RPM sweep from a range of 2000-6900 RPM in increments of 300 RPM. At each point, a single measurement would be made when the RPM and noise were steady. An instantaneous LAF SPL measurement was taken to obtain the A-weighted dB sound level. An exponential average from the B&K analyzer would provide the single noise measurement. The LabVIEW VI would then record the SPL measurements. Upon completion of the RPM sweep, the RPM would be set for a thrust setting of 0.7 lb_f and a frequency spectrum measurement was recorded for a duration of 10-15 seconds. The power supply and receiver were then disabled, and the DJI Phantom 2 stock propeller would be replaced by the Trailing Edge Notch propeller. The tests would then be repeated. After the sound and frequency measurements were completed for both propellers, the platform would be rotated 30 degrees which would rotate the orientation of the propeller by the same margin. The platform would then remain in a

fixed position once the desired orientation was achieved. The entire data collecting process would be repeated for each test stand orientation from 0 to 180 degrees. Symmetry was validated with prior testing, so the orientation was limited to 180 degrees instead of 360 degrees.

For the testing that involved varying distances, the previous testing process was repeated for all distances from the propeller. The single propeller test stand was tested at orientations of 0, 90, and 180 degrees for distances of 1, 3, 5, and 9 feet. Angles of 180 and 0 degrees were used for comparing the sound decay measurements from 1-14 feet in 1-foot increments. Distances of 18-24 feet required 2-foot increments. The hexacopter test stand would use orientations of 0, 90, and 180 degrees at distances of 2, 5, and 10 feet.

Baylor Experimental Setup

The experimental testing conducted at Baylor University took place at the Baylor Research Innovative Collaborative (BRIC) Aerothermodynamics Lab low-speed wind tunnel. Figure 4.4 displays the wind tunnel below which is an Engineering Laboratory Design (ELD), Inc. Model 406B.

Figure 4.4 Baylor Low-Speed Subsonic Wind Tunnel

This particular model was capable of obtaining freestream velocity speeds up to 165 ft/s ±1%, and a turbulence intensity less than 0.2%., with a testing volume of 24”x24”x48”. The wind tunnel utilized a test stand where the propeller was pointing into the flow with a cantilevered design in which the motor was mounted to the torque and thrust transducers. Figure 4.5 shows the test stand system used for this experimental setup. Appendix A shows the system diagram associated with the wind tunnel testing.

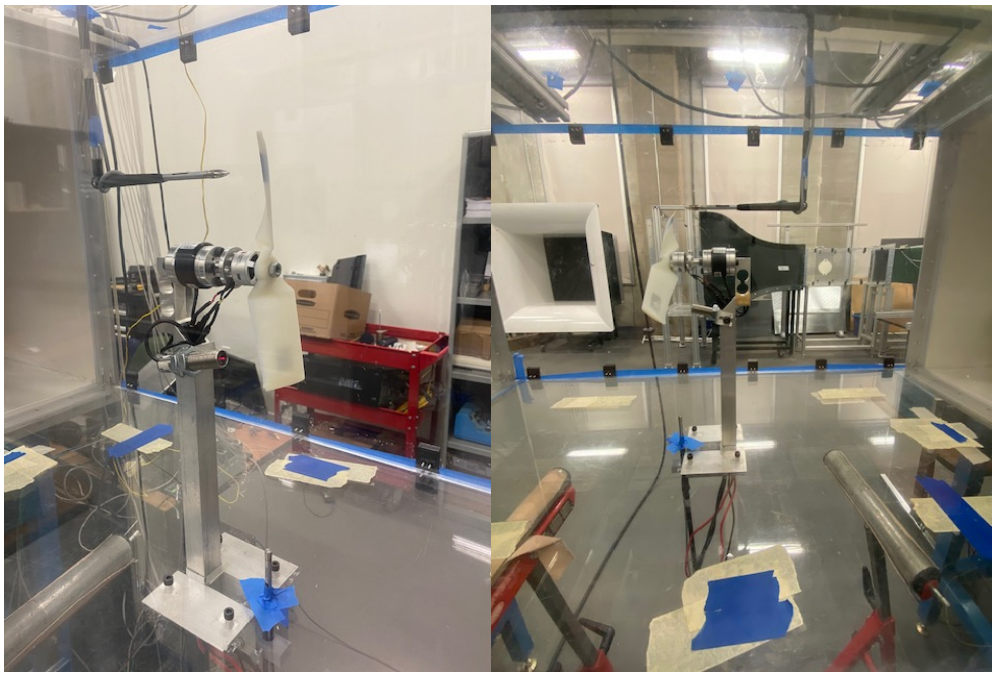

Figure 4.5 Baylor Wind Tunnel Propeller Test Stand

A series of instruments were used to measure the torque, thrust, and RPM that were all mounted to the test stand. An Interface MRT-0.2Nm Torque Transducer, capable of a 1.77 in-lb_f, was used to measure the torque of the propeller. An LSP-1 Load Cell, capable of 2.2 lb_f, was used to measure the thrust of the propeller. Two different custom motor mounts were used to safely attach the motor to the propeller and the test stand. The first

mount corresponded to the airfoil testing with the DJI Phantom 2 motor which was a custom aluminum design, seen in Fig. 4.5 above. The second mount was for a motor supplied by the USAF Academy, and was a custom 3-D printed motor mount. An Omega HHT20-ROS Remote Optical Sensor was used to measure the RPM with a range of 1-250,000 RPM. The Monarch Instrument ACT-3X-1-1-1-0-0-0 Tachometer, shown in Fig. 4.6, would provide a digital reading of the measurement.

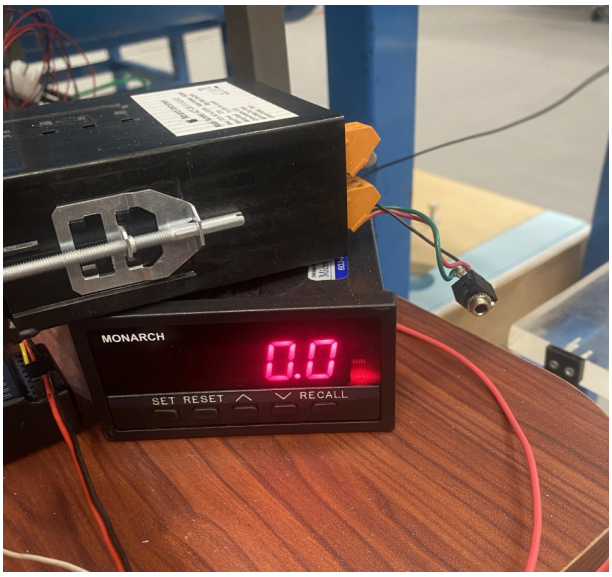

Figure 4.6 Monarch Instrument ACT-3X-1-1-1-0-0-0 Tachometer

Also seen in the previous images would be the Bruel and Kjaer 4938-A-011 ¼" Pressure Field Microphone with the attached nose cone, and the microphone aft of the propeller. The nose cone was attached to the microphone and pointed directly into the flow. The streamlined nose cone was used to mitigate stagnation pressure so the microphone SPL measurements would be measured directly without interference. This microphone system utilized an analog output voltage in a range of 0-4 V that was proportional to the SPL in dBA at a range of 0-200 dBA. The Bruel and Kjaer microphone was paired with a Type

2270 Handheld Analyzer, displayed in Fig. 4.7 below, which provided the ability to change the acoustic settings, recording, and provide a real-time display of the data. The analog voltage signal would be transferred from the B&K 2270 to the data acuistion to obtain the SPL measurement.

Figure 4.7 Bruel and Kjaer Type 2270 Handheld Analyzer

The PowerTEK Current Meter is shown below in Fig. 4.8, where the left side leads connect to an inductance ammeter and the right side connects to the B&K 1761 Power Supply and the data acquisition module. A Bruel and Kjaer Precision XLN3640 DC Power Supply (0-36V and 0-40A) was used as the power source for the test stand motor. The XLN3640 power supply used programmable inputs to hold either voltage or current settings constant while in use. The testing in this report used a constant voltage setting while the current could adjust according to the power demand. A B&K Precision 1761 DC

Power Supply (0-35V and 0-3A) was used to power the PowerTEK Current Meter. The PowerTEK Current Meter, capable of 20 A and 24 VDC, was used to measure the current for the data acquisition system. Both power supplies are shown with Fig. 4.9. A constant voltage setting of 20V was used for the testing in this report.

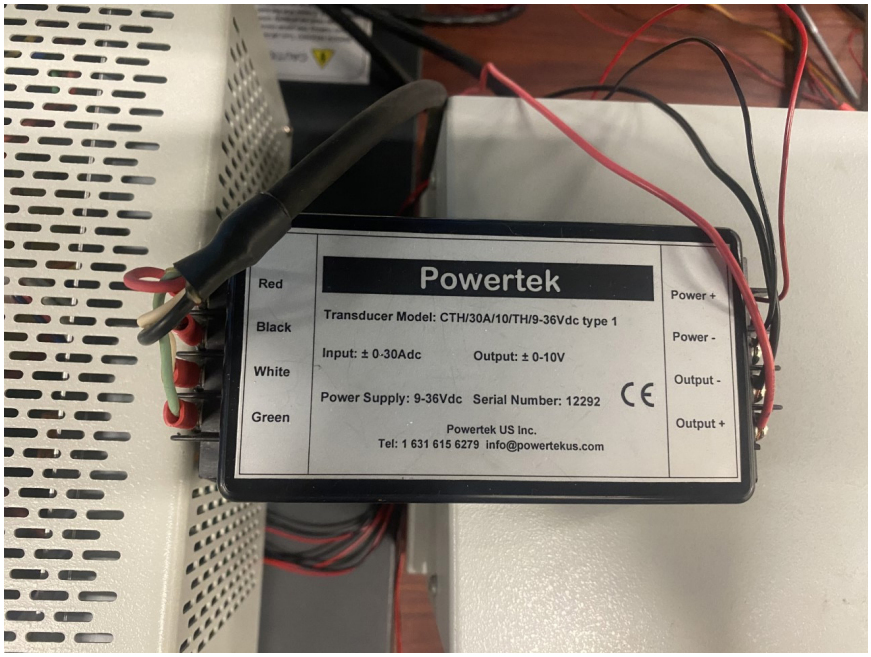

Figure 4.8 PowerTEK Current Meter

Figure 4.9 Bruel and Kjaer Precision XLN3640 DC (bottom), Bruel and Kjaer Precision 1761 DC Power Supply (top)

Two Global Specialties Model 1301 Power Supplies, shown in Fig. 4.10, were used to power the thrust and torque transducers. These two power supplies were both set to a constant voltage setting of 10 V. An Omega iBTHX sensor was used for recording atmospheric pressure and temperature conditions. Velmex BiSlide Traverse's were used to move the microphone closer or further away from the propeller at a fixed r/R location, or to measure the sound according to the propeller blade r/R location. The Velmex BiSlide Controllers, shown in Fig. 4.11, were capable of being programmed and moved with precision up to 0.003 inches and repeatable up to 0.0002 inches. Each controller allowed the microphone to be moved in the horizontal and vertical directions. Additionally, the controllers were linked together for ease of manual movement so they could be moved from controller shown left as the main drive system. These controllers were run by the Velmex software COSMOS to use in the wind tunnel for precise movement.

Figure 4.10 two Global Specialties Model 1301 Power Supplies

Figure 4.11 Velmex BiSlide Traverse Controllers

The wind tunnel upstream velocity measurements were collected with a pitot-static probe and an OMEGA PCL-2A pressure transducer displayed in Fig. 4.12. The probe was positioned approximately 17 inches upstream and 8 inches horizontally from the centerline of the propeller test stand such that it would not disturb fluid flow into the test stand.

Figure 4.12 OMEGA PCL-2A

A National Instrument (NI) CompactDAQ (cDAQ) was used to convert analog signals to digital and to acquire and store measurements. Thrust, torque, noise, current, and RPM were measured and stored utilizing this data acquisition system. The NI cDAQ 9178 Chassis and cDAQ modules can be seen in Fig. 4.13. The NI cDAQ 9178 Chassis provided multiple slot input and output modules for simultaneous operation. The cDAQ modules used were all NI cDAQ 9205 C series voltage input modules. From left to right the cDAQ modules housed signal wires corresponding to current, SPL, thrust & torque, and RPM. The power supply voltage could not be measured as these cDAQ modules were incapable of inputs greater than 10 V.

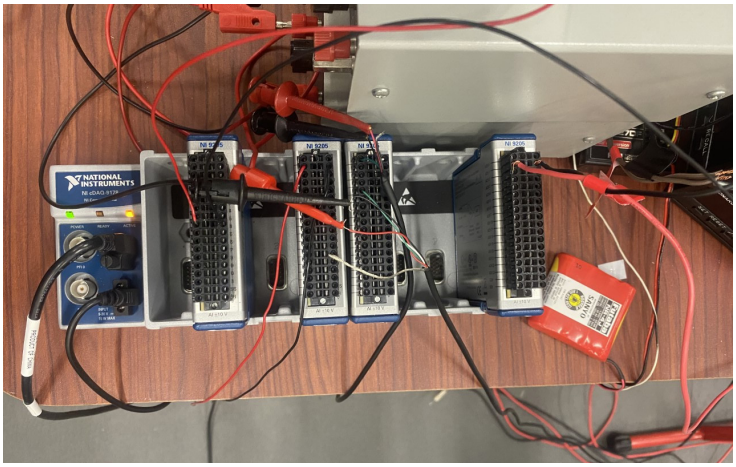

Figure 4.13 NI cDAQ 9178 Chassis and cDAQ modules

The propellers were controlled through an R/C model remote control system to best simulate UAS conditions. Figure 4.14 displays the Futaba T4EXA remote-control and its constituent Futaba FP-R127DF receiver. The receiver would be connected to the motor controller. The remote-control was capable of course adjustments and fine adjustments

(trim control) for its throttle settings. The consistency and versatility were useful in setting the RPM for RPM sweeps and traverse measurements.

Figure 4.14 Futaba T4EXA remote-control and FP-R127DF receiver

All instrument measurements were recorded with a LabVIEW Virtual Instrument (VI). Figure 4.15 displays the front panel of the Propeller Testing LabVIEW VI. The details of the block panel can be found in Appendix D. This VI records the measurements of thrust, torque, current, RPM, SPL, freestream velocity, PCL-2A pressure differential, temperature, relative humidity, and atmospheric pressure. In addition to the measurements, statistical data was also computed for the variance, standard deviation, and mean. Furthermore, options were built-in as inputs such that a second microphone reading could be recorded as well as the microphone traverse location and tunnel frequency setting. The real-time display also features the voltage waveform signal for several readings, shown at the bottom of Fig. 4.15. The data was recorded at 5000 samples for a rate of 1000 Hz and each measurement was averaged to then produce a single value. This was an appropriate range due to the high frequency produced by the propeller.

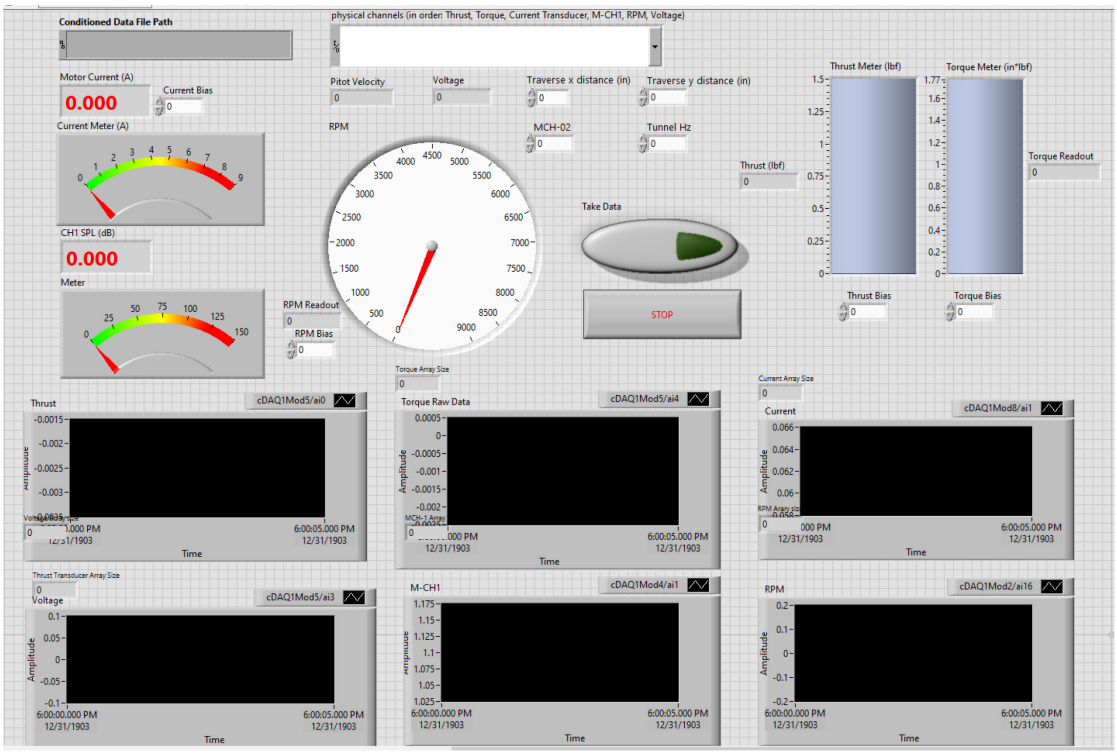

Figure 4.15 Propeller Testing LabVIEW VI Front Panel

Hardware Calibration

The thrust transducer, torque transducer, tachometer, current inductance ammeter and the microphone all required calibration before testing. The thrust and torque transducers were calibrated using an applied load in which voltage measurements were correlated to determine the desired output. To begin, the torque transducer calibration required removal of the motor and motor housing. The calibration adapter would be placed on the torque cell and a range of masses from 0-500g were hung on the arm. Figure 4.16 and 4.17 illustrates the torque transducer calibration arm. The voltage response to the mass would be recorded for each separate measurement once a steady state condition was achieved. The thrust transducer calibration utilized a wire and pulley for calibration and the same range of masses were applied to this system. This is shown in Fig. 4.17.

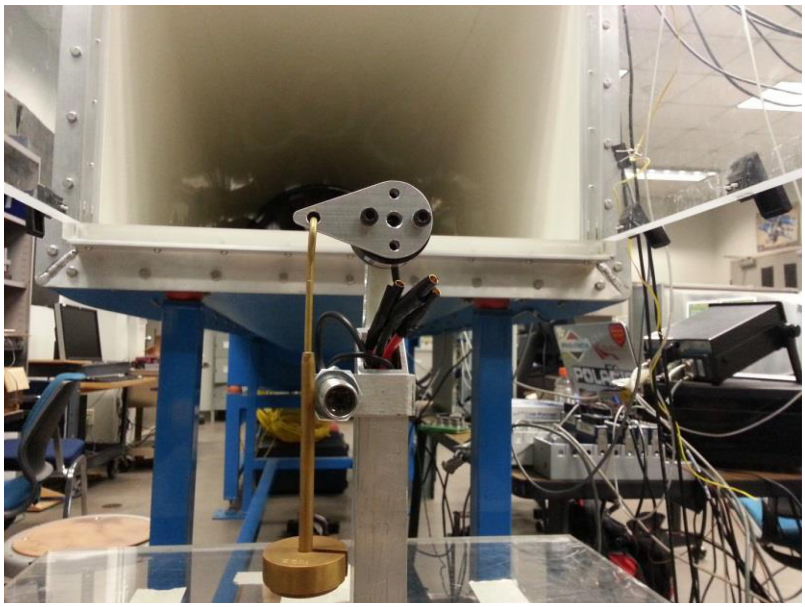

Figure 4.16 Torque Cell Calibration Arm

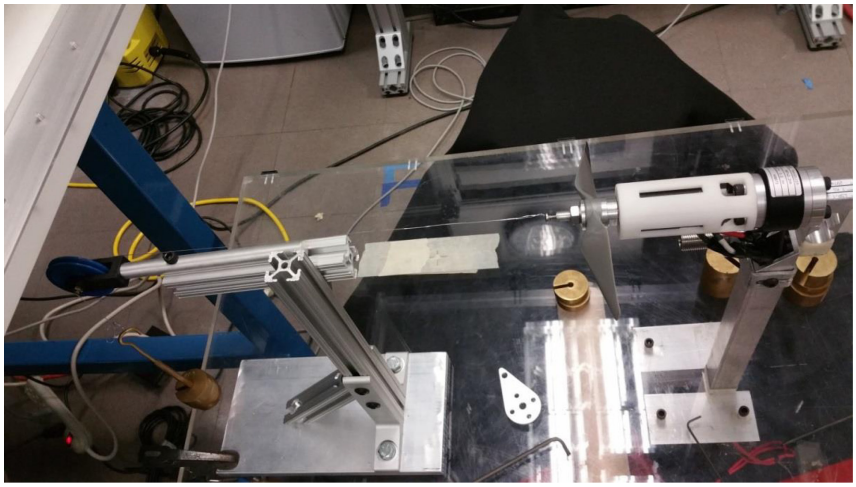

Figure 4.17 Load Cell Calibration Arm

All calibration instruments used the same VI. The corresponding input of mass, digital current, or RPM were recorded in the VI along with the measured the analog voltage. Figure 4.18 shows the LabVIEW Calibration VI and the programming details for this setup can be found in Appendix D. From the calibration values recorded, a calibration curve would be made similar to Fig. 4.19. The calibration constants would then be used to convert

the analog input voltage values to their corresponding output reading in the Propeller Testing LabVIEW VI.

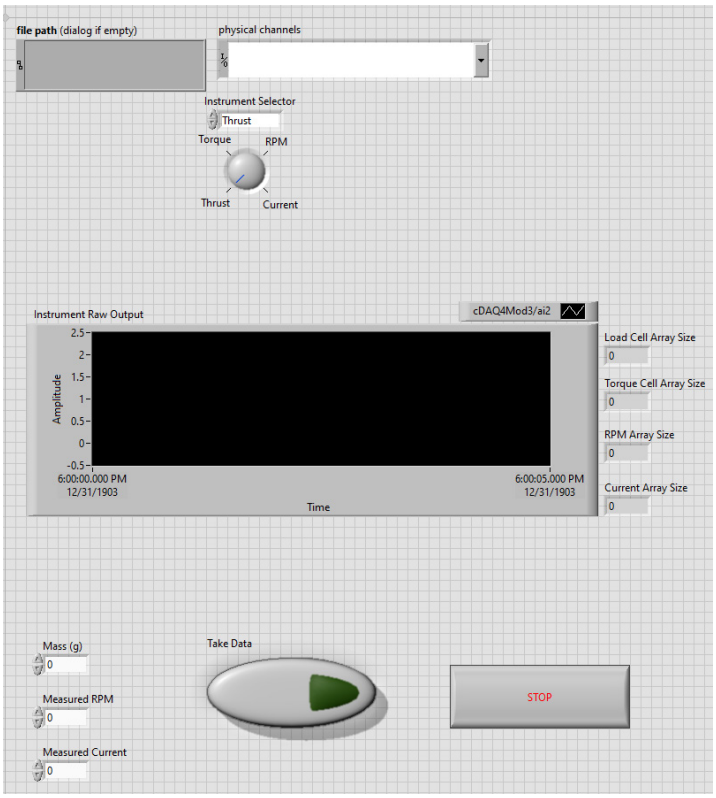

Figure 4.18 LabVIEW Calibration VI

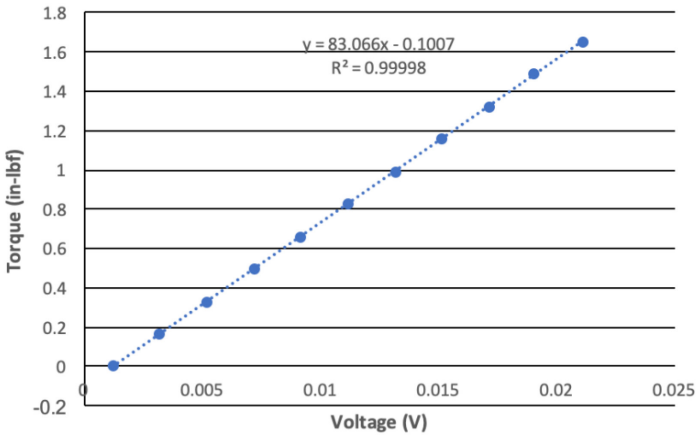

Figure 4.19 Typical Calibration Curve

The calibration process for the current and RPM was similar to the thrust and torque transducers, but digital measurements would be used instead of a known load. Figure 4.20 shows the panel tachometer calibration instruments with both the SHIMP Digital Stroboscope and the ESL-20 Digital Stroboscope. In the RPM calibration, the propeller would be operating at set RPMs and the stroboscope would then 'freeze' the rotor. The reading would be entered into the Calibration VI to obtain the analog voltage for that reading. A similar process was performed for the current ammeter, but the reading would be read directly from the power supply. The current ammeter would utilize inductance from the power supply to determine the current delivered.

Figure 4.20 ESL-20 (left) and SHIMP Digital Stroboscope (right)

Lastly, the B&K microphone had its own Sound Calibrator Type 4231 shown in Fig. 4.21. The microphone with its flat tip protector layer would be placed into the calibrator. The 2270 Handheld Analyzer would operate the calibration program and compare the result with the previous calibration.

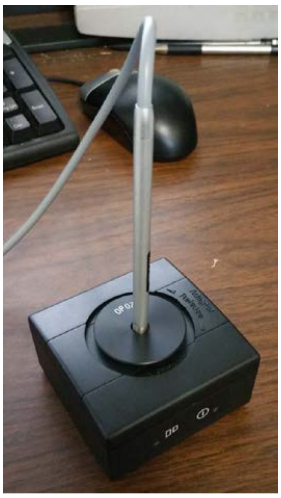

Figure 4.21 Bruel and Kjaer Microphone Sound Calibrator Type 4231

Baylor Experimental Procedure: Radial and Axial Traverse, RPM sweep and Frequency Spectrum

RPM Sweep

The RPM sweeps conducted at the BRIC Low-Speed Subsonic Wind Tunnel followed the same guidelines as outlined in the USAFA procedure with exception of accomplishing both static and dynamic test cases. The RPM sweeps were completed in increments of about 300 RPM from a range of 2000-6000 RPM. If the design thrust was met earlier than 6000 RPM, the test would conclude after one or two data points beyond 6,000 RPM. If the on-design thrust was not met within this range, the RPM sweep would continue until the Torque Cell was approaching its over-ranged limit of 1.77 in-lb_f. The sweep procedure was completed with the downstream microphone pointing into the flow at 1 inch aft of the trailing edge of the propeller and at a r/R location of 0.75. This process would remain essentially the same for a dynamic test.

For a dynamic test, the background SPL reading would be taken with all systems off. The tunnel would then be turned on and brought to a constant speed of 44 ft/s. The speed

of the tunnel was controlled through a NI-cDAQ 9178 chassis containing a NI 9263 analog output channel. The wind tunnel speed was set using the Propeller Testing LabVIEW VI real-time digital display which showed the speed in ft/s. Another acoustic measurement would be made with the tunnel operating and the propeller at zero throttle to measure the noise with the propeller at idle or windmill conditions. Once the measurement was recorded, the RPM sweep procedure would continue as normal following the guidelines previously mentioned.

Radial and Axial Traverse

For the propeller acoustic radial traverse measurements, a microphone traverse procedure was used to define the peak sound pressure levels of the propeller. The traverses located the r/R location for a peak dBA of a single propeller. The microphone with the bullet tip nose cone was placed 1 inch aft of the trailing edge pointing into the flow at an initial starting r/R location of 0.375 above the propeller hub. The propeller was then brought to a constant RPM at which the on-design thrust was achieved. For the airfoil study the on-design thrust was 1.5 lb_f while the lift distribution study design point was at 1.0 lb_f. The lift distribution study changed to a measured thrust of 0.5 lb_f due to torque transducer limitations. The microphone was then moved radially outward in 0.1-inch increments from a range of 0.375-1.1 r/R. The controller positions would be set using the Velmex software COSMOS and its 'relative move' menu. Once the measurement was complete, the microphone was moved to the next downstream location and the process repeated if needed. This procedure was accomplished at microphone locations of 1, 3, 6, and 9 inches aft of the propeller for the airfoil study only. These studies will be discussed in greater detail in Chapter Five. When all testing had been finished, the wind tunnel was shut down,

the power supply turned off, the Futaba controller turned off, and the propeller was changed to the next test propeller. The whole radial traverse process then was repeated.

An axial traverse was performed to investigate the noise outside the propeller stream tube parallel to the freestream velocity. The axial traverse testing procedure followed very similar guidelines as the radial traverse. The microphone was directed perpendicular to the flow, with a flat tip covering, and it was placed 1 inch above the propeller plane of rotation. The axial traverse was moved on a plane perpendicular to the propeller plane of rotation and from a range of 2 inches in front of the leading edge of the propeller to 4 inches aft of the leading edge for a total of 6 inches. The axial traverse was completed in increments of 0.2 inches at the on-design RPM and thrust. The axial traverses were all completed under dynamic conditions and only for the lift distribution study. The procedure began with shutting all systems off and recording background sound measurement. The tunnel was brought to 44 ft/s and another sound measurement recorded with the propeller not running. The propeller was then brought to on-design conditions. Once on-design conditions were achieved, the sound measurements were taken at the test locations. When testing was completed, the wind tunnel was shut down, the power supply turned off, and the Futaba controller turned off as well. The propeller was changed to the next test propeller and the axial traverse process repeated.

Frequency Spectrum

Gathering the frequency spectrum required the propeller to operate at the on-design condition. At the on-design condition, a 10-15 second audio recording was made by the handheld analyzer. The audio recording was then processed through the B&K software to perform a Laplace transform resulting in display of the power spectral density.

Uncertainty Analysis

The uncertainties of all the calculated results described in the above equations were determined using the root-sum-square uncertainty method from Kline and McClintock [47].

$$\eta = \frac{V*T}{RPM*Q} \tag{4.1}$$

$$U_{SYS,X} = Manufacturer\ Specified \tag{4.2}$$

$$U_{RAND,X} = \frac{t*S_x}{\sqrt{N}} \tag{4.3}$$

$$U_\eta = \left[(\frac{\delta\eta}{\delta V}U_V)^2 + (\frac{\delta\eta}{\delta T}U_T)^2 + (\frac{\delta\eta}{\delta \mathrm{RPM}}U_{RPM})^2 + (\frac{\delta\eta}{\delta Q}U_Q)^2\right]^{\frac{1}{2}} \tag{4.4}$$

The propeller efficiency uncertainty was determined to be 0.3%. The high sampling rate was able to reduce the random uncertainty values significantly. The main contributions to uncertainty where the systematic uncertainty values that either came from the manufacturer or were half of the least count placement.

Table 4.1 Uncertainty Analysis Summary

Measurement Variables	**Uncertainty**
Density (kg/m^3)	±0.003
Velocity (ft/s)	±0.153
SPL (dBA)	±0.1
Thrust (lbf)	±0.001
Torque (in*lbf)	±0.002
RPM	±0.064
Efficiency (%)	±0.3

CHAPTER FIVE

Experimental Results

This chapter will present the experimental results gathered from the investigations conducted at the USAFA and Baylor laboratories.

USAFA Testing Facility Results

This section presents the results of the experiments conducted at the USAFA with the anechoic chamber and North Low-Speed Wind Tunnel test facilities. The objective of the anechoic chamber testing was to investigate noise generation of stock and modified DJI Phantom 2 propellers, and to define the near and far field noise signatures. The objective of the experiments in USAFA North Low-Speed Wind Tunnel was to investigate noise and RPM reduction with five bladed propellers designed to disrupt the tip vortex and reduce noise generation. DJI Phantom2 and Gartt motors were compared to evaluate sUAS motor power consumption.

Anechoic Chamber

The testing in the anechoic chamber compared the aeroacoustics in the near and far field of the DJI Phantom 2 stock propeller to a stock propeller that was modified. The modified stock propeller had a notch in the Trailing Edge (TE) of the two blades. The notch was applied at 0.95 r/R with a Double Slot width and a Double Depth (DSDD) configuration. This propeller modification, recognized as the TE notch propeller, can be seen in Fig. 5.1. Previously, the TE notch design was compared to seven other tip

treatments that reduced blade tip vortices while minimizing the increases in power consumption [48] for the TE DSDD modification. For this modification, Van Treuren et al. measured a peak SPL reduction of 7.2dBA compared to the stock propeller for a 3.96% increase in power consumption. These propeller comparisons were taken in the near field at 1 inch behind the trailing edge of the propeller and were traversed radially from 1.5 inches from the centerline of the hub to the tip of the propeller. Additionally, these measurements were gathered at a thrust of 0.7 lb_f.

Since the TE notch propeller performed well in the near field, it was necessary to investigate how well it would compare to the DJI Stock propeller in the far field. Additionally, it was desired to investigate the behavior of the TE notch in a hexacopter configuration. The anechoic chamber provided an acoustic environment that would eliminate significant outside sources of noises at reasonably long distances away from the test stands.

Figure 5.1 TE notch blade [48]

Previous testing in the anechoic chamber verified axisymmetric noise characteristics for 360 degrees around the propeller test stand. This allowed the measurements to be limited between 0 and 180 degrees, where 0 degrees was directly upstream of the propeller plane and 180 degrees was directly downstream of the propeller. Measurements taken 1 foot away from the hub and with azimuthal angles of 0, 30, 60, 90, 120, 150, and 180

degrees are displayed in Fig 5.2. As seen in Fig. 5.2, the overall SPL trend displays little to no deviation between the two propellers at this distance. At 0 degrees the TE notch value is slightly higher than the Stock, both at about 80 dBA. At 90 degrees the SPL was approximately 72.5 dBA with the TE notch being slightly higher although there was an overall decrease in SPL from the 0-degrees measurements. Directly behind the propeller plane at 180 degrees, the TE notch was slightly higher than the Stock propeller at 92.5 dBA. The SPL values aft of the propeller at 180 degrees are the highest SPLs due to the contributions of the wake and other pressure perturbations behind the propeller.

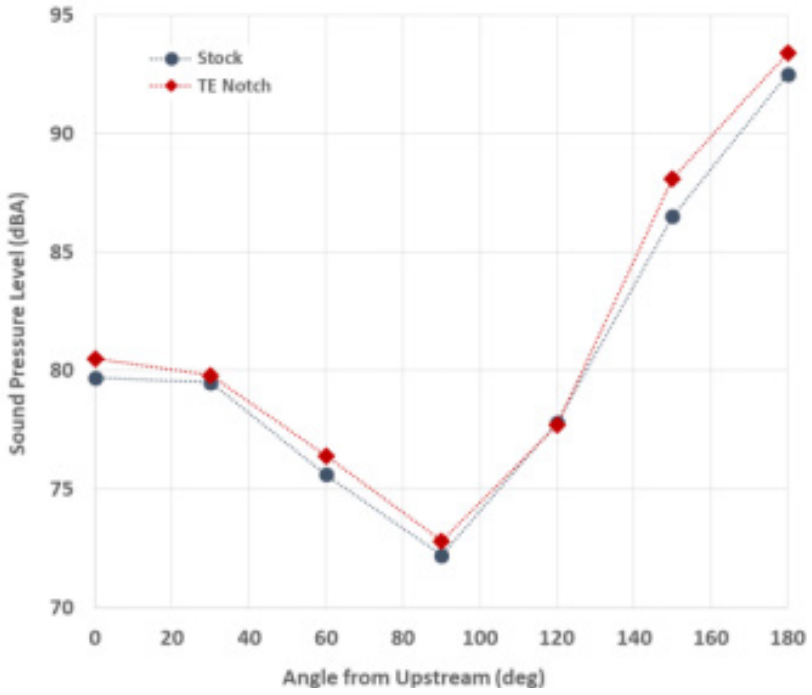

Figure 5.2 SPL azimuthal angles for Stock vs. TE notch at 1 foot

Following the SPL azimuthal angle measurements, frequency spectrums were taken of both propellers 1 foot away from the hub. Although there were minimal differences seen from the 1-foot azimuthal locations, the frequency spectrums showed differences in the lower frequencies of the power spectral density displayed in Fig. 5.3.

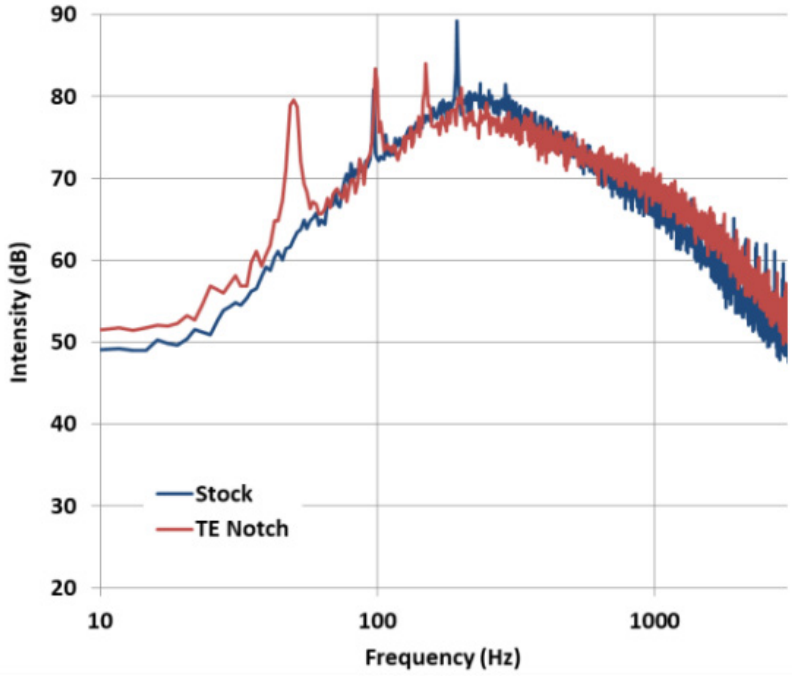

Figure 5.3 Stock and TE notch Power Spectral Density vs. Frequency (Hz) Located 1 Foot and an Azimuthal Angle 180 Degrees

At approximately 50 Hz the TE notch spectrum has a dramatic spike that this is not seen in the Stock spectrum. Meanwhile the Stock propeller had the highest overall peak value at 10 dBA higher than the TE notch spectrum. Frequency spectrums were also measured at distances of 5 and 9 feet at 180 degrees aft of the propeller hub. The 5-and 9-foot spectrums did not display any distinguishable differences between the Stock and TE notch spectral densities.

Continuing, measurements were also made comparing the SPL for the Stock and TE notch azimuthal angles while varying downstream distance as well. These results, shown in Fig. 5.4, illustrate no observable difference between the Stock and TE notch propellers for both the azimuth and distance. As a result, the sound decay testing with the single propeller test stand only used the Stock propeller.

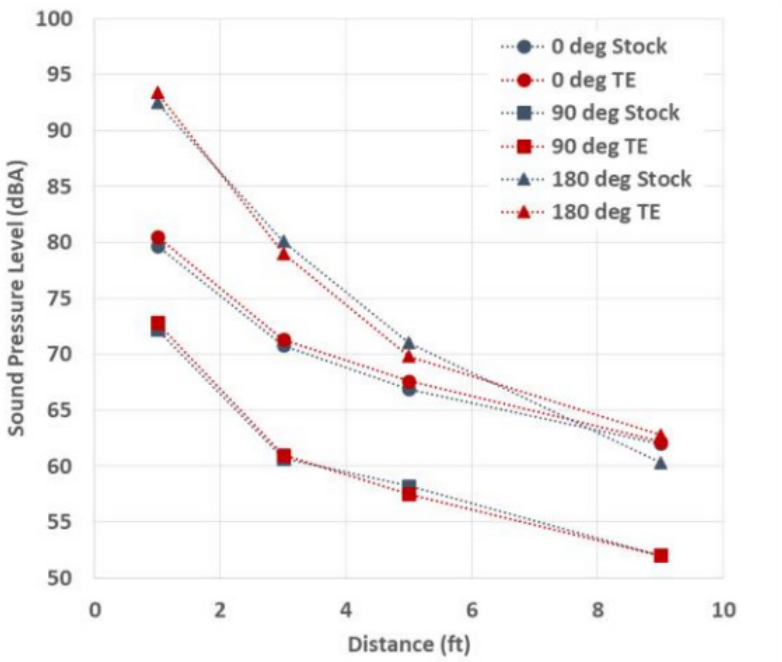

Figure 5.4 Stock and TE notch SPL (dBA) vs. Distance (ft)

With the single propeller test stand, a series of sound decay tests were accomplished at the 0- and 180-degrees azimuthal angles while also varying the distance. The B&K microphone was moved to distances of 1, 2, 4, 6, 8, 10, 11, 12, 18, 20, 22, and 24 feet. Figure 5.5 displays the 0-degree sound decay measurements with a theoretical sound decay applied to the 1 foot and 4-foot measurement. The stock value represents the measured SPL produced from the propeller. The 'Std Decay' refers to the theoretical sound decay as mentioned in Chapter Three. When the theoretical sound decay applied to 1 foot it can be seen that the decay rate does not follow the measured value. However, Fig. 5.5 shows that the theoretical decay rate does not occur until the 4-foot distance.

Decay trends are displayed shown behind the propeller test stand at 180 degrees in Fig. 5.6. However, the theoretical sound decay did not match the far field as well, and the SPL measurement magnitude overall, was higher than the 0-degree measurement by

approximately 10 dBA for each distance until about 10 feet. Moreover, the theoretical sound decay did not coincide with the experimental measurement until 18 feet for the 180-degree data. Contrasting with the sound decay trends shown in Fig. 5.5, the 180-degree orientation would suggest that the flow behind the propeller wake and turbulence would provide noise differences as well.

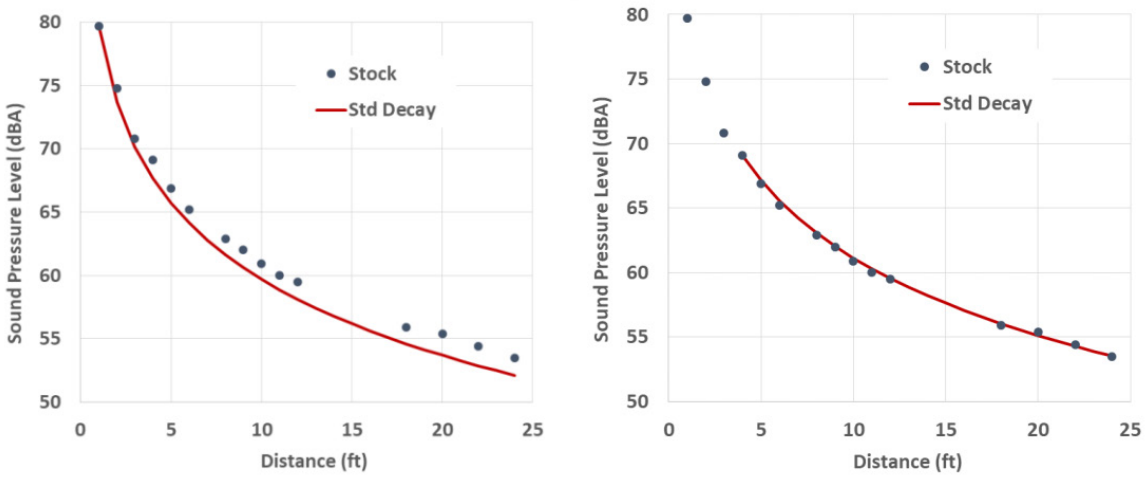

Figure 5.5 Stock and TE notch 0 Degree Sound Decay SPL (dBA) vs. Distance (ft) for 1-foot and 4-foot Theoretical Decay

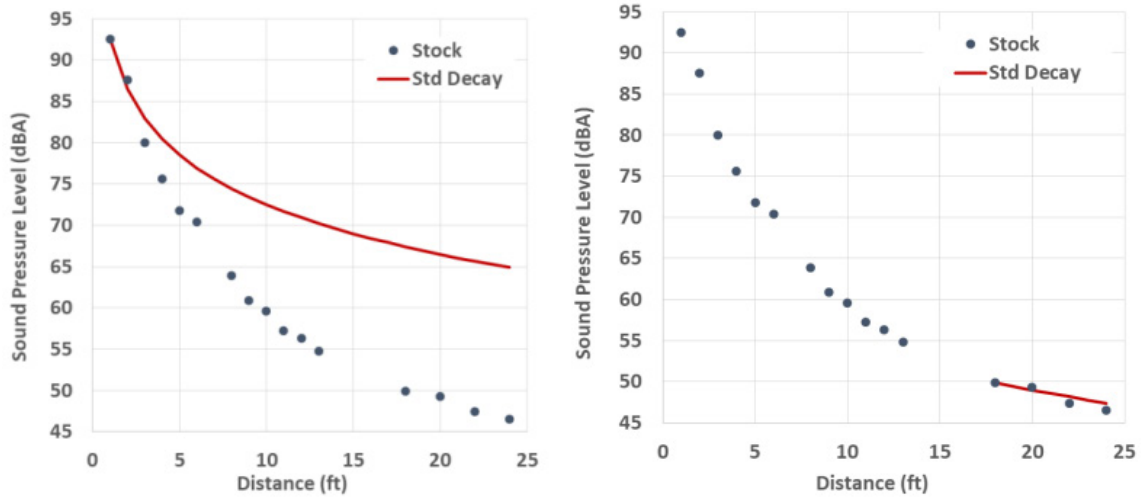

Figure 5.6 Stock and TE notch 180 Degree Sound Decay SPL (dBA) vs. Distance (ft) for1-foot and 18-foot Theoretical Decay

A frequency spectrum was measured at the 24-foot distance and compared to the 1-foot spectrum. The results are shown in Fig. 5.7. For the 180-degree azimuth orientation, the frequency spectrums showed clear deviations in magnitude and spike behavior dominating the upper end of the frequencies. The low frequencies are of importance as the low frequencies are similar to common frequencies the human ear hears. The magnitude of the frequencies at 24 feet were substantially lower in magnitude, especially at lower frequencies below 100 Hz.

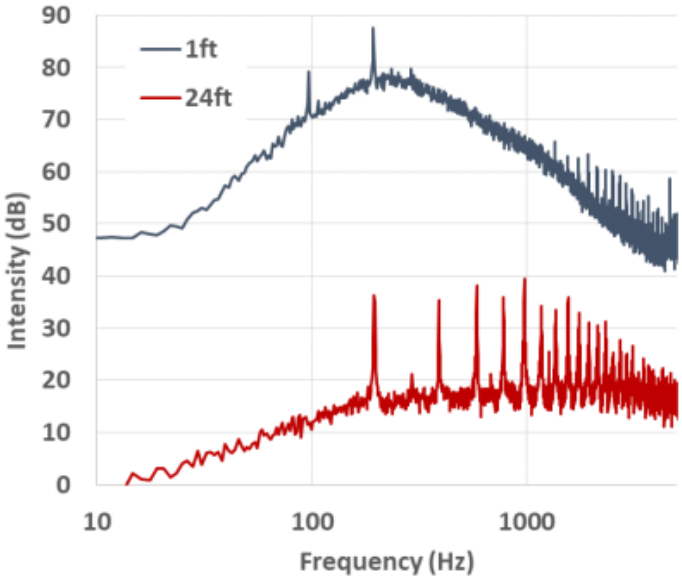

Figure 5.7 Stock Propeller Spectrum Comparison at 1 and 24 feet from 180 Degrees

Lastly, a series of radial microphone traverses were conducted in the near field within the USAFA North Low-Speed Wind Tunnel. Since there was no observable difference between the Stock and TE notch propellers at distances of 1-foot or greater, radial traverses were used to further investigate the near field phenomena, closer than 1 foot. These results, illustrated by Fig. 5.8, did show distinguishable differences when comparing the two propellers against SPL at the same r/R location. These results validate what was previously

determined by Van Treuren et al. from the 1-inch radial traverse, which was a large difference of approximately 8 dBA between the SPL peak of the Stock and TE notch propellers [48]. However, the distances further aft of 1-inch confirm what was determined in the anechoic chamber, which led to no observable difference with an increase in distance at 1 foot.

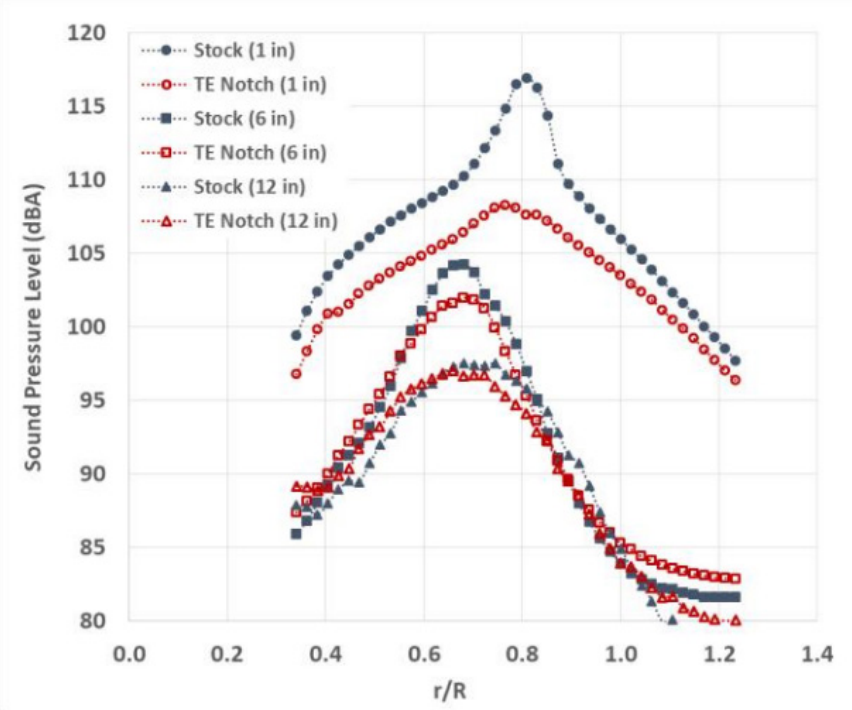

Figure 5.8 Radial Microphone Traverse of Stock and TE notch SPL vs. r/R at 1, 6, and 12 inches Downstream of the Propeller

Figure 5.9 further supports a similar trend for the Hexacopter study, which measured the sound generated at a height of 5 feet to the center of the device. Azimuthal orientations of 0, 90, and 180 degrees showed there is no observable difference between the two different propellers although, overall, the magnitude of the SPL had increased compared to the stock propeller test data. The lack of SPL differences between the TE notch and Stock propellers further illustrated the data with the single propeller test stand.

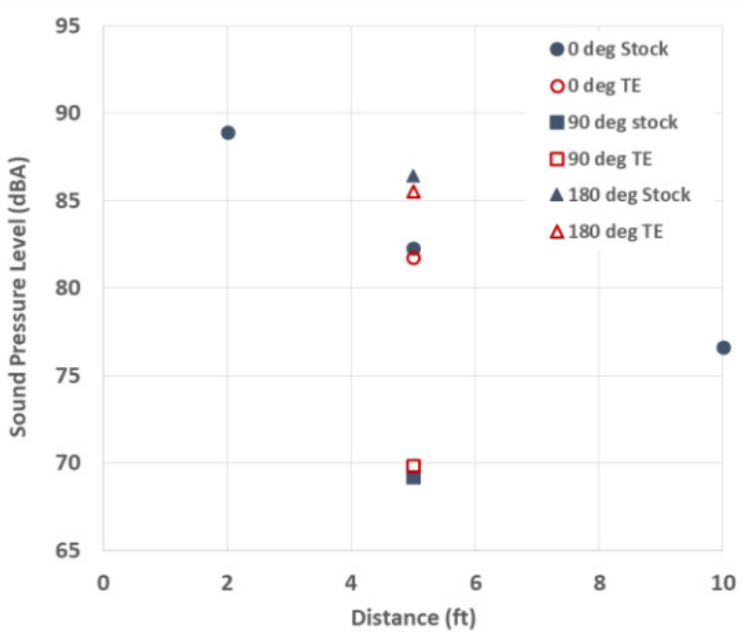

Figure 5.9 Hexacopter Stock and TE notch SPL vs. Distance (ft) for Azimuthal angles of 0, 90, and 180 degrees

USAFA North Low-Speed Wind Tunnel Studies

The USAFA North Low-Speed Wind Tunnel studies investigated the aeroacoustics and motor electrical efficiency of a two bladed DJI Phantom 2 Stock and five bladed custom propeller designs. The custom propellers were designed with the intent to reduce the strength of the tip vortex at a thrust design point of 0.7 lb_f. The custom five bladed propellers were also all designed with the GM15 airfoil and tested under static conditions. Static conditions with no incoming velocity would best simulate static hover conditions of a sUAS Quadcopter. Furthermore, the decision was made to test five bladed propellers to reduce the RPM under the premise that this would reduce the generated noise and the strength of the tip vortex. Additionally, the electrical power consumption of the propellers was also an important measurement. Figure 5.10 displays the five bladed propellers tested in this study.

A) B) C)

Figure 5.10 Five Bladed Custom Propellers Hoop5 (A), Oval5 (B), and the Square 5 (C)

The first set of tests conducted was an RPM sweep to determine the RPM point at which 0.7 lb_f thrust could be achieved. Figure 5.11 displays the RPM as a function of thrust. As the RPM increases, it is obvious that the SPL increases as well. The Stock propeller had the highest RPM of approximately 6000 RPM at the design thrust, followed by the Hoop5 and Oval5 at approximately 4176 RPM, and the Square5 had the lowest at 3340 RPM.

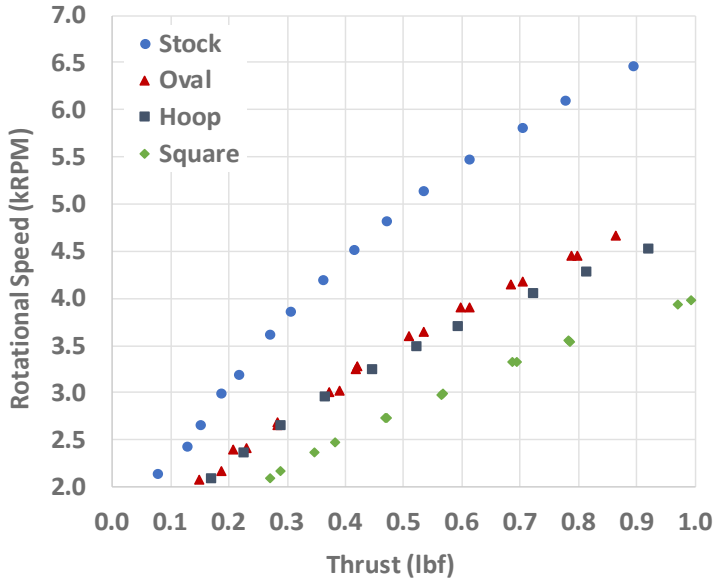

Figure 5.11 Stock and Five Bladed Propellers RPM vs Thrust (lb_f)

Given the custom propellers' increase in surface area, number of blades, and the weights being heavier than the Stock propeller, the RPM results are not surprising. Table 5.1 displays the propeller weights.

Table 5.1 Weight of Propellers

Propeller	Weight (g)
Hoop5	97
Square5	57
Oval5	47
Stock	13

These results showed that surface area changes the disk loading. The smaller disk loading and surface area, seen with the Stock Propeller, would require a higher RPM. The opposite would be seen with the largest surface area and disk loading with the Square5 propeller. However, the Hoop5 propeller had surprising results as its disk loading would be similar to the Square5, the difference being the ring connecting Hoop tips. This provided intuition into the streamtube effects of the Hoop in that it greatly reduced the tip vortex strength.

Figure 5.12 shows the Mechanical Power of the Stock and Five Bladed propellers as functions of thrust. Mechanical Power is defined as a function of torque and RPM, as depicted in Eq. 5.1, where Q is the torque and n is the propeller revolutions per second [30]. Electrical power was calculated as a function of voltage and current, and electrical efficiency was defined as the ratio of mechanical power to electrical power.

$$Mechanical\ Power = 2\pi nQ \tag{5.1}$$

$$Electrical\ Power = Voltage * Current \tag{5.2}$$

$$Electrical\ Efficiency = \frac{Mechanical\ Power}{Electrcial\ Power} \tag{5.3}$$

At 0.7 lb_f, the Hoop5 had the highest mechanical power of 52.3W while the rest of the propellers were approximately 33.1W with minimal differences between the Oval5 and Square5. It was determined that the large weight of the Hoop5 and added drag contributed to high torque loading which then increased the mechanical power.

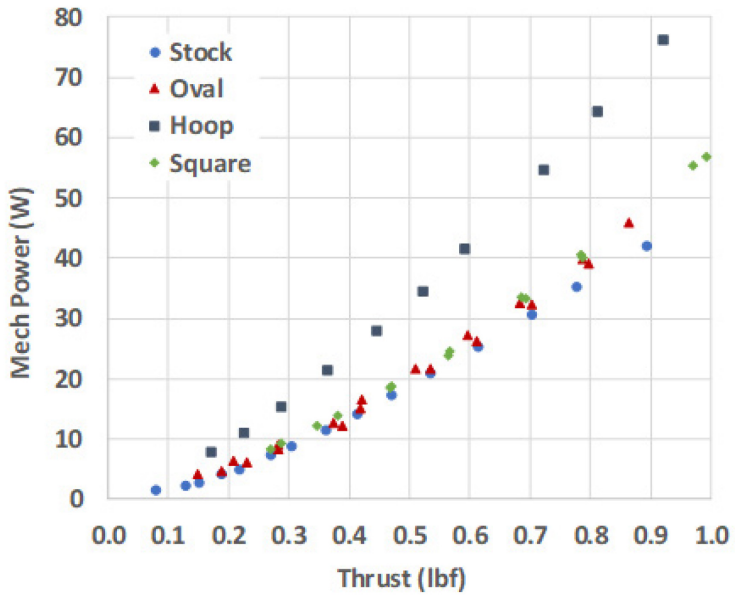

Figure 5.12 Stock and Five Bladed Propellers Mechanical Power (W) vs. Thrust (lb_f)

The next series of tests were radial traverses to characterize the near field acoustic performance of the propellers. The microphone was traversed along the span of the propeller blade where r/R was a non-dimensional parameter describing the radius of the propeller. A r/R = 0.0 would be located at the hub, and a r/R = 1.0 would be located at the tip of the blade. The microphone was traversed from a range of r/R = 0.30 – 1.30 at 0.1 inch increments. Figure 5.13 displays the results of a radial traverse conducted 1 inch aft of the trailing edge of the propellers.

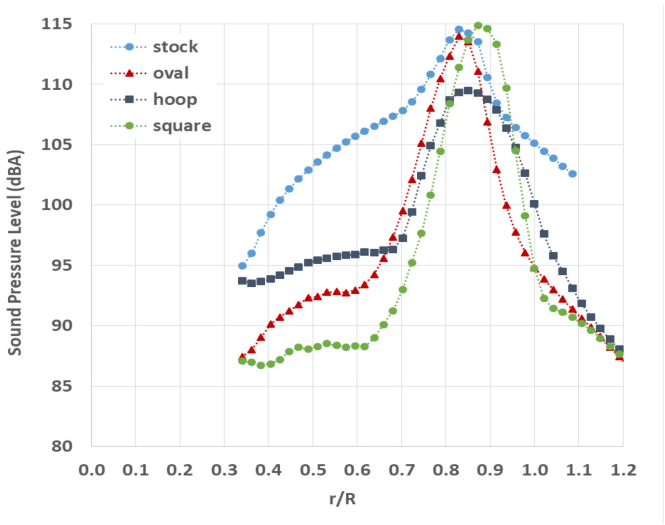

Figure 5.13 Stock and Five Bladed 1-inch Radial Traverse SPL vs. r/R

These results display an approximate difference of 5 dBA at the peak SPL between the Hoop5 propeller and the other propellers tested. The SPL distributions showed the Stock maintaining high SPL values until its peak, the Oval5 and Square5 showed similar orders of magnitude in peak SPL as the Stock despite reductions in over 2000 RPM. The Hoop5 distribution maintained the lowest SPL distribution in addition to lowest the peak SPL. The reduction in SPL would indicate that the Hoop5 design was effective in eliminating the tip vortex strength. These trends would continue further downstream of the propellers with radial traverses of 6, 9, and 12 inches.

Figure 5.14 displays the 12-inch Radial Traverse SPL vs. r/R. The peak SPL magnitudes decreased downstream, but the difference in SPL peaks was still evident with the Hoop5 propeller being the lowest. By this point, all of the propellers have reduced their peak SPL to be below the Stock propeller. The peak locations have also all trended further towards the tip of the blade. Overall the SPL peaks of the 12-inch traverse showed SPL dissipations in magnitude with a decrease in SPL surrounding the peak distribution.

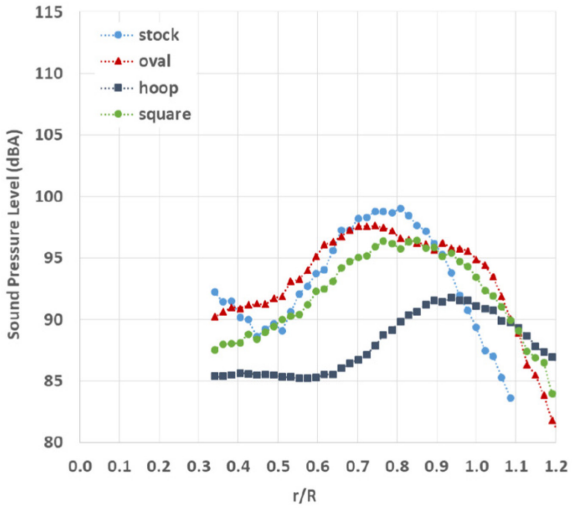

Figure 5.14 Stock and Five Bladed 12-inch Radial Traverse SPL vs. r/R

Figure 5.15 shows the Five Bladed propellers peak SPL reduction compared to the Stock propeller. Clearly the Hoop5 provided the lowest SPL generation compared to the Stock propeller of all the blades tested with reductions of 5 – 9 dBA. The Square5 propeller performed better from 6-12 inches and eventually reached a 3 dBA reduction. The Oval5 propeller had the lowest difference in SPL, but it was consistently lower at 1–2 dBA. These reductions in SPL were attributed to the reduction of the tip vortex strength.

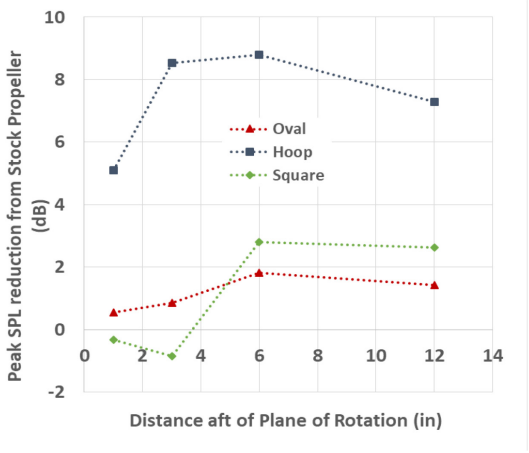

Figure 5.15 Five Bladed Propeller Peak SPL Reduction from Stock Propeller vs. Distance Aft of Plane of Rotation (in)

Figure 5.16 provides smoke visualization showing that all of the Five Bladed custom designed propellers reduced the strength of the tip vortex. The results indicate that the vortex reduction was largely related to the surface area, disk loading, and reduction in RPM.

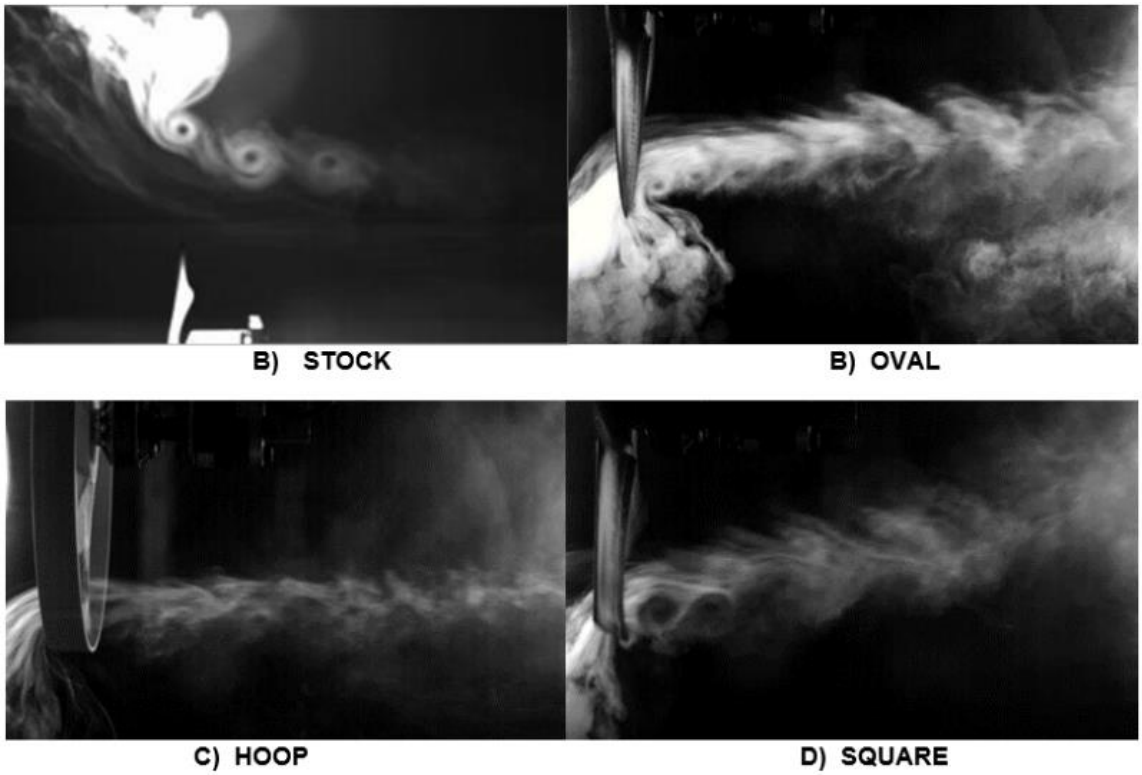

Figure 5.16 Smoke Flow Visualization for all Propellers

Figure 5.17 displays the frequency spectrums taken 1 inch aft of the plane of rotation at the peak SPL location for each respective propeller. The frequency spectrums were also measured at the on-design thrust point of 0.7 lb_f. The on-design thrust was established through the RPM sweeps discussed previously. When comparing the different spectrums, there were no strong similarities to the magnitudes and spike locations for each frequency spectrum except for the Hoop5 propeller. The Hoop5 data displayed spike values lowest in

magnitude than the other propellers. Similar behavior was seen with the frequency spectrums taken 6 inches aft of the propeller plane of rotation.

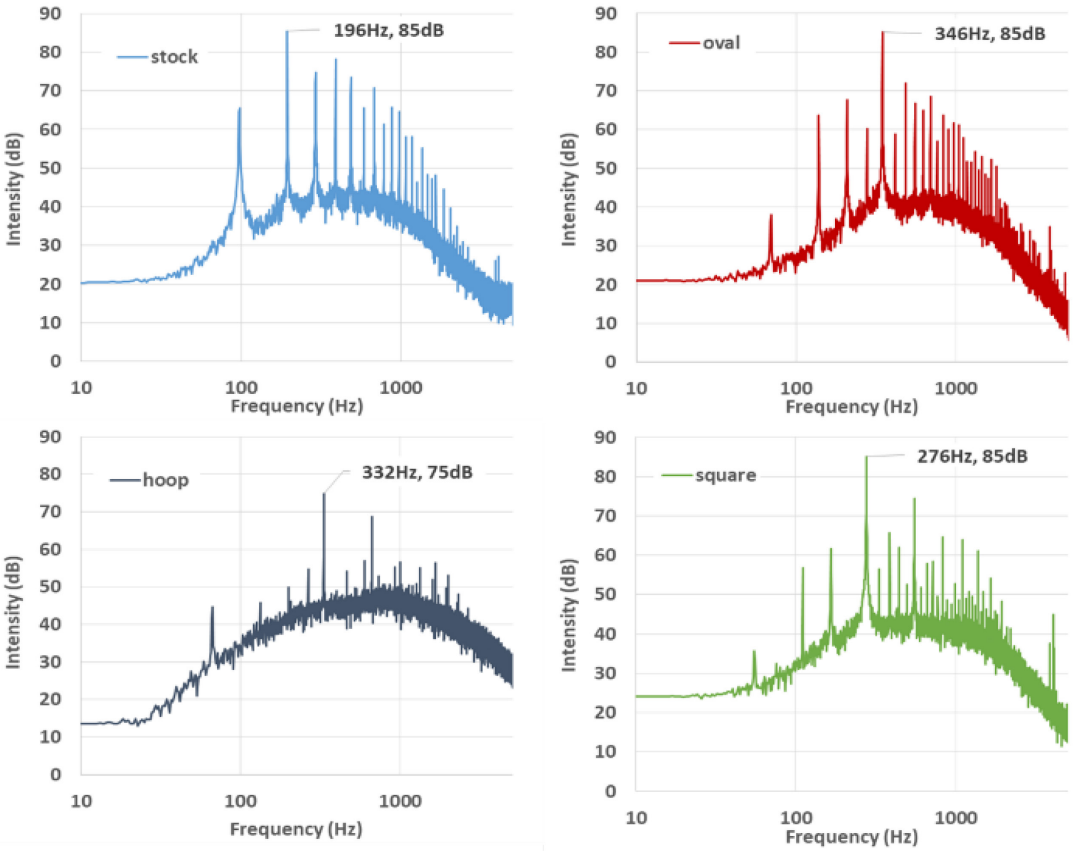

Figure 5.17 Propeller Frequency Spectrums at 1 inch Aft of the Propeller Plane of Rotation

The last set of results for the USAFA North Low-Speed Wind Tunnel tested the power consumption of the propellers in relation to electrical efficiency. The first study involved the DJI Phantom 2 Stock propeller and its Stock motor. The objective was to determine how the input voltage would affect the motor performance. Figure 5.18 displays the electrical efficiency comparison of the DJI Stock motor at input voltages of 8.32, 11.5, 14.93, and 17.5 VDC.

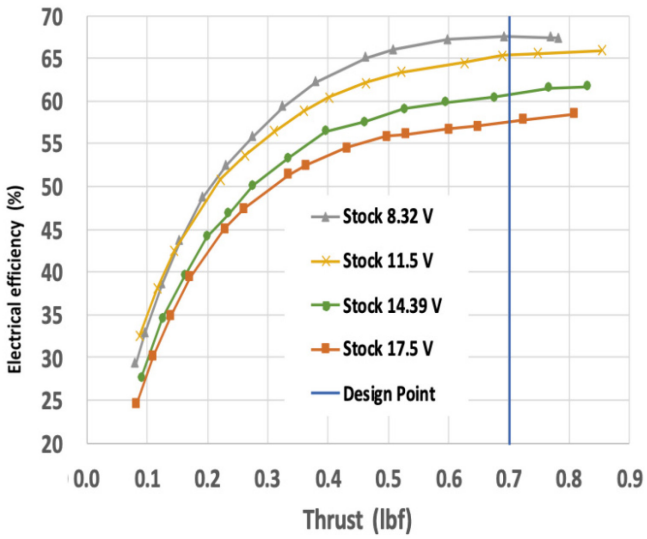

Figure 5.18 DJI 960 Kv Electrical Efficiency vs. Thrust (lb_f) with Varying Input Voltages

An RPM sweep was accomplished for each voltage setting to characterize the electrical efficiency as a function of thrust. The data illustrates the electrical efficiency dependence on the input voltage. Lowering the input voltage caused a higher electrical efficiency. Overall, there was a 17.4% improvement in electrical efficiency at the on-design thrust for operating at the lower input voltage setting of 8.32 VDC compared with the highest voltage. This an important finding as it illustrates how operating at the most electrically efficient input voltage could increase flight time for a UAS.

This voltage trend was also consistent with the Gartt motors but not as pronounced. Figures 5.19 and 5.20 display the Gartt 370 and 580 Kv motors, respectively, plotted with electrical efficiency as a function of thrust. Although the Gartt motors were not nearly as sensitive to input voltage settings as the 960 Kv Stock motor, it was still determined that the lower voltages improved the electrical efficiency. Figure 5.20 shows the Gartt 580 Kv electrical efficiency vs. thrust for several different input voltage settings from 11.8 VDC to 14.8 VDC. The Gartt 580 Kv motor experienced a 2.4% improvement at a lower voltage

setting of 11.8 VDC, and the Gartt 370 Kv motor experienced a 3.7% improvement while operating 18 VDC.

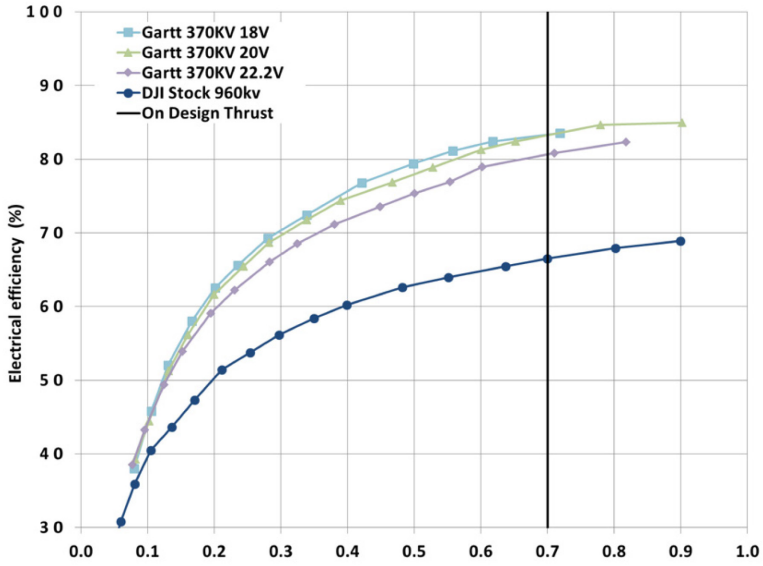

Figure 5.19 Gartt 370 Kv Electrical Efficiency vs. Thrust (lb_f) with Varying Input Voltages

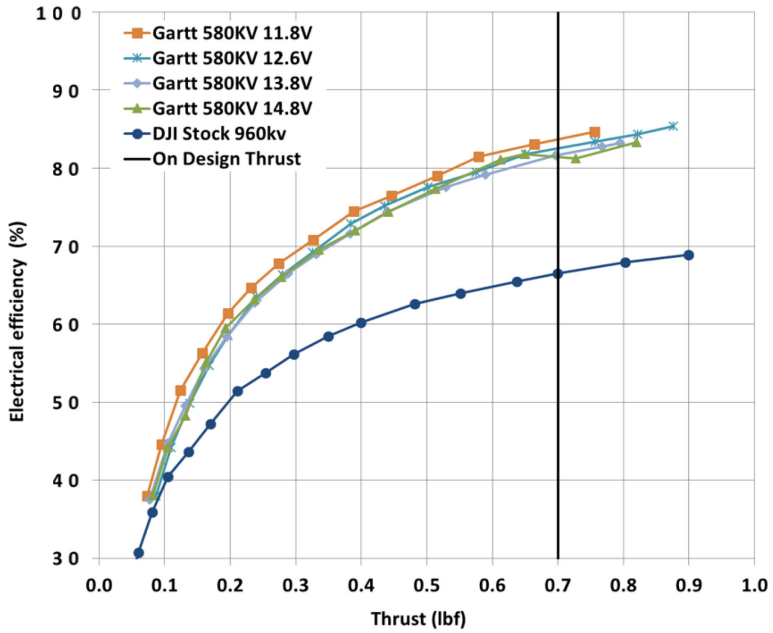

Figure 5.20 Gartt 580 Kv Electrical Efficiency vs. Thrust (lb_f) with Varying Input Voltages

Figure 5.21 displays the comparison between the 960 Kv Stock and Gartt 580 Kv motors using both the Stock and Hoop5 propellers. In this plot it is clearly evident that the Gartt 580 Kv motor was more electrically efficient than the 960 Kv Stock motor as seen with both propellers. Despite very different propeller characteristics between weight and disk loading, the Gartt 580 Kv motor experienced electrical efficiencies with improvements of 16.5% for the Hoop5 propeller and 31.3% for the Stock propeller. This testing illustrates that matching the propeller and motor will reduce power consumption and improve the performance of the UAS. This should be an optimization process contingent upon mission characteristics.

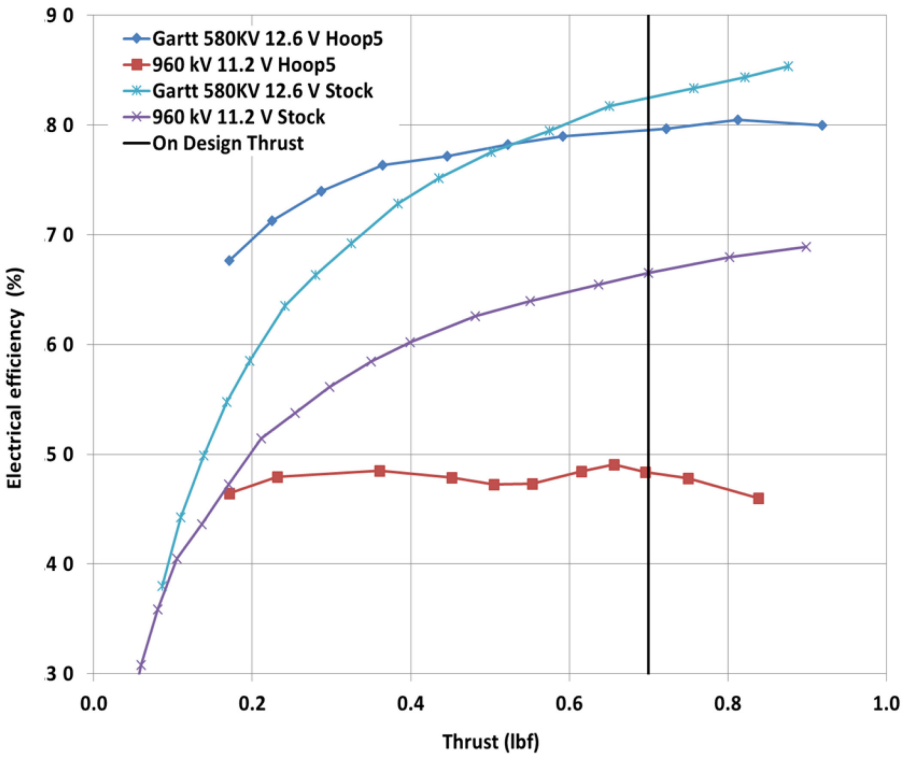

Figure 5.21 Comparison of 960 Kv Stock and Gartt 580 Kv with Stock and Hoop5 Propeller

Baylor Results

Two main studies were conducted on airfoil optimization and the effects of unloading the propeller blade tip by changing the lift distribution on the blades. The testing in this report was conducted under a typical design point for the Terminator UAS. The chosen design was a diameter constrained to 8 inches with an incoming velocity of approximately 44 ft/s. Additionally, the propellers were all limited to a 'constant chord' tip treatment. The propellers did not have a taper towards the outboard portion of the blade as was seen with the previous oval tip propellers. The effects of a tip vortex will be significant since there were no physical tip treatments applied. With a strong tip vortex and no taper, a consistent comparison can be made among experimental airfoils.

Airfoil Study

The airfoil investigation compared 5 airfoils. Airfoil performance was explored at a Reynolds number of 100,000. Since the propellers are designed with a constant chord for this study, the Reynolds number was expected to vary from the hub to the outer radius of the propeller as the relative velocity increases. The outer portion of the blade the near the tip is expected to see Reynolds numbers close to 100,000. Moreover, the airfoils in this study were chosen with the goal of having better aero-acoustic performance than the GM15 airfoil, frequently used in USAFA research. The GM15 has a low max thickness of 6.7% which results in a very thin trailing edge. This is not desirable for UAS applications. Such a thin airfoil cross section would be easily susceptible to breaking in both urban and military environments, making it a liability to use on UAS propellers. Figure 5.2 shows the GM15 and GOE358 airfoils where the differences in thickness and camber can be seen.

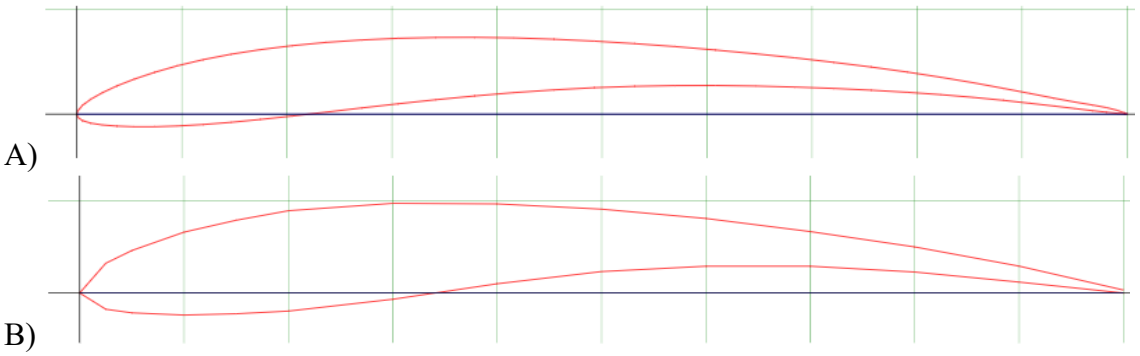

Figure 5.22 Airfoil Comparison of the GM15 (A) and the GOE358 (B) [49,50]

The airfoils chosen for this study all had high lift coefficients in addition to having broad L/D_{Max} curves. As mentioned earlier, this would help avoid stall yet operate with more aerodynamic efficiency. The GM15 thickness value was rather small and not feasible for a realistic UAS environment. Therefore, a last constraint of a max thickness of 9-10% was added for the airfoils in this study. It is important to note that the airfoils' aerodynamic characteristics were used in the propeller design program that resulted in a propeller optimized for a thrust of 1.5 lb_f and an RPM of 6000. The constraint of the on-design thrust and RPM resulted in the chord length of the propellers being different.

The airfoils selected for study were the AH 79-100 A, GM15, FX 63-120, GOE 358, and SA7026. These airfoils were selected for having sufficient thickness, shown in Table 5.2, to be used with additive manufacturing while providing adequate lift to drag characteristics. The additive manufacturing process required the airfoils to have sufficient thickness so the propeller would not fail under loading. A high maximum C_l/C_d value was required for the airfoils selected so the propeller could efficiently operate. However, if there was not a wide enough range of angle of attack where optimal C_l/C_d values occur the propeller could stall, and no further lift would be generated. Stalling occurred with the SG6043 propeller which resulted in its inability to reach the design thrust, and therefore

was discontinued from this report's experimental results and not reported in Table 5.2. Information about each propeller selected can be seen below in Table 5.2.

Table 5.2: Airfoil Characteristics at Re = 100,000 [48-53]

Airfoil	Max Thickness (%)	Max Camber (%)	Chord Line Distances (in)	L/D_{Max}	α Optimal Range (deg)
AH 79-100A	**10.0**	**3.6**	**1.56**	**62**	**5.0-7.0**
GM15	**6.7**	**4.8**	**1.40**	**67**	**3.5-6.0**
FX63-120	**12.0**	**5.2**	**1.22**	**65**	**5.5-7.5**
GOE 358	**10.9**	**5.6**	**1.12**	**59**	**4.5-9.0**
SA7026	**9.0**	**3.6**	**1.57**	**61**	**5.5-7.0**

The plots shown below in Figs. 5.23-5.27 are the computational data of XFOIL taken from AirfoilTools [48-53]. These plots were created for all the airfoils at a Reynolds number of 100,000. Furthermore, these plots were useful in comparing propellers C_l/C_d vs. α behavior. The AH79-100A plot shown in Fig. 5.23 displays a curve that was wider than the GM15 airfoil and it had a C_l max value just below the GM15 airfoil. The GM15 characteristics can be seen by Fig. 5.24 shown below.

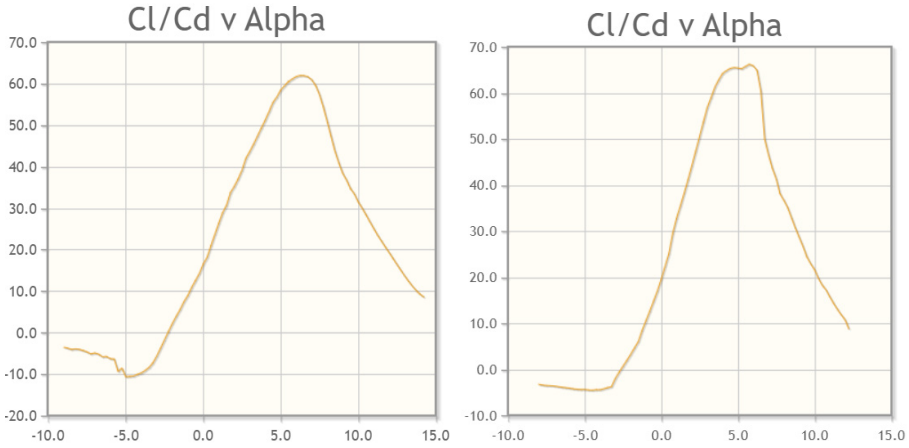

Figure 5.23 (left) and 5.24 (right): C_l/C_d vs. α at Re=100,000 for AH 79-100A (Left) and GM15, respectively [51, 49]

Additionally, Figures 5.25-5.26 are more AirfoilTools plots at a Reynolds number of 100,000. The GOE358 displayed in Figure 5.25 provided a C_l/C_d max value just below the GM15, but it also had a wide C_l/C_d vs. α curve that was especially predominant for high C_l values. This was important to note the distinction that this wide distribution provides a more robust design that can delay stall better than the other airfoils. Delaying the margin of stall on the airfoil would provide a wider range of on-design AOA for the airfoil to operate. The GM15 had a L/D_{Max} range for about 2.5 AOA while the GOE358 had a L/D_{Max} range for about 4.5 AOA. The FX 63120 displayed in Fig. 5.26 had a C_l max value very similar to the GM15, and it still had a wider C_l/C_d vs. α curve than the GM15 by a small margin. The SA7026 displayed in Fig. 5.27 provided C_l/C_d max that appears to the same as the GM15, but its distribution was much narrower than the GOE358 as well.

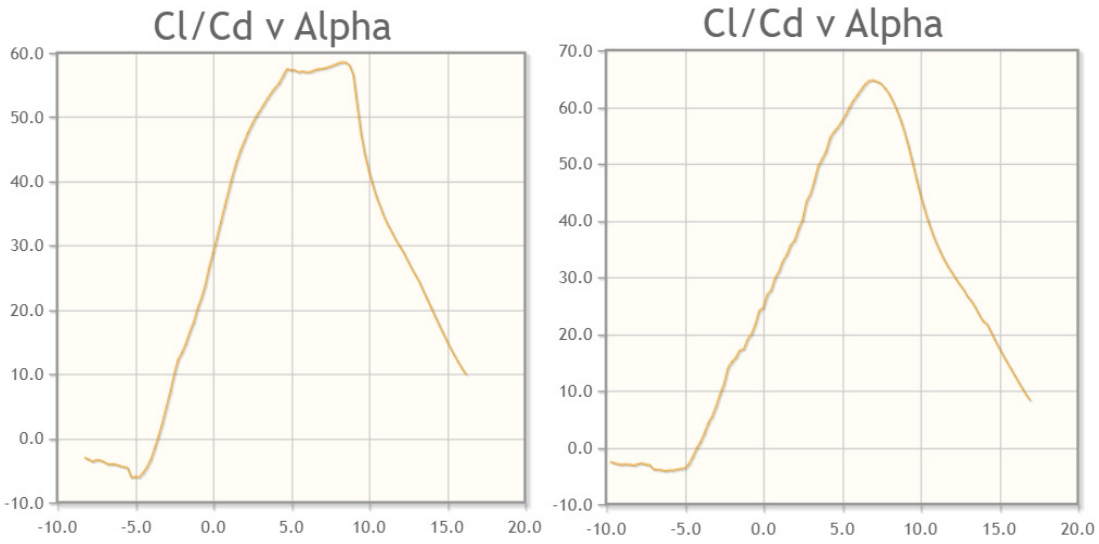

Figure 5.25 (left) and 5.26 (right): C_l/C_d vs. α at Re=100,000 for GOE358 (left) and FX63120 (right), respectively [49, 52]

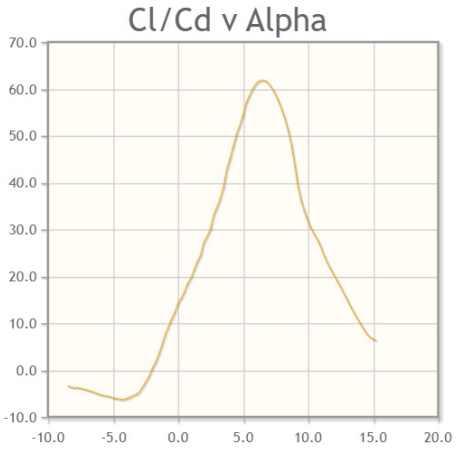

Figure 5.27: C_l/C_d vs. α at Re=100,000 for and SA7026 [53]

Figure 5.28 displays the chord changes due to the different airfoil characteristic data shown in Table 5.2. The largest chord lengths can be seen below with the AH79-100A and the SA7026. The smallest chord belongs to the GOE358. The GOE358 had the smallest chord because of its aerodynamic lift and drag characteristics were better than the other propellers. Because its chord length was the smallest, this shows that it did not need as much surface area as the other propellers with large chord lengths to achieve the 0.7 lb_f of thrust. All propellers were designed under the same conditions, therefore, the GOE358 did not need a larger surface area to produce the same amount of thrust.

Figure 5.28: Displayed left to right are the AH79-100A, FX63120, GM15, GOE358, and SA7026 propellers

The experimental results for the airfoil comparison have little to no difference in the acoustic measurements. Figure 5.29 shows the 9-inch radial traverse data for the airfoils that were considered. All the tested propellers have essentially similar SPLs with their peak nearly the same magnitude at the same r/R, occurring at the edge of the propeller. Table 5.3 shows the small SPL deviations at both 1 and 9 inches aft of the propeller. This makes sense due to the sharp discontinuity that a constant chord (square) tip treatment provides. Comparing the propellers purely based on the measurements, the SA7026 has the lowest peak noise measurement, but it is not that much lower than the other propellers.

Table 5.3 Airfoil Study Peak SPL at 1 and 9 inches

Propeller	Propeller Speed (RPM)	1" Peak SPL (dBA)	9" Peak SPL (dBA)
AH79-100a	**4899**	**127.64**	**121.82**
FX63120	**5142**	**127.06**	**122.41**
GM15	**4588**	**127.93**	**122.15**
GOE358	**5836**	**127.98**	**122.66**
SA7026	**4934**	**126.50**	**121.85**

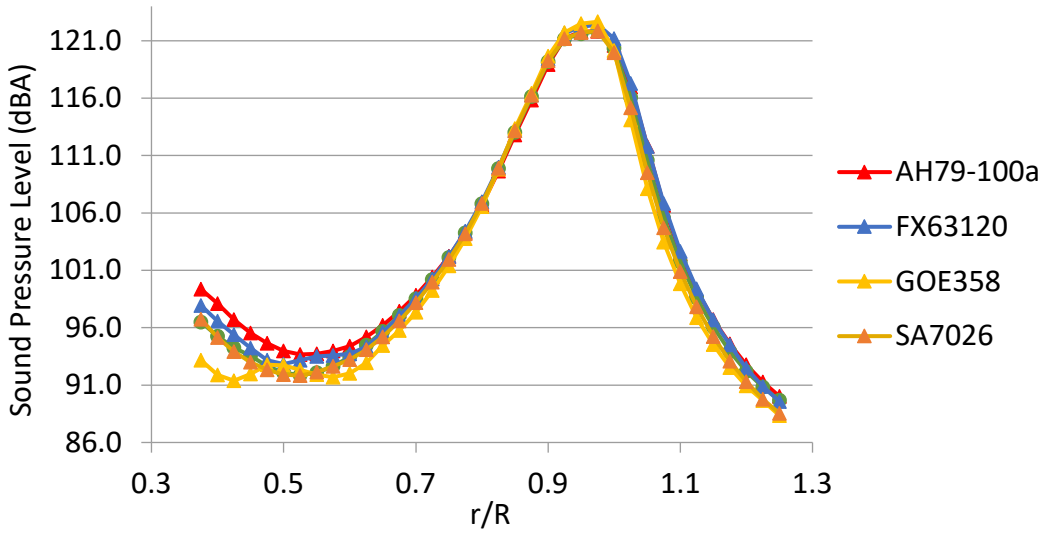

Figure 5.29 Typical Airfoil Study Radial Traverse (9-inches shown)

Lastly, Table 5.4 displayed the electrical efficiency for each of the propellers tested. The clear winner of this study was the GOE358 with a 67.80% electrical efficiency which used its higher aerodynamic performance to provide greater efficiencies. Furthermore, its thick profile favors an increased camber with a thicker trailing edge which also made this airfoil a good choice for this study.

Table 5.4: Comprehensive Performance Results

Propeller	Propeller Speed (RPM)	ELC Efficiency (%)
AH79-100a	**4899**	**31.71**
FX63120	**5142**	**61.00**
GOE358	**5836**	**67.80**
SA7026	**4934**	**55.99**

Lift Distribution Study

The objective of the lift distribution study was to test the effects of unloading the tip of the propeller to eliminate the tip vortex. This reduces the induced drag on the propeller resulting in a reduction in power consumption. The design point of this study was directed towards propeller improvements for the Raven sUAS while also maintaining the same constraints listed previously for the airfoil study. All custom designed propellers were made with the GOE358 airfoil. As previously mentioned, this airfoil had high aerodynamic performance that made it a durable airfoil to use in designing propellers.

Preliminary testing of brief RPM sweeps showed that the initial design point of 1.0 lb_f of thrust could not be obtained without over-ranging the torque transducer. Therefore, the propellers were all compared at a test point of 0.5 lb_f of thrust. Although this was not the theoretical design point, all testing of the propellers was completed under the same

conditions with the same testing procedures. It was thought that a new comparison point of 0.5 lb_f of thrust would be satisfactory to show desired trends.

Propeller Lift Distributions Described

Figure 5.30, shown above, displays the lift coefficient distributions that were used to design the propellers. To begin, the Baseline distribution illustrates the typical minimum induced loss design. This propeller was designed for max C_L/C_D AOA which results in a nearly constant C_L. The lift coefficient has a slight increase as it progressed to the edge of the blade. As can be seen with the remainder of the lift coefficient distributions, it is clear that C_L decreases to the tip. The tip has been unloaded with these designs. The Prandtl bell-shaped design had a lift coefficient distribution that experienced the most aggressive drop in its lift coefficient. The Prandtl Smooth design was made to develop a less aggressive unloading of the tip, particularly at an approximate r/R of 0.57-0.59. The last custom lift coefficient distribution was the 60_1 design. The 60_1 design created a similar starting r/R as the Prandtl bell-shaped distribution as its range was from 0.6-1.0 r/R. It used a polynomial curve fit to zero lift at the tip.

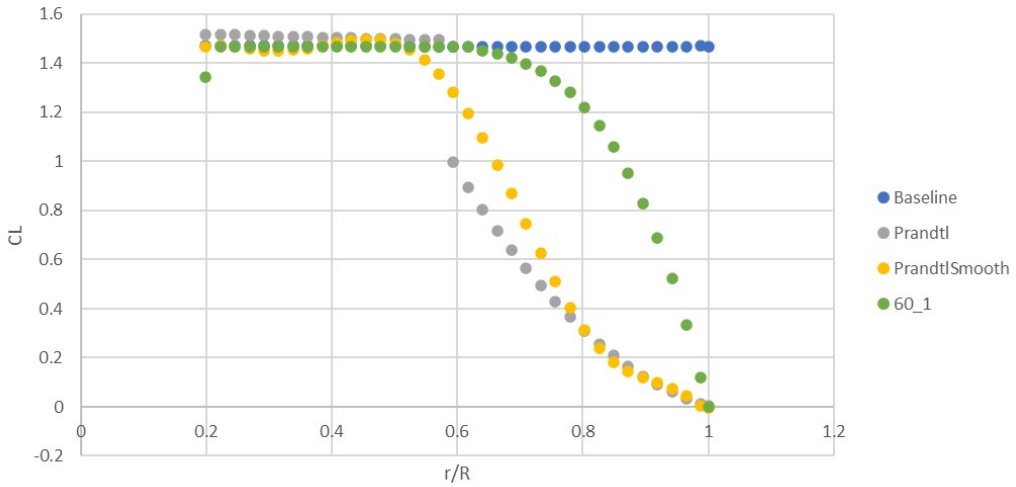

Figure 5.30 Lift Coefficient Distribution at 1.0 lb_f of Thrust

Propeller Physical Description

The propellers tested in this study are shown in Figure 5.31 from top to bottom and left to right, the propellers are organized: Prandtl Smooth, Prandtl Bell-Shaped, 60_1, and the Baseline propeller. The physical description of the propellers helps illustrate the unique designs. Notably, the Prandtl bell-Shaped and the Prandtl Smooth propellers' drastic unloading at r/R = 0.60 shows in the design with the abrupt twists that occurs at roughly half the radius of the two propellers. Especially with the Prandtl bell-Shaped design, the sharp drop in its lift coefficient can be seen at approximately an r/R between 0.57-0.59. The dramatic twists resulted from the zero-lift production at the tip. These blades were also made with a 'dovetail' design such that the individual blade would be inserted to a dovetail hub. This simplified the manufacturing process and provided better resolution for the smaller blade. The APC 8x6 propeller was added to this study to compare the aeroacoustics and power reduction against a widely used commercial propeller. It is also important to note there was a difference in weight where the APC 8x6 propeller was approximately 40% lighter than the weight of the minimum induced drag blades and the Baseline blades, without the dovetail hub and attachments for mounting.

The Prandtl Bell-Shaped, Prandtl Smooth, and the 60_1 all had similar characteristics at the outboard portion of the propeller blade. The propellers had twists that moved the AOA to a negative direction. The AOA for the Baseline propeller progresses to becoming more positive from the hub to the tip of the blade. This helps illustrate the propeller design compensating for the minimum induced drag design by attempting to force the vortex interaction towards the inboard portion of the blade instead of the outboard portion. The Baseline propeller had contrasting characteristics of vortices towards the edge of its blade.

This is largely because the Baseline propeller, designed for minimum induced loss, is trying to use the outer portion of the blade to develop most of the thrust on the propeller.

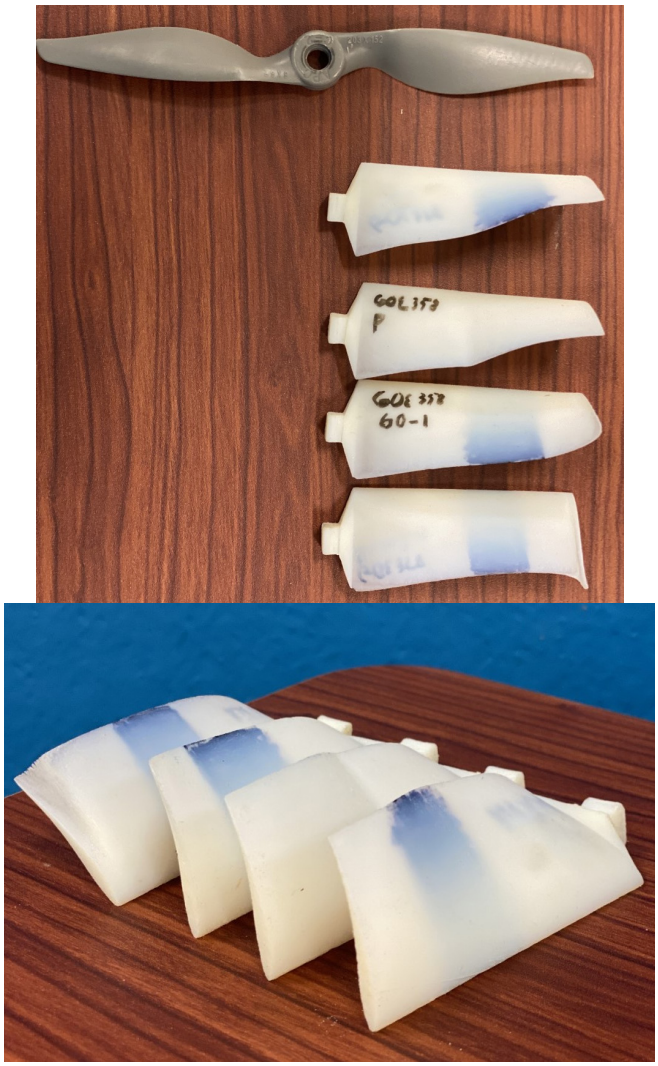

Figure 5.31 Lift Distribution Propellers

Lift Distribution Results

Propeller performance data was gathered by completing RPM sweeps with the freestream velocity at 44 ft/s. The RPM sweeps were used to analyze the power consumption of the propellers in terms of the torque, mechanical and electrical power.

Table 5.5 displays the results of the RPM sweep data comparing power consumption and electrical efficiency of the propellers.

Table 5.5 Lift Distribution Propeller RPM Sweep Power and Electrical Efficiency at 0.5 lb_f of Thrust

Propeller	RPM	**Torque** (in-lbf)	**ME PWR** (W)	**ELC PWR** (W)	**ELC Eff** (%)
Baseline	**3858**	**1.11**	**50.54**	**118.66**	**42.21**
Prandtl	**5271**	**0.78**	**48.76**	**79.92**	**60.75**
Prandtl-Smooth	**5522**	**0.82**	**53.45**	**88.14**	**60.80**
60_1	**4047**	**1.04**	**49.47**	**98.13**	**50.07**
8x6	7547	0.50	48.00	70.00	68.60

The Baseline propeller had the poorest performance in terms of torque, electrical power, and electrical efficiency, which was expected. It was also expected that the Baseline propeller would have the lowest RPM and relatively low mechanical power. This was attributed to the high lift distribution carrying through the tip of the blades. Having more lift produced at the tip of the blades means that the RPM would not need to operate as high to obtain the same lift or thrust. The 60_1 propeller was next after the Baseline propeller. This performance was not entirely expected since this propeller also unloads the tip of the blade. This shows that unloading the tip using a polynomial fit does not immediately reduce the torque moving to the tip, therefore, power consumption of the propeller stays higher. However, there was still an 8% improvement in electrical efficiency over the Baseline propeller as the 60_1 propeller was 50.07% electrically efficient.

The Prandtl and Prandtl Smooth propellers had the best performance in terms of their electrical efficiency of all the custom designed propellers. There was only a 0.05% difference in electrical efficiency between the two propellers with the Prandtl Smooth being higher at 60.80%. The Prandtl Smooth required an RPM of 5522 which was slightly

higher than the Prandtl's RPM at 5271. The Prandtl Smooth also had higher torque, mechanical power, and electrical power. The higher electrical power in the Prandtl Smooth would be a concern for sUAS operations that places a premium on endurance and range. The best electrical efficiency and power consumption was with the APC 8x6 propeller. This propeller was tested to compare the custom designed propellers against a standard commercial propeller. Ultimately, there was an 8% improvement in electrical efficiency with this propeller over the Prandtl bell-shaped propeller and it also had lower torque. However, it must be understood that the APC 8x6 had a much higher RPM due to its smaller size in terms of its chord length, airfoil thickness, and weight. Despite these differences, the Prandtl propeller had the same order of magnitude in mechanical power while having a much higher increase in torque. The higher torque, mainly due to the constant chord tip treatment, would explain why more electrical power was needed for the Prandtl propeller as opposed to the APC 8x6. Therefore, the data suggests that a propeller designed with the Prandtl distribution and similar chord length, weight, and a tapered tip treatment as the 8x6, would outperform the APC 8x6 in electrical efficiency.

To obtain the SPL characterization of the test propellers, axial and radial traverses were conducted in the BRIC Low-Speed Wind Tunnel. The radial traverse was measured from an r/R of 0.375 – 1.25 with the microphone placed 1 inch aft of the propeller plane of rotation. Figure 5.32 shows the results of the 1-inch radial traverse. Table 5.6 displays the radial traverse locations where the peak SPL occurs as well as the peak value. As seen in Table 5.6 and Fig. 5.31, the Prandtl bell-shaped propeller is the lowest peak SPL and overall the lowest compared to the Baseline propeller. The Baseline propeller design had the highest SPL reading with 121.48 dBA at 0.95 r/R. The next highest SPL was 121.32

dBA with the 60_1 which occurred at 1.025 r/R. The similarity is interesting as they are both similar despite the 60_1 propeller's effort to unload the tip. This would suggest that there needs to be further study with this method of unloading the tip. Furthermore, they both have r/R SPL peak locations near the tip of the blade which would suggest that the biggest contribution to the noise would be attributed to the tip vortices. The APC 8x6 propeller produced low SPL measurements overall and only had a peak SPL at 111 dBA and 0.85 r/R. This was significantly lower than the Baseline and 60_1 propellers with a 10 dBA drop. Even more impressive is that the Prandtl and Prandtl Smooth propellers both produced less noise than the APC 8x6 propeller. Both SPL peak locations occurred at 0.775 r/R with the Prandtl SPL being slightly lower at 109.85 dBA and the Prandtl Smooth generating its peak SPL of 110.87 dBA. Despite having performance differences with the APC 8x6 that were mainly due to the Prandtl propellers' larger size and weight, the Prandtl propeller had the lowest SPL measurement of all tested propellers.

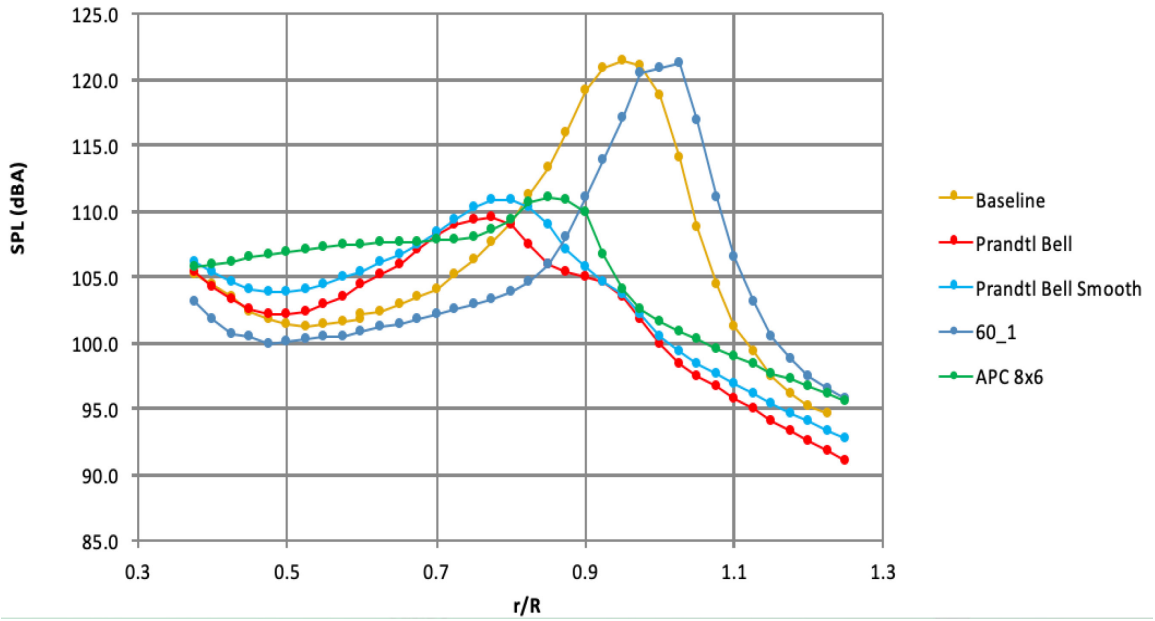

Figure 5.32 1-inch Radial Traverse Lift Distribution Propeller Comparison

Table 5.6 1-inch Radial Traverse Peak SPL r/R Locations and SPL

Propellers	r/R	SPL (dBA)
Baseline Prandtl	**0.950**	**121.49**
Prandtl Smooth	**0.775**	**109.85**
60_1	**0.775**	**110.87**
APC 8x6	**1.025**	**121.32**
	0.850	**111.00**

In addition to the radial SPL traverse, an axial traverse was conducted to further investigate the acoustic profile of the propellers. The summary of results can be seen from Table 5.7. The comparison points were described in reference to the propeller plane of rotation at 2 inches in front, on-plane (centered at the leading edge of the blade), and 3 inches aft of the propeller. The axial traverses were taken at 1 inch off the tip of the propeller blade. The objective of this traverse was to characterize the streamtube phenomena.

Table 5.7 Axial Traverse SPL Frontal, On-Plane, and Aft Comparisons

	SPL (dBA) and Microphone Location		
Propeller	Frontal (-2.0")	On-Plane (0.0")	Aft (3.0")
Baseline	**98.45**	**109.57**	**97.83**
60_1	**95.93**	**102.40**	**96.87**
Prandtl Prandtl	**99.25**	**107.12**	**91.82**
Smooth APC	**99.19**	**107.17**	**91.87**
8x6	**99.33**	**103.21**	**96.31**

The Baseline propeller SPL distribution proved to be the noisiest across all comparison points. This is reasonable given its physical profile and that it will be producing more drag

and larger vortices than the other propellers. The 60_1 propeller has the lowest noise from the frontal and on-plane aspects, but aft of the propeller plane of rotation it had the second largest SPL of 96.87 dBA. Meanwhile the APC 8x6 was the second lowest for the on-plane and aft measurements. The Prandtl and Prandtl Smooth propellers had similar values at all locations which was surprising given differences mentioned previously in their performance. The most striking observation was aft of the propeller plane of rotation the Prandtl bell-shaped and the Prandtl Smooth both had the lowest measured noise with SPLs around 91.82 dBA, and approximately a 5 dBA drop compared to the APC 8x6 propeller. Ultimately, more study is needed to determine the impact of the microphone locations and distances from the propeller noise sources to determine the best comparison point.

CHAPTER SIX

Conclusions and Future Recommendations

Summary of Completed Work

This study began with an introduction to establish the demand and wide-spread use of the UAS. Following the introduction, it was also highlighted that further development to improve aerodynamics and aeroacoustics is needed in this field. A literature survey of relevant aerodynamic research displayed the lack of an emphasis on aeroacoustics and, specifically, lift distribution research on UAS, low Reynolds number propellers. Continuing, propeller theoretical background gave more insight to the theory applied in this study. An explanation was given on the experimental setup and methods for both the USAFA and Baylor BRIC testing. Aeroacoustic experiments were performed on propellers with the TE notch and DJI Stock in an anechoic chamber. Aerodynamic and aerocoustic tests were performed on the Hoop5, Square5, Oval5, and DJI stock propellers at static conditions in a wind tunnel. Motor electrical efficiency studies were conducted on the DJI 960 Kv motor, Gartt 580 and 370 Kv motors. An airfoil study tested the AH 79-100A, FX 63120, GOE 358, and SA 7026 airfoils. Finally, a dynamic study was performed comparing the effects of a lift distribution on propellers designed for minimum induced drag.

The TE notch and Stock propeller were tested in the USAFA anechoic chamber under the investigation of the far field acoustics pertaining to a single and a hexacopter test stand. While varying azimuthal angles and microphone distance, there was no observable SPL

difference between the two propellers in the far field with increasing distance. This was evident for both the single propeller and hexacopter tests.

Three five-bladed custom designed propellers were tested against the DJI Phantom 2 Stock propeller for aerodynamic and aeroacoustic analysis. The Hoop5, Square5, and Oval5 propellers were designed with a constant chord and each had different tip treatments. It was determined that the Hoop5 propeller had the largest difference in SPL from the Stock propeller at approximately 9 dBA, achieved at 6 inches aft of the propeller plane of rotation. It was determined, through smoke fluid flow analysis, that this design had the largest effect on decreasing the magnitude of the tip vortex which contributed to its aeroacoustic performance. However, this propeller had the highest demand in mechanical power at 52.3 W while the other propellers used approximately 33.1 W.

The Hoop5 and Stock propeller were used to compare motor electrical efficiency for the DJI 960Kv, Gartt 580 Kv and Gartt 370Kv motors. A voltage dependency was determined for the DJI 960 Kv motor as it operated with an electrical efficiency of 17.4% higher while operating at lower input voltages. However, both the Gartt 580 and 370 Kv motors were not as sensitive to an input voltage dependency. Despite the sensitivity being low, the Gartt 580 and 370 Kv motors both experienced improvements of 2.4% and 3.7%, respectively, at their lower input voltage settings. Lastly, the Gartt 580 Kv performed with better electrical efficiencies than the DJI 960 Kv with a value of 31.3% higher than the Stock propeller and a value of 16.5% higher for the Hoop5 propeller.

The airfoil investigation contained 5 airfoils with the AH79-100A, FX63120, GOE358, and SA 7026 airfoils. The GOE358 was found to be the best airfoil in this comparison due to it having the greatest electrical efficiency at 67.80% which was 6.8%

higher than its closest competitor. Additionally, this airfoil had the most desirable aerodynamic characteristics with a wide L/D_{Max} operating range, larger thickness, and its high cambered profile.

Lastly, propeller lift distributions designed for minimum induced drag were applied to constant chord propellers. Dynamic testing was performed on propellers with the Baseline, Prandtl bell-shaped, Prandtl smooth, and the 60_1 lift distributions. These propellers were also compared to a commercial hobby propeller, the APC 8x6. The results showed in the Prandtl bell-shaped distribution producing the lowest peak SPL. Additionally, the Prandtl bell-shaped distribution had an 18.54% improvement in electrical efficiency over the Baseline propeller. This difference in electrical efficiency further illustrates the difference in power consumption with the largest reduction in electrical power. At 0.5 lb_f thrust the Baseline propeller used 118.66 W and the Prandtl bell-shaped propeller used 79.92 W. Ultimately, the Prandtl bell-shaped distribution displayed the overall aerodynamic and aeroacoustic performance enhancements that results from a successful minimum induced drag propeller design.

Design Recommendations for sUAS Propellers

With the completion of this study, there are many suggestions to further this work. To begin, this study focused on designing minimum induced drag propeller design. With this design a constant chord was used throughout the entire blade. Implementing various propeller tip treatments may help reduce excess drag from the tip surface area. This profile adjustment would be expected to reduce the tip vortex and thereby decrease the noise generation. Another area of focus would be to reduce the chord length to a similar sized propeller as the APC 8x6. This may reduce the overall weight of the propeller and disk

loading which would be expected to increase the RPM while potentially reducing the torque produced from the blades. Another area of improvement could possibly be seen by using different airfoils for different sections of the propeller using the minimum induced drag propeller design. Different airfoils in different sections of the blade could improve the propellers ability to efficiently produce thrust and minimize noise generation.

Experimental Improvements

While this study achieved its goals, there is room for improvements in experimental procedures and data acquisition methods. Testing involving calibration, RPM sweeps, and SPL microphone traverse measurements would all benefit from a real-time plot displaying the important data parameters. For example, a real-time plot resembling the post processed calibration curve fit would help reduce time spent processing the data. This would improve all of the experimental procedures if the post processing plots were to be included as real-time displays during testing. Additionally, it would be helpful to develop a LabVIEW virtual instrument capable of controlling the Velmex traverse stepper motors. This would expedite the time for SPL radial and axial traverse testing.

Another area of improvement would be increasing the range of the torque cell transducer. As mentioned previously, the proper on-design thrust conditions could not be met due to torque transducer limitations for the Baylor BRIC Low-Speed wind tunnel testing. Increasing the limited range of the torque cell transducer would allow for more studies to take place without limiting the propeller thrust design point. A higher range would also promote versatility for sUAS propeller studies to better simulate various on-design conditions throughout testing like hover, cruise, and maximum thrust performance.

Recommendations for Future Studies

For future studies, this work opens the door to studies focused on lift distribution applications for propeller design. A study that could further this work would be utilizing computational fluid dynamics (CFD) to determine the tip vortex strength and comparisons to lift distribution changes. This may help in the optimization process of determining the proper r/R locations for the lift distribution decrease to begin and end. Another area of focus could be the CFD optimization of the lift distribution itself. As shown in this study, the 60_1 propeller did not have a great aerodynamic and aeroacoustic performance which indicates that there is room for optimization of the way these lift distributions are applied.

Concluding Remarks

In summary, this work examined propeller designs and modifications for aerodynamic and aeroacoustic properties. These tests resulted in the development of a propeller design that was made for minimum induced drag instead of the traditional minimum induced loss through various lift distributions. With these propeller tests, future studies can use this work to expand design considerations to generate new UAS propellers.

APPENDICES

APPENDIX A

Baylor Low-Speed Wind Tunnel Propeller Testing System Diagrams

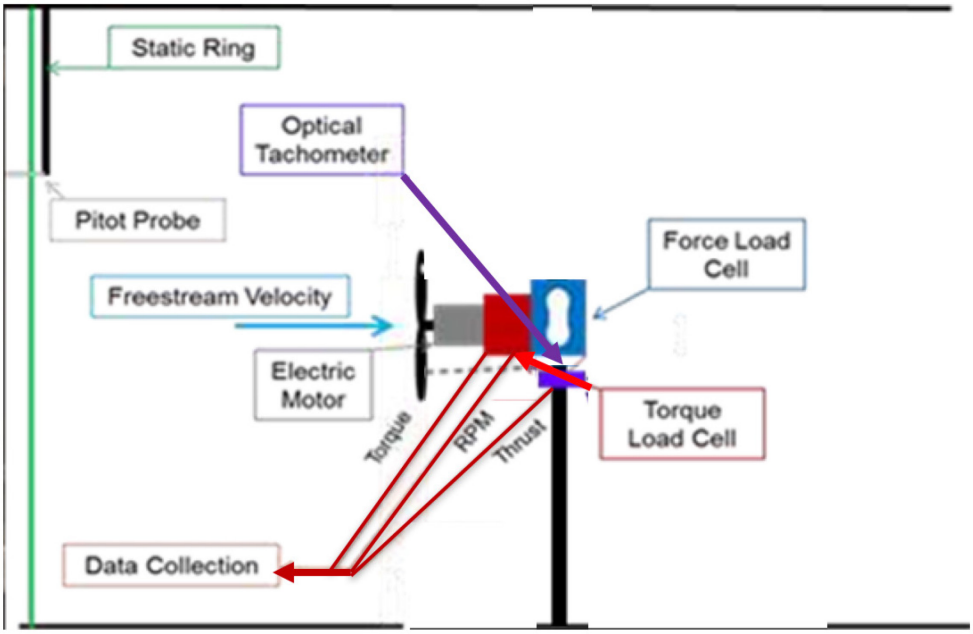

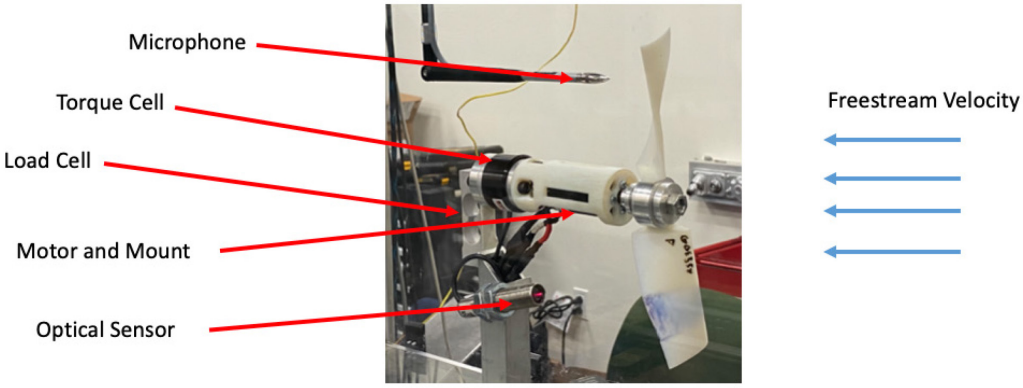

APPENDIX B

USAFA Anechoic Chamber LabVIEW VI Block Diagram

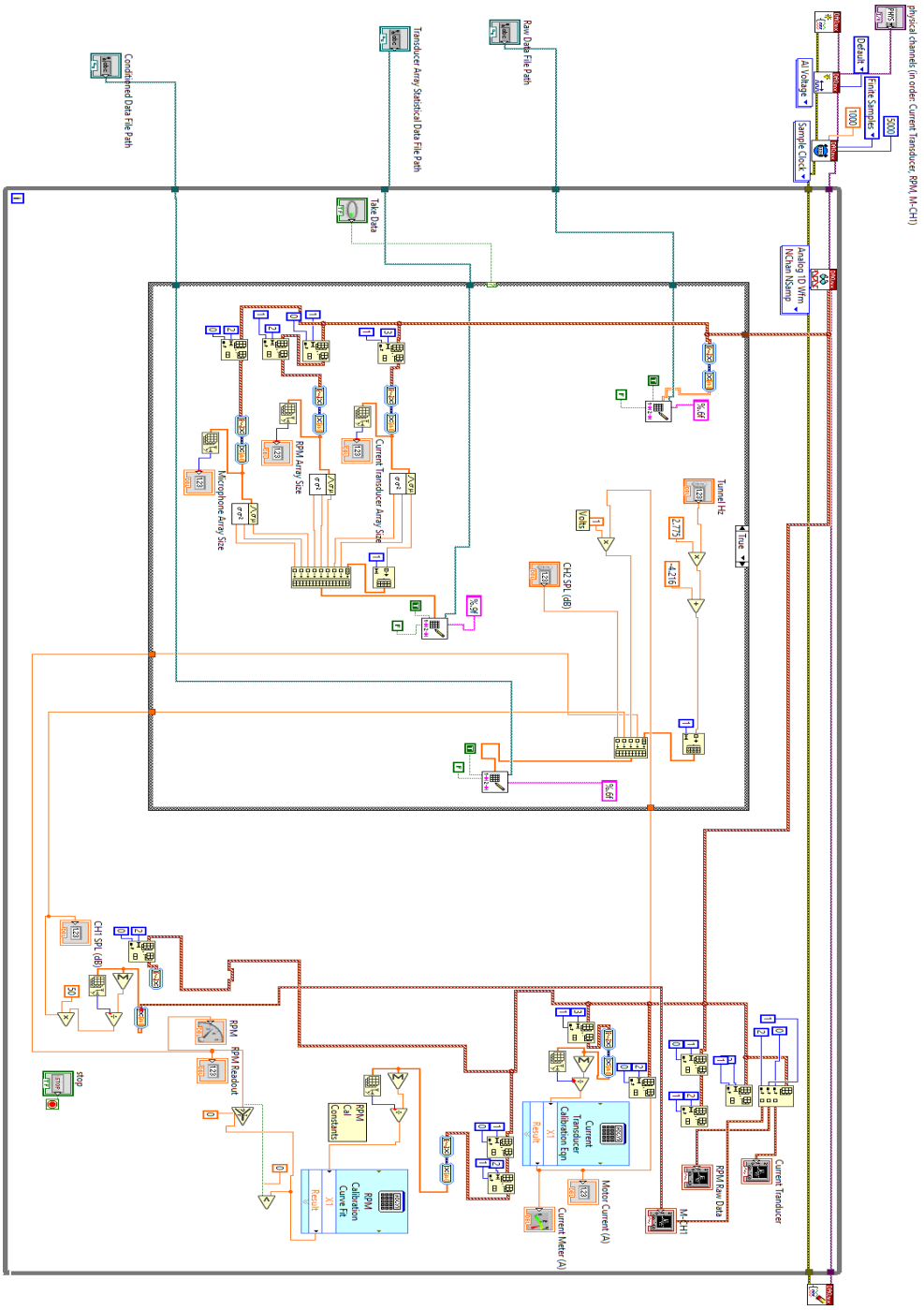

APPENDIX C

Baylor Low-Speed Wind Tunnel Propeller Testing LabVIEW VI Block Diagram

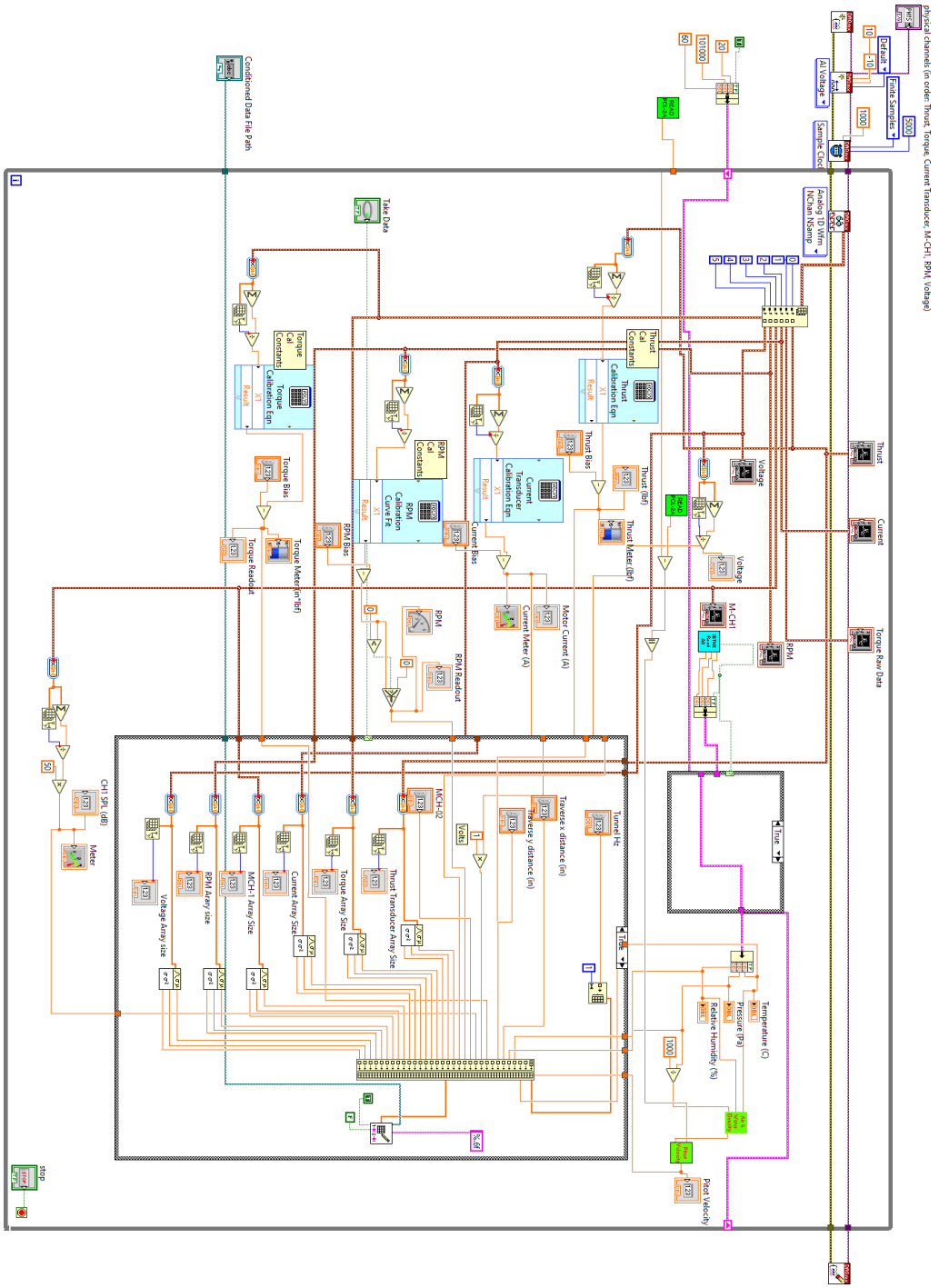

APPENDIX D

Baylor Low-Speed Wind Tunnel Calibration LabVIEW VI Block Diagram

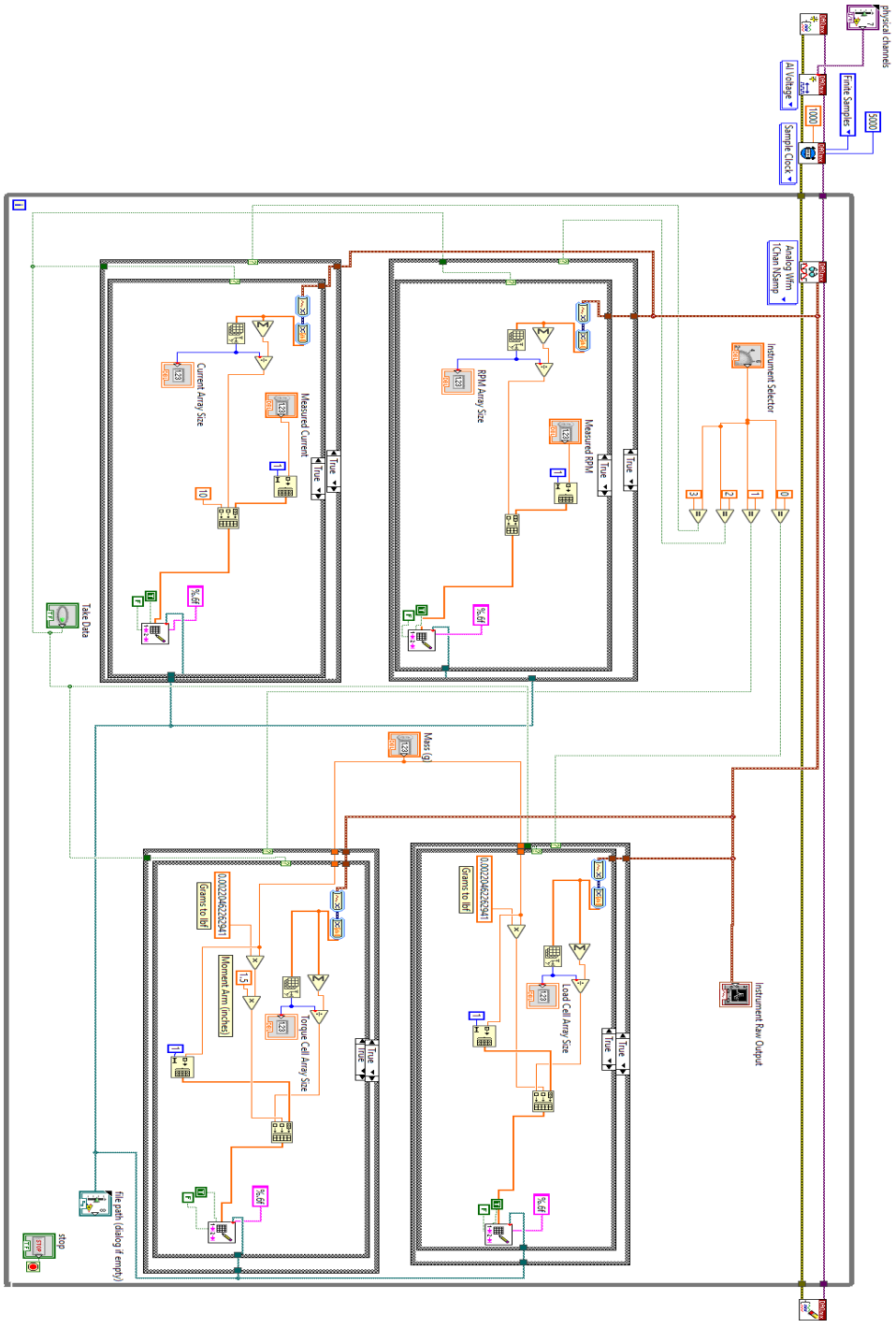

REFERENCES

[1] Esler, D., 2015, "What A Business Aviation Flight Department Needs To Know About UAS," Aviation Week and Space Technology Online. [Accessed: 18-Oct-2020].

[2] Mayor, T., and Anderson, J., 2019, "Opinion: It Is Time To Get Real On UAM," Aviation Week and Space Technology Online. https://aviationweek.com/future-aerospace/opinion-it-time-get-real-uam. [Accessed: 18-Oct-2020].

[3] Warwick, G., 2016. "The Week in Technology, Oct-6, 2017." Aviation Week and Space Technology Online, http://aviationweek.com/technology/week-technology-oct-2-6-2017. [Accessed: 18-Oct-2020].

[4] "USAF initiative Agility Prime demonstrates eVTOL advances," Airforce Technology, 24-Aug-2020. [Online]. Available: https://www.airforce-technology.com/news/usaf-initiative-agility-prime-demonstrates-evtol-advances/. [Accessed: 18-Oct-2020].

[5] V. Insinna, "US Air Force starts effort to buy a 'flying car'," Defense News, 27-Feb-2020. [Online]. Available: https://www.defensenews.com/industry/techwatch/2020/02/26/the-us-air-force-just-started-up-an-effort-to-buy-a-flying-car/. [Accessed: 18-Oct-2020].

[6] Hassanalian, M., and Abdelkefi, A., 2017, "Classifications, Applications, and Design Challenges of Drones: A Review," Progress in Aerospace Sciences, **91**, pp. 99–131.

[7] Weibel, R. E., "Safety Considerations for Operation of Different Classes of Unmanned Aerial Vehicles in the National Airspace System," p. 109.

[8] Defense Update Admin, "Black Widow Micro UAV," Defense Update: 04-Jun-2004. [Online]. Available: https://defense-update.com/20040604_black-widdow.html. [Accessed: 18-Oct-2020].

[9] "Phantom 2 - The Spirit Of Flight," DJI Official. [Online]. Available: https://www.dji.com/phantom-2. [Accessed: 18-Oct-2020].

[10] "RQ-11B Raven Small Unmanned Aircraft System (SUAS)," *USAASC*. [Online]. Available: https://asc.army.mil/web/portfolio-item/aviation_raven-suas/. [Accessed: 18-Oct-2020].

[11] Shadow TUAS. [Online]. Available: https://www.textronsystems.com/sites/default/files/_documents/ShadowV2_BlockIII_Datasheet.pdf. [Accessed: 18-Oct-2020].

[12] "RQ-4 Global Hawk," U.S. Air Force, 27-Oct-2014. [Online]. Available: https://www.af.mil/About-Us/Fact-Sheets/Display/Article/104516/rq-4-global-hawk/. [Accessed: 18-Oct-2020].

[13] "Predator C Avenger," General Atomics Aeronautical Systems Inc. [Online]. Available: https://www.ga-asi.com/remotely-piloted-aircraft/predator-c-avenger. [Accessed: 18-Oct-2020].

[14] K. Mizokami, "The F-4 Phantom Is About to Make Its Last Flight," Popular Mechanics, 14-Nov-2017. [Online]. Available: https://www.popularmechanics.com/military/aviation/a24434/f-4-phantom-retiring/. [Accessed: 19-Oct-2020].

[15] Brooks, T., Pope, D., and Marcolini, M., 1989, "Airfoil Self-Noise and Prediction," NASA Reference Publication 1218, National Aeronautics and Space Administration, Hampton, VA.

[16] Hays, A., and Van Treuren, K. W., 2019, "A Study of Power Production and Noise Generation of a Small Wind Turbine for an Urban Environment," Journal of Energy Resource Technology, 141(5), p. 051202.

[17] Van Treuren, K., and Wisniewski, C., 2019, "Testing Propeller Tip Modifications to Reduce Noise Generation on a Quadcopter Propeller," ASME Turbo Expo 2019: Turbine Technical Conference and Exposition, Phoenix, Arizona, June 17-21, 2019.

[18] Deters, R. W., Kleinke, S., and Selig, M. S., 2017, "Static Testing of Propulsion Elements for Small Multirotor Unmanned Aerial Vehicles," *35th AIAA Applied Aerodynamics Conference*, American Institute of Aeronautics and Astronautics, Denver, Colorado.

[19] NRC, 2007, *Assessment of Wingtip Modifications to Increase the Fuel Efficiency of Air Force Aircraft*, National Academies Press, Washington, D.C.

[20] Ning, A., and Kroo, I., 2010, "Multidisciplinary Considerations in the Design of Wings and Wing Tip Devices," Journal of Aircraft, 47(2), pp. 534–543.

[21] Mangler, W., 1937, "The Lift Distribution of Wings with End Plates." National Aeronautics and Space Administration.

[22] Bowers, A. H., Murillo, O. J., Eslinger, B., Technology, J., and Gelzer, C., 2016, "On Wings of the Minimum Induced Drag: Spanload Implications for Aircraft and Birds," NASA/TP-2016-219072.

[23] Wroblewski, G. E., and Ansell, P. J., 2017, "Prediction and Experimental Evaluation of Planar Wing Spanloads for Minimum Drag," Journal of Aircraft, 54(5), pp. 1664–1674.

[24] Pate, D. J., and German, B. J., 2013, "Lift Distributions for Minimum Induced Drag with Generalized Bending Moment Constraints," Journal of Aircraft, 50(3), pp. 936–946.

[25] Phillips, W. F., Hunsaker, D. F., and Joo, J. J., 2019, "Minimizing Induced Drag with Lift Distribution and Wingspan," Journal of Aircraft, 56(2), pp. 431–441.

[26] Carrizales, M. A., Lone, M. M., and Bragado Aldana, E., 2019, "Non-Elliptic Wing Lift Distribution Wings to Decrease Vertical Tailplane Size in Commercial Aircraft," *AIAA Scitech 2019 Forum*, American Institute of Aeronautics and Astronautics, San Diego, California.

[27] Jones T. R.: The spanwise distribution of lift for minimum induced drag of wings having a given lift and a given bending moment, Document ID: 19930082889, NACA Technical Note 2249, Dec 01, (1950)

[28] Ranjan, P., and Ansell, P. J., 2018, "Computational Analysis of Vortex Wakes Without Near-Field Rollup Characteristics," Journal of Aircraft, 55(5), pp. 2008–2021.

[29] Zolbayar, B.E., "Investigation of Noise from Electric, Low-Tip-Speed Aircraft Propellers," M.S. Thesis, Pennsylvania State University.

[30] Roskam, J., Lan, C.T., 1997, *Airplane Aerodynamics and Performance*, DARcorporation, Lawrence, Kansas, pp. 275-282, Chap 7.

[31] Anderson, J. D., 2011, "*Fundamentals of Aerodynamics,*" McGraw-Hill, New York, pp. 318-321, Chap. 4.

[32] I. A. Maia and F. I. da S. Junior, "PERFORMANCE ANALYSIS OF TYPICAL AIRFOILS THROUGH NUMERICAL SIMULATION USING FLUID-STRUCTURE INTERACTION," 23-Nov-2014.

[33] Van Treuren, K. W., and Hays, A. W., 2017, "A Study of Noise Generation on the E387, S823, NACA 0012, and NACA 4412 Airfoils for Use on Small-Scale Wind Turbines in the Urban Environment," Journal of Energy Resources Technology, **139**(5), p. 051217.

[34] Treuren, K. V., Sanchez, R., Wisniewski, C., and Leitch, P., 2020, “ACOUSTICALLY TESTING STOCK AND MODIFIED UAS PROPELLERS IN BOTH THE NEAR AND FAR FIELD,” p. 12.

[35] Ray, E. F., 2010, “Modeling Sound Propagation,” Industrial Noise Series Part IV, Universal, Stoughton, WI.

[36] Hansen, C. H., 2001, “Fundamentals of Acoustics,” Occupational Exposure to Noise: Evaluation, Prevention and Control,” World Health Organization, pp. 23-52.

[37] Turkdogru, M., Ahuja, K. K., and Churney, A., 2007, “Geometric Farfield Conditions for Reliable Acoustic Measurements of Ducted and Unducted Rotors,” Inter-Noise 2007, Istanbul, Turkey, 28-31 August 2007.

[38] “Environmental Noise.” Brüel and Kjaer Sound & Vibration Measurement A/S, 2000.

[39] “Environmental Noise Measurement.” Brüel and Kjaer Sound & Vibration Measurement A/S, Denmark.

[40] Prandtl L.: Über tragflügel kleinsten induzierten widerstandes. Zeitschrift für Flugtecknik und Motorluftschiffahrt, München, Deustchland, 1 VI (1933)

[41] Hurt, H. H., Jr., Aerodynamics for Naval Aviators, Skyhorse Publishing, Inc., New York NY, 2012.

[42] T. Liller, “The Design of Small Propellers Operating at Low Reynolds Numbers and Associated Experimental Evaluation,” thesis, Baylor University Graduate School, Waco, 2015.

[43] QPROP Propeller Characterization, “Propeller Characterization for QPROP,” QPROP, http://web.mit.edu/drela/Public/web/qprop/prop_measure.pdf (accessed May 25, 2015).

[44] Drela, M., 2005, “DC Motor/Propeller Matching,” Lecture Notes.

[45] Drela, M., 2006, “QPROP User Guide,” QPROP User and Theory Documents.

[46] Drela, M., 2006, “QMIL User Guide,” QPROP User and Theory Documents.

[47] Kline, S. J., and F. A. McClintock: "Describing Uncertainties in Single Sample Experiments", Mech. Eng., p. 3, January 1953.

[48] Van Treuren, K. W., and Wisniewski, C., 2019, “Testing Propeller Tip Modifications to Reduce Acoustic Noise Generation on a Quadcopter Propeller,” Journal for Engineering for Gas Turbines and Power, Vol 141, pp 121017-1 to121017-11.

[49] “GM15 (Smoothed) (Gm15sm-Il)” [Online]. Available: http://airfoiltools.com/airfoil/details?airfoil=gm15sm-il. [Accessed: 16-Mar-2020].

[50] GOE 358 AIRFOIL (Goe358-Il)” [Online]. Available: http://airfoiltools.com/airfoil/details?airfoil=goe358-il. [Accessed: 16-Mar-2020].

[51] “AH 79-100 A AIRFOIL (Ah79100a-Il)” [Online]. Available: http://www.airfoiltools.com/airfoil/details?airfoil=ah79100a-il. [Accessed: 16-Mar-2020].

[52] “FX 63-120 AIRFOIL (Fx63120-Il)” [Online]. Available: http://airfoiltools.com/airfoil/details?airfoil=fx63120-il. [Accessed: 16-Mar-2020].

[53] “SA7026 (Sa7026-Il)” [Online]. Available: http://airfoiltools.com/airfoil/details?airfoil=sa7026-il. [Accessed: 16-Mar-2020].